

Methods for Molecular Magnetic Resonance Imaging and Magnetic Resonance Spectroscopy using Hyperpolarized Nuclei

THÈSE N° 5966 (2013)

PRÉSENTÉE LE 15 NOVEMBRE 2013
À LA FACULTÉ DES SCIENCES DE BASE
GROUPE COMMENT
PROGRAMME DOCTORAL EN PHYSIQUE

ÉCOLE POLYTECHNIQUE FÉDÉRALE DE LAUSANNE

POUR L'OBTENTION DU GRADE DE DOCTEUR ÈS SCIENCES

PAR

Riccardo BALZAN

acceptée sur proposition du jury:

Prof. O. Schneider, président du jury
Prof. A. Comment, Prof. R. Gruetter, directeurs de thèse
Dr D. Mari, rapporteur
Dr B. van den Brandt, rapporteur
Prof. P. R. Vasos, rapporteur



ÉCOLE POLYTECHNIQUE
FÉDÉRALE DE LAUSANNE

Suisse
2013

The surest way to corrupt a youth
is to instruct him to hold in higher esteem
those who think alike
than those who think differently.

—— F. Nietzsche, *The Dawn*

Acknowledgments

Everything comes to an end, so it is my PhD at CIBM. A journey with good and bad moments that helped me to grow personally and scientifically. A journey I took along with many people that helped me to always go further and learn new things. All these people, I think, really deserve to be thanked.

First of all I thank Prof. Arnaud Comment and Prof. Rolf Gruetter for giving me the chance of traveling in the amazing world of DNP and guiding me when I got lost.

Thanks Simone Franchini, for always pulling me back to the theoretical side of physics, and for sharing laughs and funny moments that replenished my stamina when it was really low.

Thanks to Valerio Paladino, to keep reminding me that in the end also the experimental physics is fine if you keep enjoying it, possibly with a craft beer.

Thanks Alessandro Sellerio, that shared with me countless coffees, talking about work and not only work during almost all the PhD. You really helped me to keep my mental sanity, if I ever had it.

Thanks Tian Cheng, my first hardware teacher that opened me the doors of polarizers wonders. I hope I learned at least one tenth of what you taught me, noticing it or not.

Thanks Andrea Capozzi for the support during the long experimental days, when everything breaks and nobody knows why, and when stuff works and there is time for a beer.

Thanks Jessica Bastiaansen, for you never ending optimism.

Many thanks also to all the CIBM members, in the good and the bad I think I learned something from each one of you.

Un grazie grandissimo va alla mia famiglia, per avermi dato la spinta giusta per volare lontano ed un porto sicuro in cui tornare ogni volta che fuori non c'era altro che burrasca. In tantissimi momenti, non fosse stato per voi non so davvero come avrei fatto.

E per ultima la più importante. Nicole, non c'è niente che possa scrivere che renda giustizia a quanto hai fatto per me in questi anni, anche senza accorgertene. L'unica cosa che posso dirti è: grazie.

Lausanne, 15 November 2013

R.B.

Abstract

Since the introduction 10 years ago of the dissolution method, Dynamic Nuclear Polarization (DNP) became a widely applied and powerful technique to enhance nuclear magnetic resonance (NMR) signals of low naturally abundant, insensitive nuclear spins for analytical chemistry and biomedical research. The aim of DNP is to obtain a very high degree of polarization on the nuclei of interest in cryogenic conditions (*i.e.* 1 K), a hundred or more times higher than the thermal polarization. Then, through a fast dissolution process the molecules hosting the nuclear spins are mixed in a room temperature solution and, since their polarization is conserved if their relaxation times are long enough, they can be used for *in vitro* or *in vivo* experiments with a SNR enhanced by 10^4 times or more.

Although the DNP technique was established about 60 years ago, the hardware and cryogenic equipment needed to perform DNP and the subsequent dissolution, still are a technological challenge. In this thesis we will cover different DNP aspects, ranging from hardware installation, software development, solid state measurement, *in vitro* and *in vivo* experiments and a possible application of DNP to MRI studies of granular materials.

A new DNP cryostat was developed and tested to determine its cryogenic performances and then optimized for fast cooldown, helium holdtime and overall minimal operational consumption. We will show the characteristics of the cryostat and the performances on standard operations like cooling and DNP at 1 K. Another important aspect the development tackled was automation. The management of the system was condensed in a single electronic box capable to handle the interface with all the cryostat instruments. This box is driven by a single common USB port through a custom made software interface we developed. Although a few manual operations are still needed, we achieved a high degree of automation.

The solid state polarization enhancement ϵ is defined as the ratio between the DNP enhanced and the thermal polarization signals. It can be determined by measuring the DNP enhanced signal after the system stabilizes in the polarized state (*i.e.* after about 5 buildup time) and thermal polarization signal after the spins have fully relaxed to equilibrium (*i.e.* after about $5 T_1$). As a first application of the new system, we present a method that exploits the behavior of steady states magnetization produced with trains of evenly spaced pulses, at constant flip angle. This method allows to precisely determine the thermally polarized signal of a sample with known T_1 and a given flip angle in a small fraction (as low as half of a T_1 or less depending on the requested accuracy) of the time needed in the usual "wait $5 T_1$ and pulse" scheme.

The main drawback of the dissolution DNP is that the large polarization achieved will

ineluctably relax towards its thermal equilibrium value in a few times T_1 , that for typical ^{13}C labeled molecules is shorter than a minute. On the other hand some nuclei as ^6Li and quaternary ^{15}N show a very long T_1 on the order of few minutes in biological conditions, allowing measurements as long as several minutes.

^6Li is very sensitive to contrast agents such as *Gd*-doped contrast agents, O_2 and de-oxygenated hemoglobin. We studied the effect of the oxygenation of human and rat blood on the ^6Li T_1 , showing clear changes between oxygenated and de-oxygenated samples. Thus we showed that ^6Li could be used to map blood oxygenation levels *in vitro*, and suggest possible *in vivo* applications, even in brain due to its capability to easily pass the blood brain barrier.

^{15}N labeled choline has a very long ^{15}N T_1 and can be used to probe rate of transport or metabolism in brain. Although it has a long T_1 , the spectral dispersion between the precursor, choline, and its metabolites is very small. The spectral dispersion is much larger for ^1H spins and thus being able to partially transfer repeatedly the ^{15}N to ^1H before detection would greatly increase the spectral separation between metabolites while still being able to measure the time course of the metabolic process, which is not the case with a full transfer like with INEPT.

We demonstrate that a Hartmann–Hahn polarization transfer can be used to partially transfer the hyperpolarization of ^{15}N to surrounding ^1H before detection on ^1H . This method can then be applied to *in vivo* DNP experiments.

Even with a very high signal it is very difficult to quantify metabolites that are very close in the NMR spectrum, compared to the actual *in vivo* linewidth. To improve the spectral resolution it is worth performing the experiments in high magnetic fields. We show the first *in vivo* rat muscle DNP measurement of acetate at 14.1 T, to resolve *e.g.* the glutamate peak from acetate substrate.

Finally we discuss a segmentation algorithm used to precisely reconstruct granular samples composed of up to 10^4 spheres. We used a standard Gradient Echo imaging sequence on a Siemens 7 T MRI human scanner to obtain high resolution images of a phantom composed of a cylinder filled with Cu^{2+} doped water and plastic spheres. Then the 3D images were segmented through a thresholded Hough transform method and the beads centers determined. The datasets were studied to extract structural and geometrical information.

keywords: dissolution dynamic nuclear polarization (DNP), cryogenics and hardware for DNP, nuclear magnetic resonance (NMR), solid state polarization enhancement, *in vivo* magnetic resonance spectroscopy (MRS), Magnetic Resonance Imaging (MRI), Granular Materials (GM).

Riassunto

Negli ultimi 60 anni, la Dissolution Dynamic Nuclear Polarization (DNP) è diventata una potente tecnica per amplificare il segnale di risonanza magnetica nucleare (NMR) originato da nuclei poco abbondanti o con scarsa sensitività per la chimica analitica e la ricerca biomedica.

Lo scopo della DNP è quello di ottenere un'elevata polarizzazione dei nuclei di interesse in condizioni criogeniche (*i.e.* 1 K), centinaia o più volte quella ottenibile termicamente. Quindi, attraverso un rapido processo di dissoluzione il campione può essere trasferito in una soluzione a temperatura ambiente, conservando la polarizzazione, ed usato per esperimenti *in vitro* o *in vivo*, con un incremento di SNR dell'ordine di 10^4 .

Nonostante la tecnica sia stata sviluppata da molto tempo, l'hardware e la criogenia necessari per la DNP e la dissoluzione sono ancora una sfida tecnologica. In questa tesi verranno trattati vari aspetti della DNP, dall'installazione hardware, sviluppo software, misure in stato solido, esperimenti *in vitro* ed *in vivo* fino a possibili applicazioni della DNP allo studio tramite MRI di sistemi granulari.

Un nuovo criostato per la DNP è stato sviluppato e testato per determinarne le performance criogeniche e quindi ottimizzato in termini di velocità di raffreddamento, tempo di stoccaggio dell'elio liquido e consumo globale. Verranno presentate le caratteristiche del criostato e le sue performance in operazioni standard come raffreddamento e polarizzazione a 1 K. Un altro importante aspetto trattato riguarda l'automazione. La gestione del sistema è stata condensata in un singolo controller, interfacciato con tutti gli strumenti del criostato. Il controller è a sua volta interfacciato ad un PC, tramite una comune porta USB, e controllato attraverso un'interfaccia software sviluppata ad hoc. Nonostante alcune operazioni manuali siano ancora necessarie, il grado di automazione ottenuto è molto elevato.

L'incremento di polarizzazione in stato solido ϵ è definito come il rapporto tra la polarizzazione del sistema iperpolarizzato e quella del sistema in equilibrio termico. ϵ può essere determinato dalla misura del segnale iperpolarizzato, dopo che il sistema ha avuto il tempo di stabilizzarsi nello stato stazionario (*i.e.* dopo 5 tempi caratteristici di buildup) e il segnale polarizzato termicamente dopo che gli spin si sono completamente rilassati all'equilibrio (*i.e.* dopo $5 T_1$). Come prima applicazione del nuovo sistema, presentiamo un metodo che sfrutta il comportamento degli stati stazionari di magnetizzazione ottenuti con serie di impulsi ugualmente spazati, a flip angle costante. Questo metodo consente, conoscendo T_1 e flip angle, di determinare precisamente il segnale polarizzato termicamente, in una frazione di T_1 .

Il maggior inconveniente della DNP consiste nel fatto che la grande polarizzazione prodotta rilassa verso lo stato di equilibrio termico in pochi T_1 , che per tipiche molecole marcate

^{13}C è minore di un minuto. D'altro canto alcuni nuclei come ^6Li e ^{15}N quaternari posseggono T_1 molto lunghi, dell'ordine di alcuni minuti in condizioni biologiche, consentendo un periodo di misura dell'ordine di 10 minuti o più.

^6Li è molto sensibile ad agenti di contrasto quali Gd , O_2 e deossiemoglobina. Abbiamo studiato l'effetto dell'ossigenazione di sangue e plasma, sia umani che di ratto, sul T_1 del ^6Li , mostrando chiari cambiamenti tra campione ossigenati e deossigenati. In questo modo abbiamo mostrato che con il ^6Li è possibile mappare i livelli di ossigenazione *in vitro*, e suggerito possibili applicazioni *in vivo* anche nel cervello grazie alla sua capacità di attraversare facilmente la blood brain barrier.

La colina marcata con ^{15}N esibisce un T_1 molto lungo e può essere usata per l'osservazione dei rate di trasporto o del metabolismo nel cervello. Anche se il T_1 è molto lungo, la dispersione spettrale in ^{15}N dei metaboliti originati dalla colina è molto limitato. D'altra parte la dispersione spettrale dei ^1H è molto più elevata; perciò potendo trasferire parzialmente e ripetutamente la polarizzazione dai ^{15}N ai ^1H si incrementerebbe notevolmente la separazione spettrale dei metaboliti.

Mostreremo una tecnica basata sul trasferimento di polarizzazione Hartmann–Hahn, per trasferire parzialmente l'iperpolarizzazione dei ^{15}N ai ^1H circostanti, prima dell'acquisizione su ^1H . Questo metodo può quindi essere applicato ad esperimenti DNP *in vivo*.

Anche con un segnale molto alto la quantificazione dei metaboliti molto vicini nello spettro in rapporto alla loro larghezza di linea *in vivo*, può rivelarsi molto difficile. Per migliorare la risoluzione spettrale è utile utilizzare campi più elevati per gli esperimenti. Mostreremo le prime misure DNP *in vivo* in muscoli di ratto, utilizzando acetato iperpolarizzato, per risolvere ad esempio il picco del glutammato dal substrato di acetato.

In conclusione verrà discusso un algoritmo di segmentazione utilizzato per la precisa ricostruzione di campioni granulari composti da $10^{4\sim 5}$ sfere. Si è utilizzata una sequenza di Gradient Echo Imaging su uno scanner umano Siemens per MRI a 7 T per ottenere immagini ad alta risoluzione di un phantom composto da un cilindro riempito di una soluzione acquosa di Cu^{2+} e sfere di plastica. Dopodichè le immagini 3D sono state segmentate attraverso un metodo basato sulla trasformata di Hough ed i centri delle sfere determinati. I dataset sono stati quindi analizzati per estrarre informazioni geometriche e strutturali.

Parole chiave: Dissolution Dynamic Nuclear Polarization (DNP), criogenia e hardware per DNP, Risonanza Magnetica Nucleare (NMR), incremento di polarizzazione in stato solido, *in vivo* Spettroscopia in Risonanza Magnetica (MRS), Imaging in Risonanza Magnetica (MRI), Materiali Granulari (GM).

Contents

Acknowledgments	v
Abstract (English/Italiano)	vii
Table of contents	xii
Introduction	1
Scope of the thesis	2
1 NMR and Dissolution DNP	7
1.1 Spin properties	8
1.2 Pulsed NMR	12
1.3 Dynamic Nuclear Polarization (DNP)	18
1.4 DNP mechanisms	22
1.5 Hyperpolarization methods	28
1.6 Common methods for NMR measurements	29
2 Polarizer development and test	37
2.1 Hardware	38
2.2 Cryogenic performances	43
2.3 Conclusions	47
3 Solid-state enhancement measurement	49
3.1 Introduction	50
3.2 Evenly spaced pulses	51
3.3 Results	56
3.4 Conclusions and Outlook	59
4 Hyperpolarized ^6Li as blood oxygenation probe	61
4.1 ^6Li properties and medical applications	62
4.2 Methods	62
4.3 Results	65
4.4 Conclusions and Outlook	67
	xi

Contents

5	^{15}N labeled choline cross polarization	71
5.1	^{15}N Choline	72
5.2	Efficiency of cross polarization	73
5.3	Methods and Results	74
5.4	Conclusions and Outlook	75
6	Hyperpolarized ^{13}C NMR at 14.1 T	79
6.1	Hardware	80
6.2	Results	83
6.3	<i>In vivo</i> outlook	85
7	MRI segmentation method for granular material reconstruction	87
7.1	Methodology	88
7.2	Reconstruction algorithm	89
7.3	Data analysis and results	93
7.4	Conclusions and outlook	97
8	Conclusions and Outlooks	101
	Appendix A Polarizer development	103
	Appendix B Steady State for evenly spaced pulses	113
	Appendix C Optimized Hartmann-Hahn polarization transfer for choline	119
	Appendix D Table of abbreviations	123
	Curriculum Vitae	

Introduction

Magnetic Resonance Imaging (MRI) and Magnetic Resonance Spectroscopy (MRS) are non-invasive techniques based on Nuclear Magnetic Resonance (NMR) and widely used in medicine for acquiring anatomic and metabolic information about diseased tissues. ^1H , a spin 1/2 element with the largest nuclear gyromagnetic ratio γ among naturally abundant elements, is the nucleus of choice for *in vivo* NMR. This choice is mainly due to two reasons: the first is the large γ , producing high signal intensities and the second is its high natural isotopic (99.99%) and biological (63% for human) abundance. However, ^1H spectra are often limited by the strong water signal that can cover them of metabolites in exam, and the relatively small spectral dispersion of metabolites due to the narrow resonance frequency range. ^{13}C , ^{15}N and ^{31}P , are biologically relevant spin 1/2 nuclei involved in a wide range of metabolic processes. Their γ is substantially lower than that of ^1H and their natural isotopic and biological abundance is very low. These characteristics causes a relatively low NMR sensitivity on one hand, but little MRS and MRI background signals on the other hand. How to efficiently improve the MR sensitivity of these nuclei recently became a very important field of research, in particular in the context of metabolic studies.

The Dynamic Nuclear Polarization (DNP) method, based on the saturation of the Electron Spin Resonance (ESR) transition of free radicals to transfer the unpaired electron spin polarization to the surrounding nuclear spins in solid samples, was theoretically and experimentally studied since the 1970s to produce polarized targets for nuclear and particle physics research. Large polarizations were observed not only for proton but also for deuteron, lithium and other nuclei. Recently, a novel technique consisting in the dissolution of DNP enhanced solid samples from pumped liquid helium temperature (*i.e.* about 1 K), to obtain a nuclear spin polarization up to four orders of magnitude larger than the room-temperature thermal polarization in liquids, was applied to MRS and MRI. It became a prominent technique not only for chemical analysis but also for visualizing *in vivo* the bio-distribution of hyperpolarized substrates and their downstream metabolites. The intrinsic limitation of the technique is the finite life time of the hyperpolarized state of the molecule, which is determined by the longitudinal relaxation time T_1 of the nuclei of interest. The hyperpolarized state cannot be recovered once the magnetization is destroyed for the measurement and therefore, although it is very intense, the signal is only available for a limited amount of time.

The strategy to improve dissolution DNP consists in finding biologically relevant substrates containing long T_1 nuclear spins, maximizing their polarization and speed up the *in vivo* injection process, minimizing the losses during the transfer.

Furthermore, the use of MRS scanner at high magnetic field for *in vivo* applications, exploits the increased spectral resolution, with respect to lower field, to resolve peaks spectrally very close to each other or to the substrate resonance.

In the EPFL laboratories, DNP prepolarizers^{1;2} have been coupled to a high field MRI scanner³ and used to efficiently polarize samples at fields of 3.35 T, 5 T⁴ and above. These designs however often necessitate experienced operators and manual interaction to control the cryogenic part, as well as the dissolution. Due to the availability of a commercial setup (Oxford instrumentsTM, HypersenseTM) not many efforts were made on easing the use of these research polarizer designs. Furthermore, none of these setups has been used to perform *in vitro* or *in vivo* experiments at MRI scanner fields above 9.4T.

Scope of the thesis

The first aim of this work was the development, optimization, automation and installation of a new dissolution DNP prepolarizer (in the CIBM-EPFL laboratories and in other collaborating laboratories located abroad in universities in Europe and the United States of America) and to couple it to a Varian 14.1 T rodent MRI/MRS scanner. Afterward, several applications of the dissolution DNP technique were developed and applied to perform solid-state and *in vitro* and *in vivo* studies.

Chapter 1 provides a general introduction to NMR starting from nuclear spin characteristics, dynamics and basics of NMR experiments. Then it continues with an introduction about various DNP mechanisms and methodologies. Finally, a brief discussion on different methods for common NMR measurement related to dissolution DNP is presented.

In Chapter 2 all development steps and tests made prior to utilization of the prepolarizer are described. In the beginning, a comprehensive description of the cryogenic and dissolution hardware and their properties is given, followed by a brief description of the basic cryogenic procedures that are routinely performed during the use of the cryostat. The results of the cryogenics tests are then presented with a detailed discussion on how the operational parameters were optimized. The results show that the new design has the capability to be cooled faster from room temperature, and at the beginning of each activity period, to liquid helium temperature with respect to the previous design⁵.

In the related Appendix A, an overview of the electronic hardware interface and the software GUI used for managing the different procedures is given. Finally the cryogenic and dissolution procedures, both on hardware and software side, are discussed in detail.

The aim of Chapter 3 is to present an innovative measurement scheme that will allow to rapidly and reliably measure the DNP enhancement in the prepolarizer in a very short amount

of time compared to usual schemes. Initially a brief overview of a typical solid-state DNP experiment to determine the polarization enhancement in case of high thermal signal SNR is presented. Then we calculate the magnetization evolution towards steady state created by constant flip angle pulses evenly spaced in time and show how to rapidly perform coil calibration and measure the relaxation time T_1 . Then we introduce our method: it is based on the knowledge of the longitudinal relaxation time T_1 and the exact flip angle θ used for the measurement to rapidly create and measure magnetization steady states that can then be linked to the real thermally polarized signal.

The advantages of this method are the dramatic reduction of the measurement time (down to a fraction of T_1 , which compares advantageously to the typical $5 T_1$ before the system relaxes to thermal equilibrium), the possibility to tune the measurement time depending on the required precision and the possibility to use identical low flip angles for both hyperpolarized and thermal signals measurement. Finally, applications of this method to carboxyl ^{13}C in common biomolecules and to ^{129}Xe exhibiting long relaxation times are shown.

In the related Appendix B, we give detailed calculations of magnetization steady states and the optimal strategy to obtain a steady state starting from a saturated system. Finally, we discuss the dependence of the overall measurement time on the chosen flip angle.

In Chapter 4 an *in vitro* dissolution DNP application for molecular imaging is presented. It has been recently shown that ^6Li can be hyperpolarized in aqueous solution of $^6\text{LiCl}$ and that, thanks to its long T_1 , hyperpolarized ^6Li is very sensitive to paramagnetic agents even at very low concentration⁶. This characteristic makes ^6Li a perfect candidate for probing *in vivo* oxygenation levels of blood. To assess the feasibility of this method, we measured *in vitro* the T_1 difference between oxygenated and de-oxygenated, human and rat, blood and plasma samples. Due to their biological nature, blood and plasma samples show a high variability in their relaxivity effect on ^6Li , independently of the oxygenation level. Furthermore, the quality of the dissolution itself can affect the very long ^6Li T_1 . These two aspects rise difficulties in comparing different experiments, even on the same sample. To limit this variability, we developed a coil and NMR tubes support that allowed to simultaneously measure the relaxation time of an oxygenated and a de-oxygenated sample together with a reference D_2O sample, using the same hyperpolarized solution. We observed that although the variability between two successive measurement is quite high, the difference between the same sample, oxygenated and de-oxygenated, measured in exactly the same conditions, are quite reproducible. These results demonstrate the potentialities of $^6\text{LiCl}$ as an *in vivo* oxygenation probe to study *e.g.* tumors in rat brain with dissolution DNP on a timescale much longer than usual ^{13}C labeled molecules.

In Chapter 5 we show the preparatory work for another *in vivo* dissolution DNP application on ^{15}N labeled choline. The very long T_1 of the quaternary ^{15}N in this molecule makes it ideal for dissolution DNP applications, especially in its deuterated form. Despite that, the spectral resolution of ^{15}N choline metabolites is very low, preventing from a good metabolic characterization of choline products for *in vitro* and *in vivo* metabolic applications. To overcome this limitation, a method for partial polarization transfer using Hartmann-Hahn

polarization transfer is presented.

In this method the ^{15}N is used as a polarization reservoir, while the detection is performed on ^1H , after the partial polarization transfer, granting a much higher spectral resolution. In the related Appendix C we propose a method to use the Hartmann-hahn partial polarization transfer to obtain a constant substrate signal in all the sequential time course acquisition.

In Chapter 6, the first *in vitro* dissolution DNP experiment on a phantom in a Varian 14.1 T horizontal bore MRI/MRS scanner using ^{13}C -acetate substrate will be presented. We will first present the dissolution setup and the details of the hardware coupling to the 14.1 T scanner. Then the calibrations to optimize the dissolution procedure will be shown. Then the first *in vitro* results of polarization enhancement, measured inside the infusion pump before the injection, will be shown.

Chapter 7 is dedicated to an uncommon use of MRI to study Granular Materials. Granular Materials are complex systems composed of a large number of particles interacting mainly via contact forces. Experimentally, granular systems show a rich and complex behavior⁷⁻⁹. Studying their structure is a key feature to understand their properties. First, we present the samples we studied: a granular system composed of *mm* sized plastic spheres soaked in a cylinder filled with a Cu^{2+} doped water solution. Then we show the MRI acquisition details to obtain high resolution images through a standard Gradient Echo imaging sequence in a Siemens 7 T MRI human scanner with a volume coil designed to accommodate a human head. Afterward we present our method, based on a thresholded real space Hough transform on the full 3D images, to determine with very high precision the beads centers. The results are then discussed with the used data analysis methods. Finally a proposal on how DNP could be applied to this technique is discussed.

References

- [1] J. H. Ardenkjaer-Larsen, B. Fridlund, A. Gram, G. Hansson, L. Hansson, M. H. Lerche, R. Servin, M. Thaning, and K. Golman. Increase in signal-to-noise ratio of > 10,000 times in liquid-state NMR. *Proceedings of the National Academy of Sciences of the United States of America*, 100(18):10158–10163, 2003.
- [2] J. H. Ardenkjaer-Larsen, A. M. Leach, N. Clarke, J. Urbahn, D. Anderson, and T. W. Skloss. Dynamic nuclear polarization polarizer for sterile use intent. *Nmr in Biomedicine*, 24(8):927–932, 2011.
- [3] A. Comment, B. van den Brandt, K. Uffmann, F. Kurdzesau, S. Jannin, J. A. Konter, P. Hautle, W. T. Wenckebach, R. Gruetter, and J. J. van der Klink. Principles of operation of a DNP prepolarizer coupled to a rodent MRI scanner. *Applied Magnetic Resonance*, 34(3-4):313–319, 2008.
- [4] S. Jannin, A. Comment, F. Kurdzesau, J. A. Konter, P. Hautle, B. van den Brandt, and J. J. van der Klink. A 140 GHz prepolarizer for dissolution dynamic nuclear polarization. *Journal of Chemical Physics*, 128(24):241102, 2008.
- [5] A. Comment, B. van den Brandt, K. Uffmann, F. Kurdzesau, S. Jannin, J. A. Konter, P. Hautle, W. T. H. Wenckebach, R. Gruetter, and J. J. van der Klink. Design and performance of a DNP prepolarizer coupled to a rodent MRI scanner. *Concepts in Magnetic Resonance Part B-Magnetic Resonance Engineering*, 31B(4):255–269, 2007.
- [6] R. B. van Heeswijk, K. Uffmann, A. Comment, F. Kurdzesau, C. Perazzolo, C. Cudalbu, S. Jannin, J. A. Konter, P. Hautle, B. van den Brandt, G. Navon, J. J. van der Klink, and R. Gruetter. Hyperpolarized lithium-6 as a sensor of nanomolar contrast agents. *Magn Reson Med*, 61(6):1489–93, 2009.
- [7] R. L. Brown and J. C. Richards. *Principles of powder mechanics*, volume 10 of *International series of monographs in chemical engineering*. Pergamon Press, 1970.
- [8] R. M. Nedderman. *Statics and Kinematics of Granular Materials*. Cambridge University Press, Cambridge, November 1992.
- [9] H. M. Jaeger, S. R. Nagel, and R. P. Behringer. Granular solids, liquids, and gases. *Rev. Mod. Phys.*, 68(4):1259–1273, Oct 1996.

1 NMR and Dissolution DNP

Abstract

NMR is a technique used to probe and study the magnetic properties of molecules. It is non-invasive in the sense that it does not damage the measured sample and can be applied to solid-state, liquid-state and *in vivo*. After the introduction of the Fourier transform to the temporal responses of the nuclear spins after RF excitation pulses, the capabilities to extract information about the environment and the chemical structure of molecules from frequency spectra has increased leading to have NMR as a powerful tool especially in medicine where structural and metabolic information can be obtained *in vivo* without harm to the patient. The main drawback of conventional pulsed NMR is that the signal intensity depends on the thermal polarization of the nuclear spins, that is very small at ambient temperature and common NMR fields. Dissolution DNP is a powerful technique that allows to produce liquid state solutions with very high nuclear spin polarizations, on the order of tens of a percent. DNP can lead to dramatic enhancements of the Signal-to-Noise Ratio (SNR) of insensitive nuclear spins with low gyromagnetic ratio and natural isotopic abundance. An introduction to the basics of pulsed NMR and DNP mechanisms is given in this chapter.

1.1 Spin properties

Spin properties and states

NMR probes the magnetic properties of molecules through the intrinsic nuclear angular momentum \hat{J} of their nuclei. The momentum rises from the combination of the nuclear spin wave function of protons and neutrons, and their orbital wave function. \hat{J} can be expressed as:

$$\hat{J} = \hat{I} \cdot \hbar \quad (1.1)$$

where \hbar is the Dirac's constant, and \hat{I} is the total nuclear spin momentum. The spin quantum number I , measurable quantity of \hat{I} , is a positive integer (possibly zero) for nuclei with an even number of nucleons and a half integer (never zero) for nuclei with odd number of nucleons. This comes from the properties of the spin wave functions. The magnetic quantum number, m_I can be used to represent the spin state. m_I can range between $-I$ to I in steps of 1. All nuclei in the periodic table can be categorized into three main types according to their total spin number:

- a) Non-magnetic nuclei with $I = 0$. These nuclei cannot be probed by NMR;
- b) Pure dipolar nuclei $I = 1/2$;
- c) Nuclei exhibiting quadrupolar or higher moments with $I > 1/2$.

The categorization to separate $I = 1/2$ from other nuclei, comes from the observation that the quadrupolar moment of the latter usually leads to very short relaxation times T_1 . This makes them less interesting for dissolution DNP, for which a sufficiently long liquid state relaxation time is necessary.

Table 1.1 shows all NMR nuclei that will be discussed in this thesis.

Nucleus	Net spin	γ [MHz/T]	N.A. [%]
^1H	1/2	42.58	99.985
^2H	1	6.54	0.015
^6Li	1	6.27	7.42
^{13}C	1/2	10.71	1.11
^{15}N	1/2	-4.32	0.37
^{129}Xe	1/2	-11.84	75.1

Table 1.1: Total spin, gyromagnetic ratio γ and natural abundance of the nuclear isotopes treated in this thesis.

A nuclear spin with angular momentum \vec{J} posses a magnetic moment $\vec{\mu}$ defined as:

$$\vec{\mu} = \gamma \vec{J} = \hbar \gamma \vec{I}. \quad (1.2)$$

where γ is the characteristic gyromagnetic ratio of the spin. The gyromagnetic ratio is an intrinsic property of a particle with spin and can assume very different values (as an example, electrons have a gyromagnetic ratio 658 times larger than 1H). Gyromagnetic ratios of nuclei of interest in this thesis are shown in table 1.1.

For isolated spins, neglecting relaxation effects, a classical approach to the dynamics in magnetic fields can be used. If we consider the magnetic moment $\vec{\mu}$ of a spin, placed in an external magnetic field \vec{B}_0 and not parallel to it, $\vec{\mu}$ starts to precess around \vec{B}_0 . The precession can be described as:

$$\frac{d\vec{\mu}}{dt} = \gamma(\vec{\mu} \times \vec{B}_0) \quad (1.3)$$

The solution of equation 1.3 gives a circular trajectory for the spin magnetization perpendicular to \vec{B}_0 with frequency

$$\omega_0 = \gamma B_0 \quad (1.4)$$

where ω_0 , the precession frequency is also called Larmor frequency.

From a quantum mechanical point of view, the spin energy levels of a spin $I = 1/2$ or a spin $I > 1/2$ with a negligible quadrupolar moment are degenerate in the absence of a magnetic field. The application of \vec{B}_0 produces an energy difference between levels with different m_I , removing the degeneracy and creating $2I + 1$ energy separated levels. This energy splitting is called Zeeman effect. The possible energy levels are related to the magnetic quantum number m_I through the relation:

$$E_m = -\hbar \gamma B_0 m_I. \quad (1.5)$$

with an energy gap between neighbor energy levels of:

$$\Delta E = \hbar \gamma B_0 = \hbar \omega_0 \quad (1.6)$$

Since the only allowed first order spin transitions are them with $\Delta m_I = \pm 1$, the difference between neighbor levels in equation 1.6 gives the NMR resonance frequency, in analogy with the classical Larmor frequency, at which the nuclei can be observed.

Populations and polarization

Spins with $I = 1/2$ have only two available states with $m_I = \pm 1/2$. These states are named "up" or "down" with respect to the quantization direction of \vec{B}_0 . These levels are separated by an energy difference of $\hbar\gamma B_0$. At thermal equilibrium, although spin transitions due to fluctuations continuously take place, the average population ratio between the two spin states stays constant. As for nuclear spins $\omega_0 \ll kT$ in all the conditions examined in this thesis, we can assume that populations on both energy levels follow Boltzmann distribution such that:

$$\frac{N_{-\frac{1}{2}}}{N_{\frac{1}{2}}} = e^{-\frac{\Delta E}{kT}} \quad (1.7)$$

where N represent the population of the state in exam. T is the sample temperature and k is the Boltzmann constant. To relate the amount of population asymmetry we can define the polarization P as:

$$P = \frac{N_{\frac{1}{2}} - N_{-\frac{1}{2}}}{N_{\frac{1}{2}} + N_{-\frac{1}{2}}} = \frac{1 - \frac{N_{-\frac{1}{2}}}{N_{\frac{1}{2}}}}{1 + \frac{N_{-\frac{1}{2}}}{N_{\frac{1}{2}}}} = \tanh \frac{\hbar\gamma B_0}{2kT} \quad (1.8)$$

for $I = 1/2$ nuclei and as:

$$P = \frac{N_1 - N_{-1}}{N_1 + N_0 + N_{-1}} = \frac{2 \sinh \frac{\hbar\gamma B_0}{kT}}{1 + 2 \cosh \frac{\hbar\gamma B_0}{kT}} \quad (1.9)$$

for $I = 1$ nuclei as for example ${}^6\text{Li}$.

This quantity reflects the spin states population and is also proportional to the NMR signal.

These expressions are valid only as long as the Boltzmann distribution holds. A zero polarization means an equal population among the levels. $|P| = 1$ corresponds to a case in which all the spins are on one of the maximum or minimum energy levels. $P > 0$ describes a system with higher population on the lower energy level and conversely if $P < 0$ the upper level is more populated. At thermal equilibrium $P > 0$ always. Note that the direction of the nuclear spin

magnetization at thermal equilibrium with respect to \vec{B}_0 depends on the sign of γ : a positive γ represents nuclei with lower energy states if $\vec{B}_0 \cdot \vec{\mu} > 0$ and thus nuclei tends to align their spin parallel and in the same direction as \vec{B}_0 . In the following we discuss only the properties of polarization for $I = 1/2$ nuclei. The same results can be qualitatively applied as well to $I > 1/2$ nuclei.

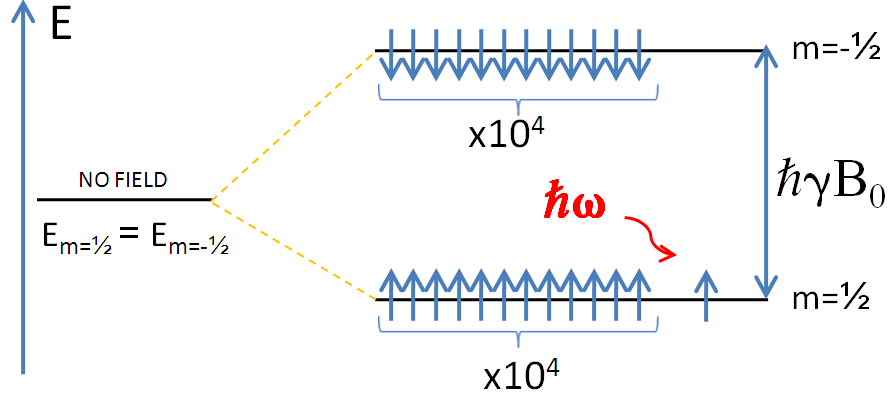


Figure 1.1: Scaled Boltzmann spin population distribution at thermal equilibrium for ^{13}C and transition induced by a quantum of energy $\hbar\omega = \hbar\gamma B_0$.

In Figure 1.1 the degeneracy produced by a field B_0 is depicted with a scale representation of average energy level population for ^{13}C at room temperature and 9.4 T . The quantum of energy $\hbar\omega$ excites the spins inducing transitions. Only the small difference in population between levels can be used to produce a non-zero variation of magnetization perpendicular to \vec{B}_0 and generating NMR signal.

In the frame of the high-temperature approximation ($\frac{\hbar\gamma B_0}{2kT} \ll 1$), the polarization can be simplified as:

$$P = \tanh \frac{\hbar\gamma B_0}{2kT} \approx \frac{\hbar\gamma B_0}{2kT} \quad (1.10)$$

The thermal equilibrium polarization depends fundamentally on three factors:

- the gyromagnetic ratio γ of the particle;
- the external field \vec{B}_0 ;
- the sample temperature T .

Table 1.2 shows the very low thermal polarization achieved by nuclei in normal MRI/MRS scanner conditions. The last columns shows that decreasing temperature to 1 K (common dissolution DNP condition during the solid-state DNP procedure), the polarization of nuclei increases dramatically and in case of electrons almost reaches unity.

Particle	$\gamma [\frac{MHz}{T}]$	RT 9.4 T [ppm P]	1 K 5 T [% P]
e^-	-28'024	21'067 [2.1 %]	99.76
1H	42.58	32.01	0.5109
2H	6.54	4.92	0.0785
6Li	6.27	6.28	0.1003
^{13}C	10.71	8.05	0.1285
^{15}N	-4.32	3.25	0.0518
^{129}Xe	-11.84	8.90	0.1421

Table 1.2: List of thermal polarization of electrons and different nuclear species in common MRI conditions and in common DNP conditions.

1.2 Pulsed NMR

In Section 1.1 we discussed the behavior of nuclear spins and their magnetization in an external magnetic field at thermal equilibrium before defining the concept of polarization. What NMR is sensitive to, is the total magnetization \vec{M} given by the sum of all the nuclear spin $\vec{\mu}$. Due to the low polarization in normal NMR conditions, even if the total number of nuclei in a sample is huge, the net magnetization is very small. This is the reason why, compared to other spectroscopic methods, NMR is considered an insensitive technique.

Unlike current or voltage which are usually measured directly, in our case magnetization is measured indirectly according to Maxwell equations:

$$\begin{aligned}\nabla \times \vec{E} &= -\frac{\partial \vec{B}}{\partial t} \\ \nabla \times \vec{H} &= \vec{J}_0 - \frac{\partial \vec{D}}{\partial t}\end{aligned}\tag{1.11}$$

The variations of magnetic field \vec{B} across a surface, generates an electric field \vec{E} used to induce a current in a closed loop, for example the RF coil in NMR measurements. On the other hand a variable electric displacement field \vec{D} in the RF coil, generates magnetic field \vec{H} around it.

The basic idea of NMR is to perturb the thermal equilibrium state of a spin system and measure the alternative magnetic field signals generated in the sample. The maximal NMR signal is detected when the detecting surface of the coil of the resonant circuit, is perpendicular to the derivative of the magnetic flux originated by the spins precession, meaning parallel to the B_0 field.

The simplest NMR experiment can be schematically described as follows:

- an alternative current pulse, with frequency close to the resonance frequency of the nucleus ω_{RF} , is sent in the coil for a defined time; this current induces an alternative magnetic field \vec{B}_1 in a volume defined by the coil geometry. \vec{B}_1 induces a rotation around

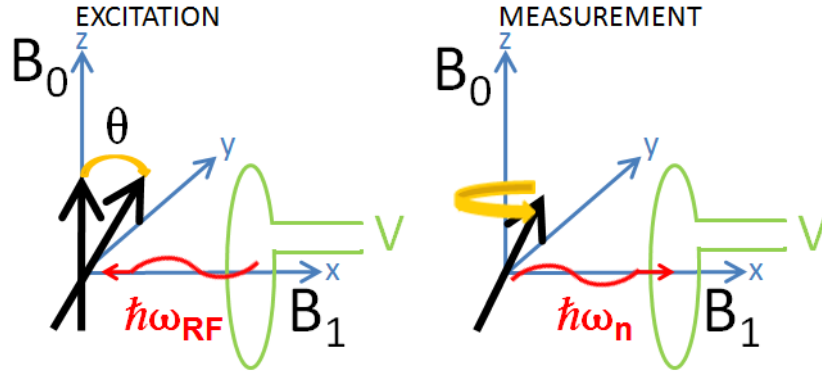


Figure 1.2: Classical schematics of the magnetization excitation (left) and NMR signal detection of the voltage induced in the coil by the precessing magnetization tilted by a flip angle θ about B_0 (right). Conventionally B_0 lies on the z axis, the coil is perpendicular to the x axis, producing an alternative field B_1 parallel to x , and magnetization vector is rotated on the yz plane.

the coil axis of the nuclear magnetization of the spins with resonance frequency close to ω_{RF} ; the rotation or "flip" angle achieved depends on the pulse length and power; for the present example we assume that at the end of the pulse the magnetization lies in the plane perpendicular to \vec{B}_0 ;

- the nuclear magnetization, precessing about \vec{B}_0 , induces a current in the coil; this current is the sum of the currents generated by the precession of all the excited spins at their own specific ω_0 . Analyzing the measured current gives information about the environment of the nuclear spins.

Figure 1.2 schematically represents the classical picture for system excitation (left) and the following measurement of the voltage induced in the coil (green) by the spin precession about the B_0 field. For convenience we define the Z axis parallel to the magnetic field \vec{B}_0 and we place the RF coil loop with axis parallel to the X axis.

The intensity of the measured NMR signal, other than on the total sample magnetization, depends also on the resonant circuit characteristics and on the RF coil sensitivity.

Rotating frame

The spins precession frequency around \vec{B}_0 is given by the Larmor frequency ω_0 . Knowing that frequency, it is useful to introduce a new reference frame called the rotating frame. This new frame is rotating about the Z axis of the laboratory frame at constant speed. The rotating frequency of the new frame is set to the excitation pulse frequency, ω_{RF} , close to the nuclei resonance frequency ω_0 . In this frame the intensity of the effective \vec{B}_0 is greatly reduced, eventually vanishing if the offset frequency $\Omega = \omega_{RF} - \omega_0$ is exactly zero. Combined with the \vec{B}_1 field created by the RF coil, the effective magnetic field \vec{B}_{eff} acting on the spins in the

rotating frame is given by:

$$B_{eff} = \sqrt{B_1^2 + \left(\frac{\Omega}{\gamma}\right)^2} \quad (1.12)$$

In the rotating frame B_1 and B_{eff} are both static. If $\Omega = 0$, $B_{eff} = B_1$ and it is perpendicular to \vec{B}_0 . This case is called on-resonance and produces, in the rotating frame, a rotation of the magnetization vector about the B_1 field with frequency $\omega_1 = \gamma B_1$.

Effect of RF pulses

To quantitatively obtain a perturbation on a spin ensemble, RF pulses are used in NMR. An on-resonance RF pulse described as $\vec{B}_1(t) = \vec{B}_1 \cdot \sin \omega_0 t$ applied in a resonant coil surrounding the sample in exam, creates an alternative $\vec{B}_1(t)$ field that rotates the magnetization by an angle θ . θ is called rotating angle or flip angle. For a square shaped pulse, θ is given by:

$$\theta = -\gamma \cdot |\vec{B}_1| \cdot \tau_P \quad (1.13)$$

where τ_P is the RF pulse length. \vec{B}_1 , the field intensity, accounts for the pulse power and the coil characteristics. Increasing the pulse length τ_P , the flip angle increases linearly. The intensity of the detectable NMR signal corresponds to the magnetization component projected on the XY plane, given by (see figure 1.2):

$$M_{XY} = M_0 \sin \theta \quad (1.14)$$

The NMR signal intensity is thus maximized when $\theta = (n + \frac{1}{2})\pi$ and zero when $\theta = n\pi$ with n integer. The exact knowledge of the flip angle used, especially in complex pulse sequences, makes very important a careful calibration before each experiment.

NMR signal and Fourier transform

RF coils detect the derivative of spin magnetization dynamics in the xy plane. After an RF pulse, the detected NMR signal in the transverse plane oscillates with a frequency of ω_0 and decreases exponentially to zero after a characteristic time T_2^* . This decay is due to transverse relaxation processes and magnetic field inhomogeneities. This oscillation decay measurement is called Free Induction Decay (FID).

This FID $f(t)$ is not a perfectly single decay but in fact it is the superposition of the

oscillations of many different nuclei, eventually having slightly different oscillation frequencies due to the different magnetic environment they are embedded in. These frequency differences are caused by different reasons, namely the different chemical shifts, the magnetic spin-spin interaction (scalar and dipolar couplings), and others.

Fourier transforming $F(\omega)$ the FID $f(t)$ it is possible to separate, in the frequency domain, the signals arising from nuclei with different ω_0 :

$$F(\omega) = \int_{-\infty}^{\infty} f(t) \exp(-i\omega t) dt \quad (1.15)$$

with

$$\begin{aligned} \operatorname{Re}[F(\omega)] &= \int_{-\infty}^{\infty} \operatorname{Re}[f(t)] \cos(-i\omega t) + \operatorname{Im}[f(t)] \sin(-i\omega t) dt \\ \operatorname{Im}[F(\omega)] &= \int_{-\infty}^{\infty} \operatorname{Im}[f(t)] \cos(-i\omega t) + \operatorname{Re}[f(t)] \sin(-i\omega t) dt \end{aligned} \quad (1.16)$$

The NMR hardware allows to simultaneously measure both real and imaginary parts of the FID, using a quadrature phase detector. The line-width of each single Fourier-transformed signal is related to both the field inhomogeneity and to the intrinsic transverse relaxation processes.

It is important to note that:

- the pulse used can excite only nuclei resonating at frequency close to ω_{RF} ; a rough estimation of the nuclei that can be excited is given by $\omega_{RF} - \Delta_P < \omega_{nuc} < \omega_{RF} + \Delta_P$ where $\Delta_P = \frac{1}{2\tau_P}$ and τ_P is the pulse length;
- the acquired signal covers only a window of frequencies centered at ω_{RF} , $\Delta_A = \frac{1}{2\delta_A}$ wide where δ_A is the time resolution of the acquisition.

Chemical shift

The chemical shift depends on the chemical and electronic structure of the molecules in which the examined nuclear spins are embedded. It is defined as the frequency difference between the NMR signal of a given reference, resonating at ω_0 , and the actual frequency of the nuclei in exam, resonating at ω . Giving it in relative units makes this quantity independent of B_0 . The chemical shift is defined as:

$$\delta = \frac{\omega - \omega_0}{\omega_0} \cdot 10^6 ppm \quad (1.17)$$

Tetramethylsilane (TMS) is used as ω_0 reference for both 1H and ^{13}C .

The frequency separation of signals arising from nuclei at different chemical shift, increases linearly with the magnetic field.

Chemical shift is caused by local magnetic field distortions produced by the electrons in orbitals close to the nuclear spins. Chemical shift are the basic tool of NMR spectroscopy to analyze samples chemical composition.

Spin dynamics and relaxation

After the RF pulse has been applied to excite the spin ensemble, the system tends to relax to its thermal equilibrium state defined by Boltzmann equations in equations 1.8 and 1.9. The spin magnetization evolution can be described with a semi-classical approach in the rotating frame using Bloch equations¹ as follows:

$$\frac{d}{dt}\vec{M}(t) = \gamma \cdot \vec{M}(t) \times \vec{B}(t) + R \cdot (\vec{M}(t) - \vec{M}_0) \quad (1.18)$$

where $\vec{B}(t) = (\vec{B}_1 \cos(\omega_0 t), \vec{B}_1 \sin(\omega_0 t), \vec{B}_0)$ is the magnetic field vector and the relaxation matrix is defined as:

$$R = \begin{bmatrix} 1/T_2 & 0 & 0 \\ 0 & 1/T_2 & 0 \\ 0 & 0 & 1/T_1 \end{bmatrix} \quad (1.19)$$

where T_1 and T_2 are the longitudinal and transverse relaxation time, respectively.

Solving the differential Bloch equations, in absence of \vec{B}_1 , we obtain:

$$\begin{aligned} M_Z(t) &= M_0(1 - e^{-t/T_1}) + M_Z(t_0)e^{-t/T_1} \\ M_{X,Y}(t) &= M_{X,Y}(t_0)e^{-t/T_2} \end{aligned} \quad (1.20)$$

where $M_{X,Y}$ and M_Z are the transverse and longitudinal magnetization, respectively.

Analyzing equations 1.20, we can state that T_1 corresponds to the characteristic time needed by the spins to relax to their thermal equilibrium. Similarly T_2 is the characteristic time relative to the magnetization dephasing in the XY plane. As $M_{XY}(t)$ and $M_Z(t)$ can be indirectly measured by NMR, the measurements are used to determine T_1 and T_2 through the Bloch equations. In this work we mainly focused on T_1 and total thermal equilibrium magnetization measurements. Various methods used for samples measurements are presented in section 1.6.

Relaxation mechanisms

The BPP (Bloembergen-Purcell-Pound) theory² first explained the NMR relaxation mechanisms. It studies how motion of spins is influenced by the environment stochastic fluctuations. The longitudinal relaxation, also called spin-lattice relaxation, originates from the random roto-vibrations of the lattice, causing random oscillating magnetic fields at the nuclear spin sites. The resulting longitudinal, or T_1 , relaxation is a reorientation of the nuclear spin parallel to the static magnetic field \vec{B}_0 with populations governed by the Boltzmann distribution. The transverse relaxation causes the loss of coherence in the transverse plane. It is caused by the spin-spin interactions that randomly change the phase of each single spin, decreasing the net magnetization precessing around B_0 . The initial coherent motion of the spins is progressively lost and finally the net magnetization M_{XY} in the XY plane vanishes. The transverse relaxation time T_2 is always longer than the measured FID relaxation time T_2^* , the latter being also affected by field inhomogeneities. In usual conditions $T_2 < T_1$.

The starting point of the mechanics of relaxation lies on the definition of a fluctuation spectral density function $J(\omega)$ that accounts for the intensity of random noise fluctuation at a certain frequency ω . $J(\omega)$ is defined as:

$$J(\omega) = \frac{\tau_c}{1 + \omega^2 \tau_c^2} \quad (1.21)$$

where τ_c is the random motions characteristic correlation time. For a homonuclear spin $I = \frac{1}{2}$ system the longitudinal and transverse relaxation rates are:

$$\begin{aligned} R_1 \quad \frac{1}{T_1} &= K [J(\omega_0) + 4J(2\omega_0)] \\ R_2 \quad \frac{1}{T_2} &= \frac{K}{2} [3J(0) + 5J(\omega_0) + 2J(2\omega_0)] \end{aligned} \quad (1.22)$$

where K represents a constant related to the spin species and the average distance r between two spins. K is given by:

$$K = \left(\frac{\mu_0}{4\pi} \right)^2 \cdot \frac{3\hbar^2 \gamma^4}{10r^6}. \quad (1.23)$$

Equations 1.22 can describe several situations:

- a) if the correlation time is extremely short $\omega_0^2 \tau_c^2 \ll 1$, then $T_2 \approx T_1$;
- b) if the correlation time is long enough to have $\omega_0^2 \tau_c^2 \gg 1$, then $T_2 \ll T_1$;
- c) in between these cases we have a range of τ_c in which T_1 reaches a minimum, but T_2

monotonically decreases with increasing τ_c . This is because of the $J(0)$ term absent in the T_1 expression.

The more important interactions leading to relaxation processes are related to paramagnetic species, dipolar interaction, and chemical shift anisotropy. These mechanisms are described in detail in literature²⁻⁴.

1.3 Dynamic Nuclear Polarization (DNP)

The NMR signal intensity is directly proportional to the total net equilibrium magnetization that depends on the polarization. Polarization varies with magnetic field and temperature as seen in equation 1.10. Room temperature polarization, even at high magnetic field, is of the order of $10^{-4\sim 5}$ for all nuclear species, as shown in table 1.2. This low polarization level gives that a large number of spins is required to have a decent NMR signal. Important improvements were achieved, in order to increase the NMR signal, on one side increasing the magnetic field of the superconducting magnets, thus enhancing the thermal polarization, and on the other side improving the sensitivity of RF coils.

Another approach is to increase the polarization of the nuclei before the NMR measurements by creating an out of equilibrium nuclear spin polarization, far beyond the thermal equilibrium polarization. One of these hyperpolarization methods is DNP.

DNP aims at transferring as much as possible of the high polarization achieved by unpaired electrons or particular electrons pair states, to nuclei enhancing the nuclear polarization.

In our case of interest, continuous microwave irradiation is applied to saturate the ESR line of the unpaired electrons of stable radicals or paramagnetic centers added to a sample containing the nuclear spins to be hyperpolarized. The high polarization of unpaired electrons in stable radicals or of the paramagnetic centers, can be transferred through dipolar-dipolar hyperfine interactions to the nuclear spin system. This way, with the same sample concentration, the NMR signal obtained by a measurement is significantly enhanced.

In this section we will introduce several fundamental spin transition processes playing a role in DNP. Then the concept of spin temperature is introduced and the three main DNP mechanisms discussed: the Overhauser Effect, the Solid Effect and the Thermal Mixing. To conclude, some other hyperpolarization methods will be presented.

General DNP mechanism

The general mechanism of DNP, depicted in figure 1.3, is used to transfer the unpaired electron spin polarization to nuclei. The electron spin transition is saturated by microwave irradiation. The frequency ω used for the saturation is close to the electron Larmor frequency ω_e . The out-of-resonance irradiation allows the interaction of electrons with nuclei, through electron-nuclear spin flip-flop transitions, in order to compensate the energy offset. This

interaction causes the polarization transfer from the highly polarized electrons to the poorly polarized nuclei. The typical energy exchange through electron-nuclear interactions normally involves one nuclear spin and one or more electron spins.

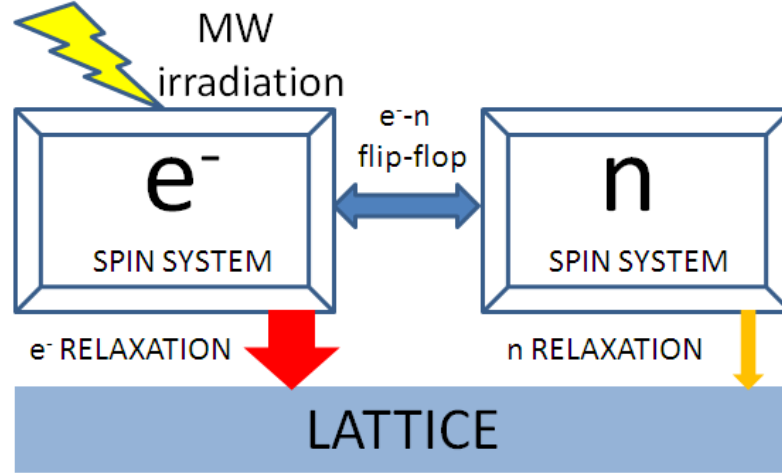


Figure 1.3: General DNP mechanism: microwaves saturate the ESR transition close to ω_0^e and then polarization is transferred through flip-flop electron-nuclear spin transition from electron spin to nuclear spin. Due to fast electron spin relaxation process, the polarization process is very efficient even with very low radical concentrations.

It is important to note that if on one side the electron spins polarize the nuclear spins, on the other side they are paramagnetic centers inducing faster relaxation of the nuclear spins them-self. To efficiently polarize the nuclear spins it is thus necessary to have the majority of them to be rather well isolated from the electron spins for most of the polarization time. One of the most important parameters to obtain the best polarization results is the ratio between nuclear spin and electron spin density. A too low electron density would lead to inefficient polarization while too high concentration would produce faster relaxation decreasing the maximum achievable polarization. The optimal concentrations also depend on the longitudinal relaxation times, that in turn is highly sensitive to the applied magnetic field \vec{B}_0 and the sample temperature.

As a rule of thumb, A. Abragam and M. Goldman⁵ obtained that to have the best polarization conditions, for solid dielectric samples with DNP, the following condition should be fulfilled:

$$(N_I T_1^e) / (N_S T_1^n) \ll 1 \quad (1.24)$$

where N_I and N_S are the concentration of nuclear and electron spins, respectively.

In metals and liquid solutions, the DNP process is caused by freely moving electrons. The interaction, involving only one nuclear spin and one electron spin, happens during a very short "contact" time and then the electron moves away before causing relaxation on the

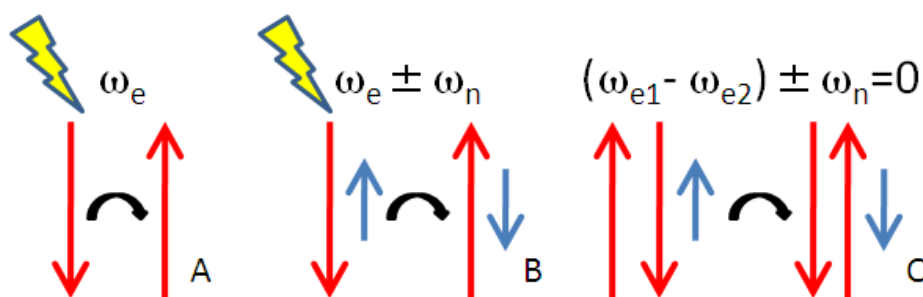


Figure 1.4: Different kind of flip and flip flop transitions: A) electron spin flip induced by MW irradiation at frequency ω_e ; B) two-spin system flip-flop process caused by off-resonance MW irradiation; the system is composed by one electron spin (red) and one nuclear spin (blue); C) three-spin flip-flop process with two electron spins (red) and one nuclear spin (blue); the difference in electron Zeeman energy matches the nuclear Zeeman energy.

just polarized nuclei. Conversely, in dielectric solids the electrons continuously polarize and let relax the spatially close nuclei. Then nuclear spin-spin dipolar interactions cause spin diffusion that will let the polarization flow to remote nuclear spins. The nuclei close to the electron experience a huge flip-flop rate and are not polarized; furthermore their resonance frequency is sensibly shifted by the presence of the electronic field thus making them not being detected at the bulk nuclei resonance frequency. The spin diffusion mechanism involves both dipolar and Zeeman spin diffusion. Some studies reported that dipolar spin diffusion is dominant with respect to Zeeman spin diffusion^{6,7}.

Typical DNP spin transitions

Spin transitions involving both electron spins and nuclear spins are essential to transfer polarization from electrons to nuclei in the DNP process. The fundamental transitions, shown in figure 1.4, can involve one or more electrons and one nucleus plus the electromagnetic perturbation used for the effective polarization transfer.

One-spin systems: the simplest spin system is composed of one spin (nuclear or electronic) with the resonance transition at its Larmor frequency. For electron spins, the microwave irradiation exactly at the electronic Larmor frequency, continuously stimulate transitions on both directions from the lower energy state (spin up) to the higher energy state (spin down), or the opposite with emission of one (or more) phonon with the same energy. Being the transition probability identical for both processes, if the irradiation power is large enough, an equalization of populations of both energy levels is obtained and thus the electron spins completely lose their polarization. This situation is schematically described in Figure 1.4-A.

Two-spins systems: three different types of two-spin systems can be defined and are all

involved in DNP: homonuclear transitions, electron-electron transitions and electron-nuclear transitions.

- as discussed in previous sections homonuclear transitions are at the origin of T_2 relaxation and spin diffusion mechanisms. Two nuclear spins, oppositely oriented, instantaneously change their orientation due to dipolar-dipolar interaction in a so called flip-flop transition. If we extend the basic idea of this process to a whole homonuclear spins system, we can depict the spin diffusion mechanism that allows polarization to diffuse from close to the electrons to the bulk solid-state sample structure;
- as for the homonuclear case, if two electron spins have the same transition energy and are close enough in space, electron-electron flip-flop transitions are allowed since they conserve both energy and angular momentum. Electronic flip-flop transitions are at the origin of electron T_2 relaxation;
- in case of heteronuclear system, the large difference in Zeeman energy between the electron and the nucleus, prevents the possibility of a single electron-nucleus flip-flop. As shown in Figure 1.4-B, microwaves irradiation at frequency $\omega_{MW} = \omega_e \pm \omega_n$ provides the missing energy allowing this kind of flip-flop transition. The nuclear spin flips (or flops) simultaneously with the electron spin. The hyperfine electron-nuclear spin interaction allows Zeeman energy to flow from the nuclear spins system to the electron spins system and vice-versa.

This type of interaction is at the origin of the Overhauser Effect and the Solid Effect.

Three spin system: the most important three-spin systems involved in DNP are ones composed by two electrons and one nucleus. To obtain transitions the Zeeman energy difference of electrons must match the nuclear Zeeman energy. This way the nuclear spin can provide (or absorb) the necessary energy to allow the two electronic spins to flip-flop. For this process to be possible, an ESR line-width larger than the nuclear resonance frequency is necessary; this way there are a non negligible amount of electronic spin couples with Zeeman energy difference matching the nuclear Zeeman energy thus producing a finite transition rate. These kind of transitions are the basis of Cross Effect and Thermal Mixing. Only Thermal Mixing will be discussed in the following being Cross Effect only a particular case of it.

Spin temperature

Now we introduce the concept of spin temperature T_S . A temperature can be associated to the populations distribution of each nuclear spin species through the Boltzmann distribution as did in equation 1.7.

Nuclear spin systems are relatively well isolated among them and from the lattice in the dielectric solids commonly used for DNP. Because of the very long $T_{1,n}$, it is possible to define a temperature associated to the nuclear spin population distribution T_S . This distribution can

be far from being in equilibrium with the sample (lattice) at temperature T_L . Thus the spin temperature T_S can be different from T_L .

In case of a two states spin system, we can define T_S as:

$$\frac{N_{-\frac{1}{2}}}{N_{\frac{1}{2}}} = e^{-\frac{\hbar\omega_0}{kT_S}} = e^{-\beta\omega_0} \quad (1.25)$$

where:

$$\beta = \frac{\hbar}{kT_S}. \quad (1.26)$$

is the inverse spin temperature. At thermal equilibrium, $T_S = T_L$.

Using equation 1.25 we can link the nuclear spin polarization to the spin temperature, in the high temperature approximation:

$$P = \frac{1}{2}\beta\omega_0 \quad (1.27)$$

In this description, P can assume negative values thus leading to negative temperatures. Negative temperatures are nonetheless allowed in this framework due to fact that the energy spectrum is limited.

Positive polarization and temperatures are linked with systems where the lower energy level is more populated, conversely negative polarizations and temperatures are linked to systems where the upper energy level is more populated.

It is possible to polarize positively or negatively the nuclei, depending on the microwave frequency used.

1.4 DNP mechanisms

Overhauser Effect

A.W. Overhauser in 1953 first predicted that nuclear spins can be polarized by the electron spins⁸. In the following years it has been shown experimentally that not only metals⁹, but also insulators doped with paramagnetic impurities¹⁰ can be polarized by DNP. Overhauser effect is based on the flip-flop transitions in two-spin systems consisting of one electron spin and one nuclear spin as depicted in figure 1.4-B. A microwave irradiation at the electron spin Larmor frequency is applied to saturate ESR transitions in figure 1.5. In the following electron spin relaxation, the nuclear spins are polarized through hyperfine coupling.

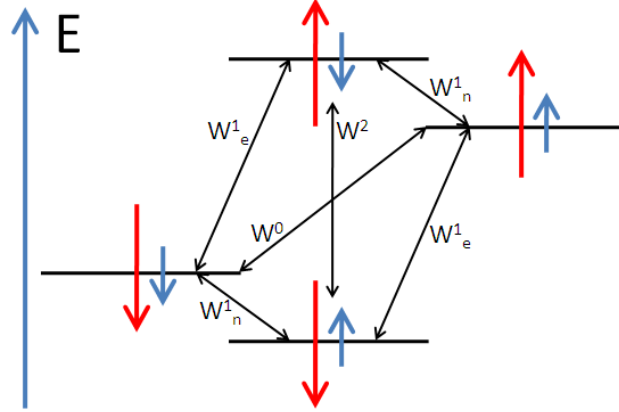


Figure 1.5: Schematics of energy levels and transitions of a two-spin system. It is composed by a nuclear spin (blue arrow) and an electron spin (red arrow). Black arrows represent transitions which rates are given by W^0 zero quantum flip-flop, W^2 double quantum flip-flip or flop-flop, W_n^1 single quantum nuclear relaxation and W_e^1 single quantum electronic relaxation.

The enhancement produced by the Overhauser effect can be obtained by solving the Solomon's rate equations³ and can be written as:

$$\epsilon = 1 - s\xi f \frac{|\gamma_S|}{\gamma_I} \quad (1.28)$$

where: s , the saturation parameter, is the electron spin saturation level; ξ , the coupling factor, affects the efficiency of the microwave power saturation; f , the leakage factor, is linked to the paramagnetic relaxation time of nuclei.

The coupling factor ξ can be expressed as:

$$\xi = \frac{W^2 - W^0}{W^0 + W^2 - 2W_n^1} \quad (1.29)$$

it can take values from -1, in the case of pure scalar coupling, to 0.5 in the case of a pure dipolar interaction.

The saturation parameter s is an indicator of how efficiently the ESR transition has been saturated and the electronic populations equalized. It can be expressed in term of the leftover

electronic magnetization in the z axis:

$$s = \frac{M_0 - \langle M_z \rangle}{M_0} \quad (1.30)$$

it can take values from $s = 0$ in case of no microwave irradiation to $s = 1$ if the microwave power is enough to equalize the electronic populations.

The leakage factor f accounts for the nuclear polarization lost because of the nuclear relaxation caused by the presence of the electron spins. It can be written as:

$$f = \frac{W^2 + W^0 + 2W_n^1}{W^0 + W^2 + 2W_n^1 + W_e^1} = 1 - \frac{T_{1n}^{+S}}{T_{1n}^{-S}} \quad (1.31)$$

where T_{1n}^{-S} is the pure nuclear longitudinal relaxation time in absence of electron spins, and T_{1n}^{+S} is the nuclear relaxation time decreased by the presence of electrons. In case s and f are equal to unity and $\xi = -1$, the enhancement factor from the Overhauser effect is only proportional to the electron-nuclear gyromagnetic constant ratio. This gives that the maximal theoretical enhancement factor can be $\epsilon_H \approx -660$ for 1H and $\epsilon_C \approx -2630$ for ^{13}C .

Solid Effect

The solid effect, in analogy to the Overhauser effect, is also based on electron-nucleus spin transitions. However, in this case the spin transitions are stimulated by the off-resonance microwave irradiation and take place at the same time.

To obtain the maximum polarization efficiency, the microwave frequency used must be equal to the relative difference (or sum) of the electron and the nuclear Larmor frequencies $\omega_{mw} = \omega_e \pm \omega_n$. This offset from the exact electron spin resonance produces a simultaneous transition of electron and nuclear spin as a flip-flop zero quantum transition if $\omega_{mw} = \omega_e - \omega_n$ or a flip-flip double quantum transition if $\omega_{mw} = \omega_e + \omega_n$. If in the Overhauser effect the microwave were stimulating transitions linked to W_e^1 , in the Solid Effect microwaves stimulate either W^0 or W^2 depending on the chosen frequency.

We refer to the polarization at frequency of $\omega_{mw} = \omega_e + \omega_n$ as negative DNP, due to the fact that it forces nuclear spin to populate the higher energy level thus giving $P < 0$. Conversely, the polarization at frequency $\omega_{mw} = \omega_e - \omega_n$ is referred as positive DNP.

The Solid Effect Hamiltonian can be written as:

$$H = -\omega_e S_Z - \omega_n I_Z + 2\omega_{1e} S_x \cos \omega t + \mathbf{S} \times \mathbf{A} \times \mathbf{I} \quad (1.32)$$

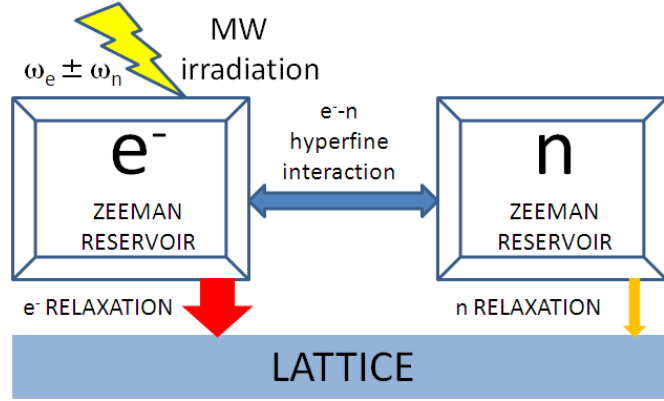


Figure 1.6: Flow chart describing the solid effect: the temperature of the Zeeman nuclear spin reservoir is lowered by the microwave irradiation at frequency $\omega = \omega_e \pm \omega_n$ through the electron Zeeman reservoir in contact through hyperfine electron-nuclear interaction.

where: the first term represents electron Zeeman energy; the second term represents the nuclear Zeeman energies; the third term represents the microwave irradiation; the last term accounts for the hyperfine coupling and \mathbf{A} is the hyperfine interaction tensor. From this expression, using perturbation theory, the transition rates equations can be obtained as¹¹:

$$\begin{aligned} W^+ &= 2\pi \frac{\omega_{1e}^2 |\frac{1}{4} A_{z+}|}{\omega_{0n}^2} \delta(\omega_{0e} + \omega_{0n} - \omega) \\ W^- &= 2\pi \frac{\omega_{1e}^2 |\frac{1}{4} A_{z+}|}{\omega_{0n}^2} \delta(\omega_{0e} - \omega_{0n} - \omega) \end{aligned} \quad (1.33)$$

where $A_{z+} = A_{zx} + i A_{zy}$. δ -functions account for energy conservation in the process and give the maximum transition rates when $\omega = \omega_{0e} \pm \omega_{0n}$.

In case of $\omega = \omega_{0S} + \omega_{0I}$, for the zero quantum transition rate equations we obtain:

$$\begin{aligned} \frac{\partial \rho_+^S \rho_-^I}{\partial t} &= -W^+ (\rho_+^S \rho_-^I - \rho_-^S \rho_+^I) \\ \frac{\partial \rho_+^S \rho_+^I}{\partial t} &= 0 \\ \frac{\partial \rho_-^S \rho_-^I}{\partial t} &= 0 \\ \frac{\partial \rho_-^S \rho_+^I}{\partial t} &= W^+ (\rho_+^S \rho_-^I - \rho_-^S \rho_+^I) \end{aligned} \quad (1.34)$$

where: ρ_{\pm} are ladder operators. The terms $\rho_{\pm}^S \rho_{\pm}^I$ represent the probability of the corresponding spin transitions.

Recombining equations and using the electron and nuclear spin polarization definitions,

we get:

$$\begin{aligned}\frac{\partial}{\partial t}(P_S + P_I) &= -2W^+(P_S + P_I) \\ \frac{\partial}{\partial t}(P_S - P_I) &= 0\end{aligned}\tag{1.35}$$

From the previous equation we obtained that P_I exponentially tends to negative electron spin polarization $-P_S$ with a characteristic time of $(2W^+)^{-1}$.

If the double quantum transition is stimulated with $\omega = \omega_{0S} - \omega_{0I}$, we obtain in analogy that the nuclear polarization exponentially grows towards $+P_S$ with a time constant of $(2W^-)^{-1}$.

Thermal mixing

Thermal Mixing is based on three-spin systems and makes use of the spin temperature formalism of introduced in section 1.3. If the electron spin concentration is larger, Thermal Mixing dominates in our sample, compared to Solid Effect. In this situation the electronic dipolar interactions are non-negligible and must be taken into account. The local magnetic field B_I produced by the electron spins dipolar field, at the site of other electrons, is non-negligible and thus the ESR line-width becomes larger.

With a larger ESR line, the probability to have electrons couples whose Zeeman energy difference matches the Zeeman energy of surrounding nuclear spins increases. This increases the efficiency of the Thermal Mixing process.

Now we introduce, according to the spin temperature formalism, several thermal reservoirs representing different and rather isolated energy systems: the Electronic Zeeman Reservoir (EZR), the Electronic Dipolar Reservoir (EDR) and the Nuclear Zeeman reservoir (NZR). The reservoirs are depicted in figure 1.7 along with the main interactions leading to Thermal Mixing.

EZR and NZR represent the Zeeman energy of the electronic and nuclear spins ensembles respectively. EDR accounts for the dipolar coupling energy of electronic spins. For each reservoir we can define a spin temperature, namely T_Z for EZR, T_{SS} for EDR and T_I for NZR. At thermal equilibrium $T_Z = T_{SS} = T_I = T_L$, meaning all spin temperatures are equal to the lattice temperature.

The whole Thermal Mixing can be split in two parts, namely dynamic cooling of EDR and thermal mixing between EDR and NZR^{5;12;13}.

The Thermal Mixing, similarly to the Solid Effect, is obtained by mean of off-resonance microwave irradiation. As seen in section 1.12, the off-resonance microwave irradiation at

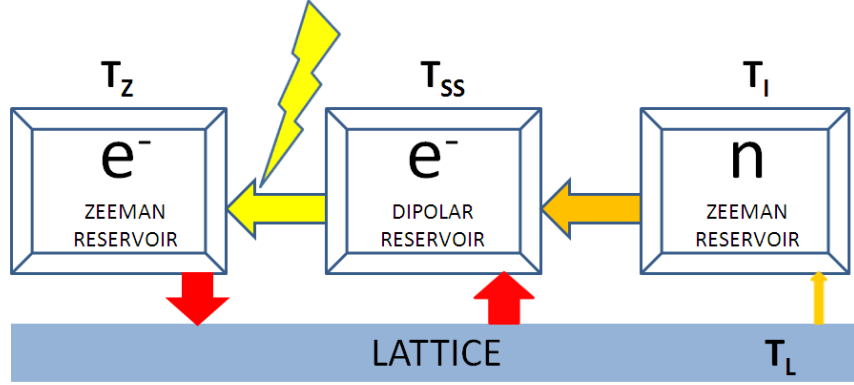


Figure 1.7: Heat flow chart describing thermal mixing: off-resonance microwave irradiation allows heat transfer from the electron dipolar reservoir to the electron Zeeman reservoir. Afterwards the electron dipolar reservoir, in thermal contact with the nuclear Zeeman reservoir, cools down the nuclear Zeeman reservoir lowering the nuclear spin temperature.

frequency ω decreases the effective field in the electrons rotating frame to:

$$\frac{B_{eff}}{B_0} = \frac{\omega_0 - \omega}{\omega_0} = \frac{\Delta}{\omega_0} \quad (1.36)$$

The sign of the spin temperature depends on that of $\Delta = \omega_0 - \omega$. The Zeeman spin temperature under microwave irradiation, T'_Z , is reduced by the same factor and is given by:

$$T'_Z = \frac{\Delta}{\omega_0} T_L \quad (1.37)$$

In the rotating frame, electron Zeeman energy of electrons is on the same range as the electrons dipolar coupling. In this situation we can have an energy exchange between EZR and EDR. Being the EZR temperature lower, the energy flow is toward this reservoir allowing for a decrease of the T_{SS} temperature of the EDR reservoir. This first step is called dynamic cooling. EDR final temperature can be estimated from the local magnetic field B_l :

$$T_f \approx \frac{B_l}{B_i} T_i \quad (1.38)$$

where B_i , T_i are the initial magnetic field and temperature.

Similarly to dynamic cooling, the thermal mixing process based on the three spin system of figure 1.4-C, allows to transfer energy from the NZR to the cooled EDR. The NZR temperature

is lowered thus obtaining an increased nuclear spin polarization. As we saw the efficiency of this energy transfer is linked to the line-width of the ESR spectrum and thus to the radical concentration.

During this process the Spin systems continue to relax to thermal equilibrium with the lattice. In particular for the NZR the leakage factor f (thin vertical arrow in Figure 1.7), linked to the nuclear T_1 is the direct relaxation rate of nuclear spin reservoir.

1.5 Hyperpolarization methods

Spin-Exchange Optical Pumping (SEOP)

The Spin-Exchange Optical Pumping is method is based on a two step process. In the first step, the valence electron shell of alkali metal atoms is polarized by means of angular momentum transfer of polarized optical electromagnetic waves. In the second step, the polarization of the polarized alkali vapors is transferred to noble gases nuclear spins through dipolar interactions during collisions. This way the gas spin polarization can be enhanced. Most of alkali atoms are suitable for SEOP since all of them have an unpaired valence electron, but Rubidium is usually used. One of the key conditions to obtain an efficient transfer is the collision rates between alkali nuclei and the gas to be polarized. To optimize this aspect high pressures are used. The temperature is controlled as well and kept high enough to obtain saturated rubidium vapor. Polarization up to 70 % with enhancements in the order of 10^5 have been reported^{14;15}.

From the biomedical point of view noble gases have some interesting properties: they are not harmful to biological tissues, they can easily enter and perfuse lungs and there are a complete absence of background being them absent in biological tissues. Furthermore noble gases T_1 's are very long in the range of hundreds of seconds^{16;17}. For all these reasons SEOP has mostly focused on lungs applications^{18;19}.

One of the noble gases used Xe . This nucleus has a quite high solubility in blood and in particular ^{129}Xe has been used in perfusion and diffusion studies of organs^{20;21} or tissues in both humans and rodents after intravenous injection²²⁻²⁴. ^{129}Xe has also been used within carrier structures²⁵⁻²⁸ able to target specific organs or diseased tissues. This improvement broadens the possible applications oh hyperpolarized gases in the MRI and molecular MRI field.

Para-Hydrogen Induced Polarization (PHIP)

The valence electrons in hydrogen molecule H_2 have the possibility to access two states: a singlet with total spin $S = 0$ or one of the three states of a triplet with total spin $S = 1$ ^{29;30}. Molecules in the first state are called para-hydrogen while molecules in the latter are called ortho-hydrogen. First order transitions between para- and ortho-hydrogen are forbidden

because they do not conserve the total spin S . At room temperature the populations are almost equalized at thermal equilibrium with about 25 % para-hydrogen and 75 % ortho-hydrogen. At low ($\sim 20\text{ K}$) temperature and with a catalizer, para-hydrogen population can be increased³¹. This polarization can then be transferred to nuclei by various methods.

Parahydrogen And Synthesis Allow Dramatically Enhanced Nuclear Alignment (PASADENA) is based on substrate hydrogenation, after the hydrogen molecules have been polarized, of molecules on a double carbon bond site³². The PASADENA method is applied normally at high magnetic field to break the para-hydrogen symmetry while retaining their spin-spin coupling.

PASADENA have been used for several MRI/MRS metabolic studies. As an example 1- ^{13}C -diethyl-succinate has shown to be polarized up to 17 % *in vitro*³³ and it has been as well used for *in vivo* imaging³⁴.

SABRE is another PHIP method that is based on the magnetization transfer from polarized para-hydrogen electrons to a substrate without chemical reactions³⁵. Various substrates ^{13}C labeled have been reported to be polarized by the SABRE method³⁶.

The main advantage of PHIP, to increase the MR sensitivity, is its capability to obtain polarized substrates in much less time than DNP. The major fields of PHIP application have been catalytic chemistry and drug developments.

1.6 Common methods for NMR measurements

In this section a brief presentation of common procedures used for NMR measurements in solid and liquid state are presented.

T_1 measurements

As seen in section 1.1 we defined the relaxation mechanisms involved in the T_1 longitudinal relaxation. To measure T_1 the thermal equilibrium magnetization along the z axis must be perturbed. Then its evolution back to equilibrium is followed. Several methods can be used to determine the longitudinal relaxation time T_1 in solid-state or liquid-state sample.

The standard methods to force the magnetization out of equilibrium are based on magnetization recovery or saturation recovery schemes that are widely used in high resolution NMR spectroscopy and *in vivo* MRI T_1 mapping. The evolution of the magnetization back to thermal equilibrium can be followed by applying a $\pi/2$ pulse in the XY plane at different time intervals following the preparation pulse (or series of pulses).

The T_1 of DNP-enhanced solid samples and hyperpolarized nuclei can be determined by monitoring the polarization decay. For instance, *in vitro* DNP NMR experiments can be performed to study the influence of the external conditions on the liquid-state ^{13}C T_1 of biomolecules of interest.

Inversion recovery scheme: a π pulse is used to perturb the system. It inverts the magnetization on the z axis from $+M_0$ to $-M_0$. Then the longitudinal relaxation exponentially brings back the magnetization to its equilibrium value. Various measurement, with a $\pi/2$ pulse and immediate afterward acquisition, with different recovery time T are performed to measure the residual magnetization on the z axis. The complete sequence can be seen in figure 1.8.

Bloch equations, introduced in section 1.2, are used to calculate the magnetization evolution and thus extract the T_1 value of the nuclear spins in exam. From equation 1.20 imposing the boundary conditions $M(0) = M_z(T = 0) = -M_0$ and $M(\infty) = M_z(T = \infty) = M_0$ the recovering magnetization M_{IR} can be written as:

$$M_{IR} = M_0 \cdot (1 - 2e^{-T/T_1}) \quad (1.39)$$

To obtain a precise determination of T_1 , T should cover a wide range of the order of $[0, 5 T_1]$.

Note that in between measurements, it is mandatory to wait a time that is long enough to allow the system to completely relax to equilibrium, typically $5 T_1$.

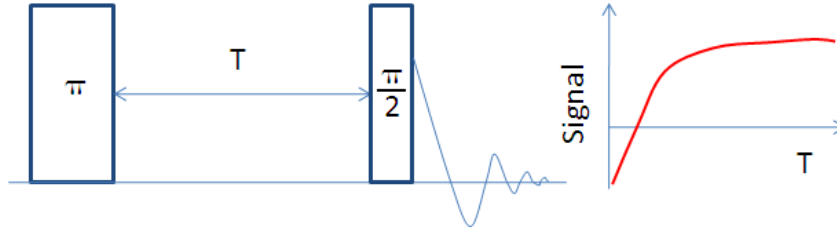


Figure 1.8: Inversion recovery pulses sequence (left) and typical magnetization recovery signal measured after the second $\pi/2$ pulse (right).

Saturation recovery scheme: in this case a saturation pulse is used to perturb the system, in place of the π pulse used in the inversion recovery scheme. Saturation pulses aim to obtain saturation in the system, meaning to equalize the spin populations thus completely destroying the magnetization. System saturation can be obtained by a single long RF pulse with enough intensity or alternately a series of π pulses that completely dephase the magnetization. After the saturation the sample magnetization is null.

The following part of the measurement is performed in the same way as for the inversion recovery scheme. In this case boundary conditions for Bloch equations are $M(0) = M_z(T = 0) = 0$ and $M(\infty) = M_z(T = \infty) = M_0$ and the polarization relaxation follows:

$$M_{SR} = M_0(1 - e^{-T/T_1}) \quad (1.40)$$

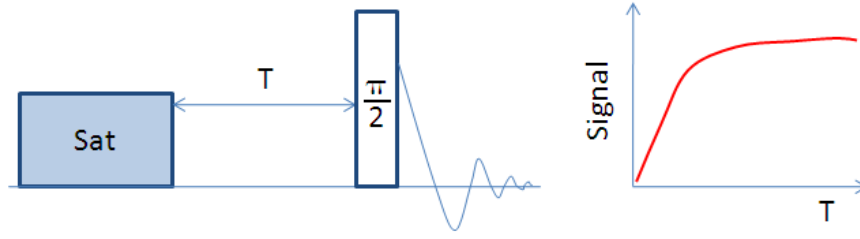


Figure 1.9: Saturation recovery pulses sequence (left) and typical magnetization recovery signal measured after the $\frac{\pi}{2}$ pulse (right).

On one side the saturation recovery scheme has the advantage of faster measurements since between them there is no need to wait for thermal relaxation. On the other hand it suffers from a resolution disadvantage since it covers, on the magnetization axis, only half of the range of the inversion recovery scheme.

Polarization decay scheme: the DNP-enhanced magnetization is much larger than in the thermal equilibrium state. The DNP-enhanced state is out of equilibrium, so after the DNP process stops, in analogy with the other two methods, the nuclear spin magnetization start to relax back toward thermal equilibrium. The time constant involved is again T_1 . Small RF pulses with flip angle θ are used every time interval T_r to determine the actual magnetization. Then from the decaying magnetization, T_1 can be extracted. In case of a negligible perturbing pulse, the magnetization signal measured at the n^{th} measurement can be written as,

$$M = M_0^P \cdot \sin\theta \cdot (e^{-T_r/T_1})^n \quad (1.41)$$

where M_0^P is the initial boundary condition for Bloch equations and represents the DNP-enhanced magnetization. The other condition is, as in the other cases, $M(\infty) = M_z(T = \infty) = M_0$.

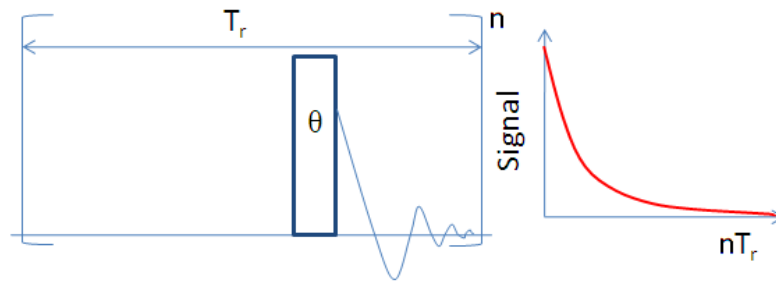


Figure 1.10: Polarization measurements with small flip angle θ (left) and typical magnetization decay signal measured just after the pulse (right).

In this scheme a single measurement lasting about $8 \sim 10 T_1$ is enough to determine T_1 .

In case of a non-negligible flip angle, the effect of the pulses on the magnetization must be accounted for using so-called RF correction:

$$T_1 = \frac{1}{\frac{1}{T'} + \frac{\ln \cos \theta}{T_R}}. \quad (1.42)$$

where T' is the pseudo-relaxation time, obtained by fitting the measured decays with a simple exponential function.

Solid-state DNP enhancement measurements

The solid-state DNP enhancement ϵ is defined as the ratio between the DNP enhanced polarization and the polarization of the system in thermal equilibrium.

$$\epsilon = \frac{P_{DNP}}{P_{thermal}} \quad (1.43)$$

Experimentally, to determine ϵ , we need to compare the signal from the DNP enhanced system (obtained for example from the first point of the polarization decay), to the signal obtained from the system after the thermal equilibrium has been established.

To determine the thermal signal we first have to wait until the system has fully relaxed to thermal equilibrium, typically after about $5 T_1$. Then we perform a single signal measurement. Since normally the thermal signal is very small compared to the DNP polarized one, the flip angle used is exactly $\pi/2$ to obtain the maximum signal. Nevertheless in many occasions, to obtain a good precision, this measurement has to be repeated and averaged to increase the Signal-to-Noise Ratio (SNR).

In Figure 1.11 we show the measurement scheme for n averages of the thermal signal.

At this point the enhancement can be calculated from the DNP polarized signal, considering the different flip angle used, with:

$$\epsilon = \frac{S_{DNP}}{S_{thermal} \cdot \sin \theta} \quad (1.44)$$

where: S_{DNP} is the DNP enhanced signal; $S_{thermal}$ is the averaged thermal signal; θ is the flip angle used in the DNP enhanced signal determination.

We underline that, even in cases where the thermal signal is very high and a single measurement is enough for a good determination, the time needed for the measurement is at least $5 T_1$ independently from the signal intensity. This because in this scheme the measurement

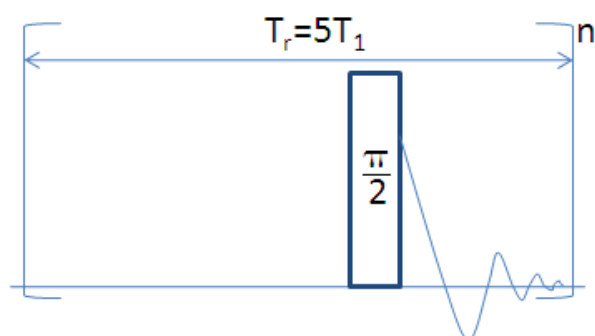


Figure 1.11: Thermal signal measurements with a $\pi/2$ pulse after the system has fully relaxed to equilibrium.

needs to be done when the system has completely relaxed to thermal equilibrium.

In solid-state experiments, where the T_1 can be of the order of hours, this method to determine the thermal signal can become unpractical and extremely time consuming.

References

- [1] F. Bloch, W. W. Hansen, and M. Packard. Nuclear induction. *Physical Review*, 69(3-4):127–127, 1946.
- [2] N. Bloembergen, E. M. Purcell, and R. V. Pound. Relaxation effects in nuclear magnetic resonance absorption. *Physical Review*, 73(7):679–712, 1948.
- [3] I. Solomon. Relaxation processes in a system of 2 spins. *Physical Review*, 99(2):559–565, 1955.
- [4] L. Helm. Relaxivity in paramagnetic systems: Theory and mechanisms. *Progress in Nuclear Magnetic Resonance Spectroscopy*, 49(1):45–64, 2006.
- [5] A. Abragam and M. Goldman. Principles of dynamic nuclear-polarization. *Reports on Progress in Physics*, 41(3):395–467, 1978.
- [6] W. Zhang and D. G. Cory. First direct measurement of the spin diffusion rate in a homogeneous solid. *Physical Review Letters*, 80(6):1324–1327, 1998.
- [7] G. S. Boutis, D. Greenbaum, H. Cho, D. G. Cory, and C. Ramanathan. Spin diffusion of correlated two-spin states in a dielectric crystal. *Physical Review Letters*, 92(13), 2004.
- [8] A. W. Overhauser. Polarization of nuclei in metals. *Physical Review*, 91(2):476–476, 1953.
- [9] T. R. Carver and C. P. Slichter. Polarization of nuclear spins in metals. *Physical Review*, 92(1):212–213, 1953.
- [10] A. Abragam. Overhauser effect in nonmetals. *Physical Review*, 98(6):1729–1735, 1955.
- [11] W. T. Wenckebach. Dynamic nuclear polarization using strong microwave fields, 2012.
- [12] S. T. Goertz. The dynamic nuclear polarization process. *Nuclear Instruments & Methods in Physics Research Section a-Accelerators Spectrometers Detectors and Associated Equipment*, 526(1-2):28–42, 2004.
- [13] M. Goldman. Overview of spin temperature, thermal mixing and dynamic nuclear polarization. *Applied Magnetic Resonance*, 34(3-4):219–226, 2008.
- [14] M. S. Albert, G. D. Cates, B. Driehuys, W. Happer, B. Saam, C. S. Springer, and A. Wishnia. Biological magnetic-resonance-imaging using laser polarized Xe-129. *Nature*, 370(6486):199–201, 1994.
- [15] H. Middleton, R. D. Black, B. Saam, G. D. Cates, G. P. Cofer, R. Guenther, W. Happer, L. W. Hedlund, G. A. Johnson, K. Juvan, and J. Swartz. MR-imaging with hyperpolarized He-3 gas. *Magnetic Resonance in Medicine*, 33(2):271–275, 1995.
- [16] A. K. Venkatesh, L. Zhao, D. Balamore, F. A. Jolesz, and M. S. Albert. Evaluation of carrier agents for hyperpolarized xenon MRI. *Nmr in Biomedicine*, 13(4):245–52, 2000.
- [17] A. Bifone, Y. Q. Song, R. Seydoux, R. E. Taylor, B. M. Goodson, T. Pietrass, T. F. Budinger, G. Navon, and A. Pines. NMR of laser-polarized xenon in human blood. *Proc Natl Acad Sci U S A*, 93(23):12932–6, 1996.
- [18] X. J. Chen, H. E. Moller, M. S. Chawla, G. P. Cofer, B. Driehuys, L. W. Hedlund, and G. A. Johnson. Spatially resolved measurements of hyperpolarized gas properties in the lung in vivo. Part I: diffusion coefficient. *Magn Reson Med*, 42(4):721–8, 1999.
- [19] X. J. Chen, H. E. Moller, M. S. Chawla, G. P. Cofer, B. Driehuys, L. W. Hedlund, J. R. MacFall, and G. A. Johnson. Spatially resolved measurements of hyperpolarized gas properties in the lung in vivo. Part II: t_2^* . *Magn Reson Med*, 42(4):729–37, 1999.
- [20] B. M. Goodson, Y. Song, R. E. Taylor, V. D. Schepkin, K. M. Brennan, G. C. Chingas, T. F. Budinger, G. Navon, and A. Pines. In vivo NMR and MRI using injection delivery of laser-polarized xenon. *Proc Natl Acad Sci U S A*, 94(26):14725–9, 1997.

- [21] G. Duhamel, P. Choquet, E. Grillon, L. Lamalle, J. L. Leviel, A. Ziegler, and A. Constantinesco. Xenon-129 MR imaging and spectroscopy of rat brain using arterial delivery of hyperpolarized xenon in a lipid emulsion. *Magn Reson Med*, 46(2):208–12, 2001.
- [22] J. Wolber, D. J. McIntyre, L. M. Rodrigues, P. Carnochan, J. R. Griffiths, M. O. Leach, and A. Bifone. In vivo hyperpolarized ^{129}Xe NMR spectroscopy in tumors. *Magn Reson Med*, 46(3):586–91, 2001.
- [23] B. Driehuys, H. E. Moller, Z. I. Cleveland, J. Pollaro, and L. W. Hedlund. Pulmonary perfusion and xenon gas exchange in rats: MR imaging with intravenous injection of hyperpolarized ^{129}Xe . *Radiology*, 252(2):386–93, 2009.
- [24] B. Driehuys, S. Martinez-Jimenez, Z. I. Cleveland, G. M. Metz, D. M. Beaver, J. C. Nouns, S. S. Kaushik, R. Firszt, C. Willis, K. T. Kelly, J. Wolber, M. Kraft, and H. P. McAdams. Chronic obstructive pulmonary disease: safety and tolerability of hyperpolarized ^{129}Xe MR imaging in healthy volunteers and patients. *Radiology*, 262(1):279–89, 2012.
- [25] M. M. Spence, S. M. Rubin, I. E. Dimitrov, E. J. Ruiz, D. E. Wemmer, A. Pines, S. Q. Yao, F. Tian, and P. G. Schultz. Functionalized xenon as a biosensor. *Proc Natl Acad Sci U S A*, 98(19):10654–7, 2001.
- [26] M. M. Spence, E. J. Ruiz, S. M. Rubin, T. J. Lowery, N. Winssinger, P. G. Schultz, D. E. Wemmer, and A. Pines. Development of a functionalized xenon biosensor. *J Am Chem Soc*, 126(46):15287–94, 2004.
- [27] G. K. Seward, Q. Wei, and I. J. Dmochowski. Peptide-mediated cellular uptake of cryptophane. *Bioconjug Chem*, 19(11):2129–35, 2008.
- [28] J. M. Chambers, P. A. Hill, J. A. Aaron, Z. Han, D. W. Christianson, N. N. Kuzma, and I. J. Dmochowski. Cryptophane xenon-129 nuclear magnetic resonance biosensors targeting human carbonic anhydrase. *J Am Chem Soc*, 131(2):563–9, 2009.
- [29] D. M. Dennison. A note on the specific heat of the hydrogen molecule. *Proceedings of the Royal Society of London Series a-Containing Papers of a Mathematical and Physical Character*, 115(771):483–486, 1927.
- [30] K. F. Bonhoeffer and P. Harteck. Experiments on para-hydrogen and ortho-hydrogen. *Naturwissenschaften*, 17:182–182, 1929.
- [31] S. B. Duckett and N. J. Wood. Parahydrogen-based NMR methods as a mechanistic probe in inorganic chemistry. *Coordination Chemistry Reviews*, 252(21-22):2278–2291, 2008.
- [32] C. R. Bowers and D. P. Weitekamp. Para-hydrogen and synthesis allow dramatically enhanced nuclear alignment. *Journal of the American Chemical Society*, 109(18):5541–5542, 1987.
- [33] E. Y. Chekmenev, J. Hovener, V. A. Norton, K. Harris, L. S. Batchelder, P. Bhattacharya, B. D. Ross, and D. P. Weitekamp. PASADENA hyperpolarization of succinic acid for MRI and NMR spectroscopy. *Journal of the American Chemical Society*, 130(13):4212–4213, 2008.
- [34] Niki M. Zacharias, Henry R. Chan, Napapon Sailasuta, Brian D. Ross, and Pratip Bhattacharya. Real-time molecular imaging of tricarboxylic acid cycle metabolism in vivo by hyperpolarized 1- ^{13}C diethyl succinate. *Journal of the American Chemical Society*, 134(2):934–943, 2011.
- [35] R. W. Adams, J. A. Aguilar, K. D. Atkinson, M. J. Cowley, P. I. P. Elliott, S. B. Duckett, G. G. R. Green, I. G. Khazal, J. Lopez-Serrano, and D. C. Williamson. Reversible interactions with para-hydrogen enhance NMR sensitivity by polarization transfer. *Science*, 323(5922):1708–1711, 2009.
- [36] Lyrelle S. Lloyd, Ralph W. Adams, Michael Bernstein, Steven Coombes, Simon B. Duckett, Gary G. R. Green, Richard J. Lewis, Ryan E. Mewis, and Christopher J. Sleight. Utilization of SABRE-derived hyperpolarization to detect low-concentration analytes via 1D and 2D NMR methods. *Journal of the American Chemical Society*, 134(31):12904–12907, 2012.

2 Polarizer development and test

Abstract

In this chapter we present the development on cryogenic, hardware and software sides of a new DNP prepolarizer based on a previous design by the SEPT group of PSI and already installed at CIBM. The cryogenic system details were reviewed, following the operational principles and procedures of a common dissolution DNP experiment, highlighting the hardware differences between the new design and the already installed PSI cryostat. The cryostat was tested to determine the cryogenic properties, the time needed and the helium consumption of the different operations routinely performed. Based on these tests the operational parameters were optimized to obtain the best compromise between helium consumption and cooldown time. Finally a discussion on the improvements and drawbacks of the new design is given.

2.1 Hardware

The complexity of dissolution DNP, which includes cryogenics, microwaves and magnetic resonance techniques makes the DNP experimental setup quite sophisticated. The dissolution DNP method and its associated instrumentation were first introduced by Ardenkjaer-Larsen et al¹. Unlike the commercially available polarizer Hypersense™, the polarizer described in the present chapter and used in the frame of this thesis is based on a separate cryostat inserted inside the bore of a standard room-temperature wide-bore superconducting magnet^{2;3}.

A previous continuous flow cryostat design was developed by the Sample Environment and Polarised Targets (SEPT) group of the Paul Scherrer Institute (PSI) and is used almost every day for *in vitro* and *in vivo* NMR experiments in the 9.4 T horizontal bore NMR imager of the CIBM^{2;4}. Using the SEPT cryostat as a starting point, a new design of DNP prepolarizer based on a continuous flow cryostat was developed. The development of the new prepolarizer setup was focused on improving the automation and the speed of procedures used for instance the cooldown period, while retaining the optimal performance characteristics of the already installed setup.

Cryogenic scheme

The cryostat shown in figure 2.1 is the original design developed by the PSI. The new cryostat is a slightly modified version of this design following the same principles.

The cryostat consists of two parts: the insulation dewar (a) and the main insert (b) where all the flow regulations are managed. The liquid helium coming from the external storage dewar through the transfer line in (b2), is on the first stage condensed in the separator (b1), an intermediate chamber used both to keep the top part of the cryostat (a1) cold and to remove the helium evaporated during the transfer. The separator is pumped through a capillary (b3) wrapped around the top part of the cryostat; the flow of cold helium in this capillary is used to cool down the baffles (b6) and the radiation screens (a3) in the Outer Vacuum Chamber (OVC) of the cryostat. The main volume of the cryostat (a2), where the sample will be placed and polarized, is connected to the separator through another capillary (b4), wrapped around the tail of the cryostat insert. This capillary can be opened or closed through a needle valve (b5) manually operated from outside.

The main differences between the new design and the original PSI design are:

- the material used for the separator. Thick brass used for separator walls was replaced with thin stainless steel, thus decreasing the heat capacity of the separator;
- a sintered plate was added in the separator to separate the liquid helium from the gas evaporated during the transfer;
- the location and material of the baffles. The double-sided printed circuit boards covered

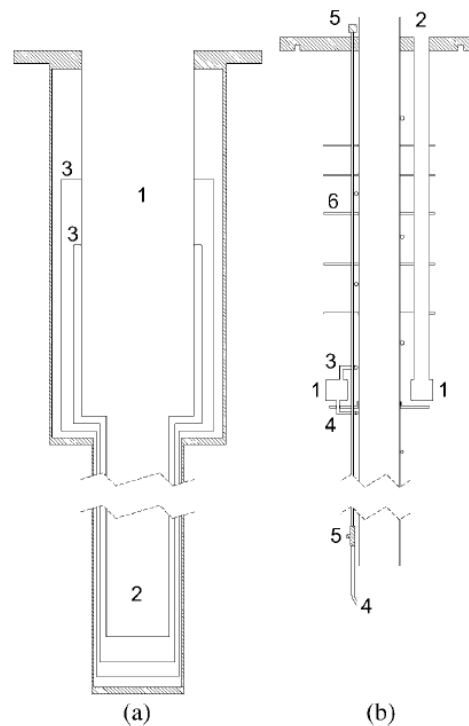


Figure 2.1: Schematic drawings of the PSI cryostat. (a) Vacuum mantle, with two heat shields in the Outer Vacuum Chamber (OVC). (b) The main insert. Figure adapted with permission from Comment et al⁴.

with a thin copper layer were replaced with bulk copper discs;

- the radiation shields were anchored at slightly different location and super-insulation foils were added in the OVC to further decrease the thermal losses;

Those design modifications led to a substantial difference in behavior which will be highlighted at the end of the chapter.

Pumping lines and connections

The cryostat is operated through a rather complex pumping system with three sets of pumps, monitored and operated in different points with electronic and electro-mechanic instruments.

The cryostat, as shown in figure 2.2, has five main ports through which the pumping system is connected:

OVC pumping: one outlet is used to keep the insulating chamber of the cryostat to a high vacuum level. The pumping system used is composed by a turbo-molecular pump

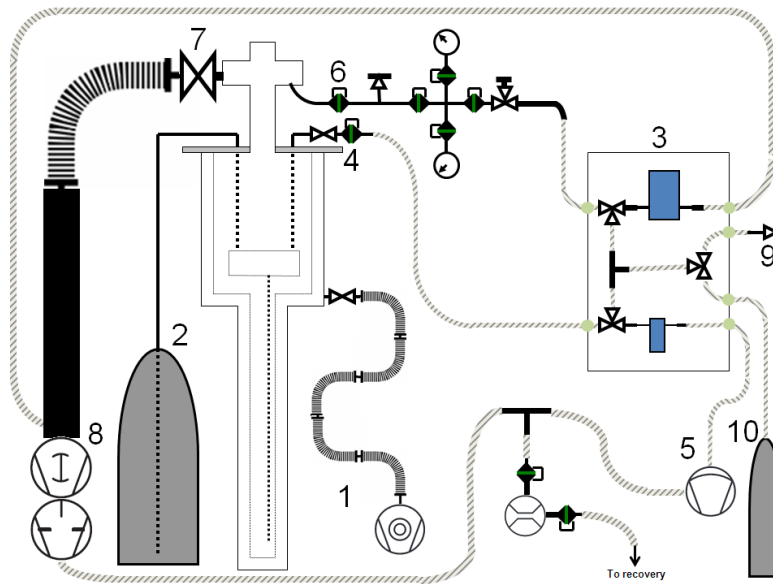


Figure 2.2: Schematic drawing of the pumping lines and instruments used to control and monitor the cryogenic operations on the cryostat.

backed up by a rotary pump (1). This pumping line is always active and not related to the cryostat operations;

Transfer line inlet: the only inlet of the cryostat comes from the storage dewar (2) that provides the liquid helium for the cooldown and the cryogenic operations. This port is directly connected to the separator;

Separator outlet: the separator itself is directly connected to the flow-box (3) through the port (4). This line is used to pump the helium gas evaporated during the transfer from the storage dewar to the Separator, through a $35 \text{ m}^3/\text{h}$ Edwards XDS35i membrane pump (5). The same port is as well used to pressurize the separator in case it has to be opened to replace an empty storage dewar. These operations are managed by the software through the flow-box hardware;

Sample Space outlet: port (6) connects, similarly to the Separator outlet (4), the Sample Space to the flow-box (3). The line is used for various purposes: to pump the Sample Space in order to reach a low vacuum for cooldown or transfer liquid helium; to connect the Sample Space to an overpressure valve to get rid of the helium boiloff when the Sample Space is not pumped; to pressurize the Sample Space during the operations that require to open the cryostat to prevent air from entering the system. Again, these operation are software controlled.

On this port the two manometers sit to monitor the pressure in the low vacuum range during normal operations and in the middle vacuum range during polarization.

High flow pumping outlet: port (7) is a KF-50 VAT manual valve directly connecting the Sample Space to the high flow pumping system (8) to achieve the minimum pressure, and

thus temperature, possible in the Sample Space to perform the polarization. The pumping system (8) is composed by a $250\text{ m}^3/\text{h}$ Pfeiffer WKP250A roots pump backed up by a $65\text{ m}^3/\text{h}$ Balzers DUO 65 rotary pump;

The flow-box (3), interfaced with the electronic control box, is used to manage the proper line connections depending on the state of the cryostat. Furthermore, it controls the pumping speed through two flowmeters from the Sample Space and from the Separator respectively. The outlet connections on the right side go, from top to bottom:

- to the main pumping line of (8);
- to an overpressure valve (9) used to keep the cryostat slightly pressurized during the normal helium boil-off;
- to a low pressure helium bottle (10) used to re-pressurize the Sample Space after a pumping operation or if it has to be opened to air;
- to the membrane pump (5).

Polarization insert and blowover

In this section we present the part of the setup used to polarize the sample, measure NMR solid-state signal and perform the dissolution to obtain the hyperpolarized solution.

The different inserts used for polarization are shown in figure 2.3. The inserts arrangement is composed by a fiberglass sample insert (A) where the sample cap is placed (1). Then the gold plated waveguide (B) is inserted into (A) to drive the microwaves from the source outside the cryostat to irradiate the sample.

Finally the sample insert is placed into the NMR insert (C), beforehand placed into the cryostat prior to the cooldown procedure.

At the bottom of the NMR insert sits an over-moded gold plated microwave cavity (2a), located at the isocenter of the magnet. It is designed to allocate the sample insert in order to place the sample exactly at the magnet isocenter. The gold layer inside the waveguide and the microwave cavity reduces the absorption of the microwaves by the surfaces and then increases the microwave power delivered to the sample for a given output power produced by the source. Saturation of the electron spin system is thus possible with less microwave output power. The reduced microwave absorption of the surfaces, as well as the reduced microwave source output power, help minimizing the heat brought from the microwaves to the helium bath thus decreasing the liquid helium evaporation. The NMR circuit is roughly tuned *in situ* with fixed capacitors (2b). The circuit is connected to outside the cryostat through a rigid coaxial cable. At the exit a tuning system composed of a coaxial cable and two variable capacitors is used for the fine tuning. This setup was described and discussed in details in a previous publication⁴.

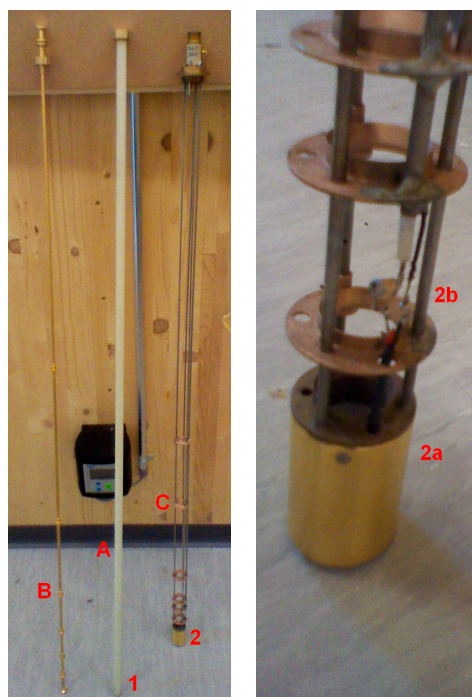


Figure 2.3: Inserts used in the cryostat for polarization. Left: A) sample insert, (1) is the location of the sample; B) gold plated microwave waveguide; C) NMR insert, (2) is the over-moded gold plated microwave cavity in the isocenter of the magnet. Right: detail of the microwave cavity (2a) and of the resonant circuit fixed capacitors (2b).

At the end of the solid-state polarization, the sample placed in the helium bath has to be extracted and transformed into a room-temperature aqueous solution to be injected *in vivo* or used for *in vitro* experiments. In figure 2.4-left the dissolution insert is shown. It is used to prepare high pressure water steam inside a boiler in figure 2.4-right. After inserting the dissolution insert into the sample insert, the steam is released onto the frozen sample to dissolve it. The geometry of the tip of the dissolution insert is designed to tightly fit the sample cup preventing steam to escape into the cryostat. The dissolved sample is then extracted from the cryostat using high pressure helium gas. The procedure has been described in previous publication².

The electro-pneumatic valves (A) installed on the dissolution insert are controlled remotely and the timing is preset. Deuterated water is introduced through the valve (F) into the boiler (D) with a syringe. Then by mean of the pneumatic valves (A), compressed helium coming through (B) is used to pressurize the boiler (normal pressure is in the range 5 – 8 bar). The boiler is heated by a resistive wire wrapped around and protected by the white teflon piece. During heating, temperature and pressure are monitored with the manometer (C) and with a *Pt100* resistor placed on top of the boiler. The box (G) contains the electrical connections from the instruments to the electronic box. When the boiler reaches the desired pressure and temperature, the dissolution can be initi-

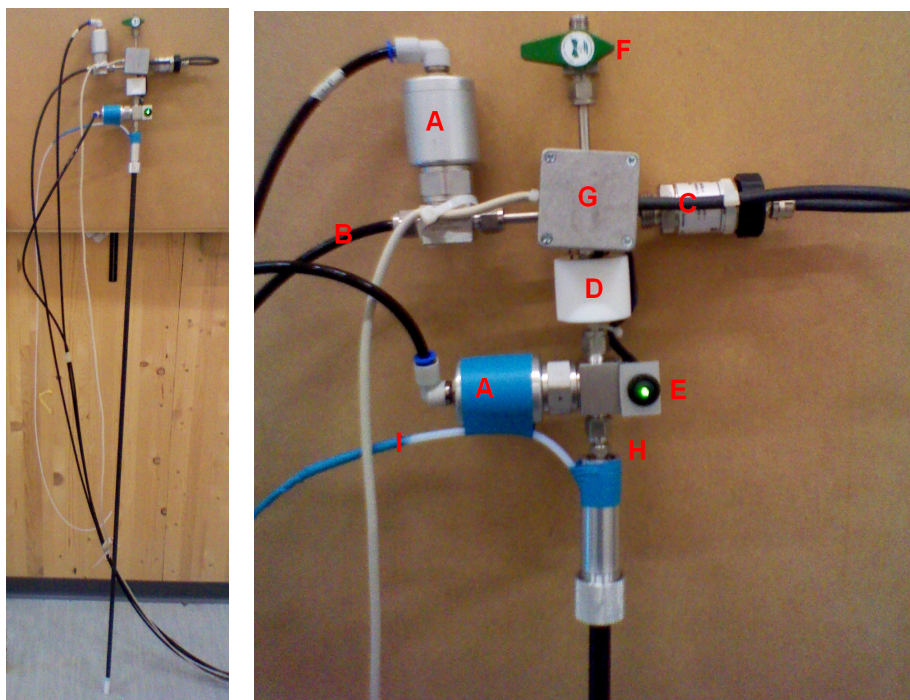


Figure 2.4: Dissolution insert used to extract the frozen sample from the cryostat in the form of a room temperature aqueous solution. Right: detail of the top cross of the insert.

ated. The operator triggers the dissolution by simply pressing a push button (E). When the dissolution sequence starts, the steam is pushed down through the Swagelok outlet (H) and the dissolved sample comes out through the 2 mm inner diameter teflon tube (I).

In order to limit as much as possible the polarization losses, it is important to perform the dissolution of the sample at high field and in the shortest time possible, so to say directly in the cryostat close to the magnet isocenter. As soon as the microwaves irradiation is stopped the spin polarization starts to decrease, relaxing toward equilibrium. In addition to the total dissolution time, the other key parameter controlling the overall polarization loss during dissolution is the longitudinal relaxation time. T_1 's of most nuclei of biological interest is lower at low field, thus enhancing the relaxation. Performing the dissolution at high field in the cryostat, allows to minimize the overall time and to keep the T_1 of the sample as high as possible, minimizing the polarization losses.

2.2 Cryogenic performances

The cryostat performances were tested and the procedures, described in Appendix A, optimized to obtain the best compromise between cooling speed and helium consumption. The parameters leading to the longest helium hold time during the DNP process were also determined.

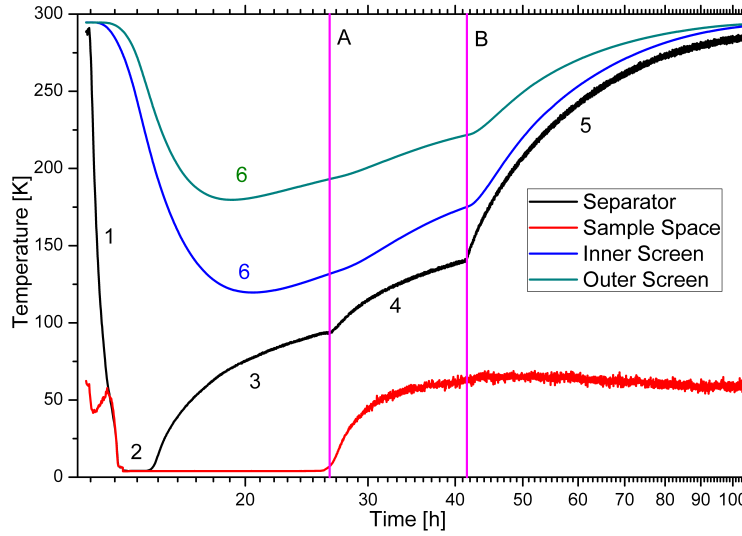


Figure 2.5: Temperature monitoring of the different cryostat parts during a complete cooldown cycle. 1) cooldown; 2) hold time (helium in Separator); 3) holdtime (standby); 4) warmup (standby); 5) warmup (idle); 6) OVC screens cooling; A) liquid helium finished in the Sample Space; B) storage dewar removed; Note: the Sample Space temperature resistor calibration is not reliable above 40 K.

The evolution of temperatures of the different parts of the cryostat during a complete cryogenic cycle are presented in figure 2.5. The cycle starts with a cooldown procedure immediately followed by a filling procedure. Then the cryostat is maintained in a standby state for about a day following the complete evaporation of liquid helium introduced into the Sample Space. Finally the storage dewar was disconnected from the cryostat and the system warmed up.

Cooldown

To optimize the cooldown procedure, several strategies were tested, with different flow values from the Separator and the Sample Space:

- using protocols with low pumping flows (as an example 20 *SLPM* on Sample Space and 2 *SLPM* on the Separator) the pressure in the Sample Space remains only slightly lower than ambient pressure. The cooldown procedure is slow (several hours) and, although a lower helium consumption rate ($< 2 \text{ l/h}$ of liquid helium), the amount of helium required for cooling the system is large ($> 10 \text{ l}$ over several hours); furthermore, the temperature of the cryostat top plate decreases below -20°C , which indicates that a non negligible part of the cooling power is wasted;
- using protocols with high pumping flows (as an example $> 80 \text{ SLPM}$ on Sample Space and $> 6 \text{ SLPM}$ on the Separator) the pressure in the Sample Space is lowered (200 *mbar*

or less). The cooldown procedure is fast but never shorter than one hour; on the other hand the helium consumption rate severely increases (9 l or higher) when the pumping flow is set too high and the top plate temperature also decreases dramatically, indicating again a poor efficiency of the cooling protocol.

The best strategy is therefore to adjust the pumping flows to intermediate values that are dynamically adjusted during cooldown:

- when the cryostat is warm, a high flow is established inside the Sample Space (70 *SLPM* on Sample Space and 6 *SLPM* on the Separator), maintaining a Sample Space pressure in the range $300 \approx 400 \text{ mbar}$; even if the flow is set to a high value, due to the high temperature difference, a large amount of heat can be transferred from the inner walls of the cryostat to the cold helium gas, thus having the helium gas relatively warm at the output of the cryostat;
- while the cryostat is cooled, the flow in the Sample Space is progressively reduced down to about 40 *SLPM* and the pressure increases (close to atmospheric pressure when temperature reaches liquid helium region). The pumping speed was chosen in order to complete the cooldown before the top plate temperature falls too low. Typically at the end of the cooldown procedure the top plate reaches about 0°C .

The whole optimized cooldown procedure shown in figure 2.5-1 takes place in as short as 1.5 hours with an overall helium consumption of about 5 liters.

Filling

The filling procedure was optimized in order to use the minimum amount of helium and perform a fast and efficient transfer. The best strategy found consists in performing the transfer as fast as possible with the highest pumping flow on the Sample Space. The idea is to minimize the period during which there is a high liquid helium evaporation rate since the gas pumped out from the Sample Space is cold and tends to freeze the main insert top plate. Using this strategy it is possible to transfer enough liquid helium to fill the cryostat in as little as ten minutes: about 1.5 liters of liquid helium is transferred into the cryostat and only less than 0.5 liters are lost because of evaporation.

Hold-time

Although the cryostat can be used in continuous flow mode, an important characteristic is the maximum amount of time it can hold liquid helium without refilling. To determine this hold time, the Sample Space was filled and then isolated from the Separator by closing both needle valves and finally the cryostat was put in standby state. The flow pumped through the

Chapter 2. Polarizer development and test

Separator (3 *SLPM*) was optimized to keep a low temperature on the top part of the cryostat, thus decreasing the upward heat leakage to the Sample Space.

While the liquid helium in the Sample Space evaporated, two regimes were observed in terms of the Separator temperature (numbers refer to figure 2.5):

- (2) : for about 1.5 hours the Separator still contained liquid helium thus stabilizing its temperature to 4.2 *K*.
- (3) : once empty, only the flow of cold helium gas transferred from the storage dewar maintained the Separator cold. The Separator temperature started to rise in an approximately exponential fashion, with a characteristic time constant of about 3.5 hours and a limit Separator temperature below 100 *K*.

The cryostat hold time at atmospheric pressure was found to be on the order of 13 hours without refilling. During all this period the Separator was pumped with a flow of 3 *SLPM*.

If the membrane pump is stopped and the Separator is connected to the recovery line, the Separator temperature still rises in an approximately exponential fashion, but with a lower time constant and a higher limit temperature. The hold time also decreased significantly to about 8-9 hours. During the polarization, the microwaves shined on the sample increase the helium boiloff. The hold time decreases from 13 hours to about 8 hours thus remaining long enough for almost all the dissolution DNP applications.

Using the cryostat in continuous flow mode or refilling the Sample Space when the level becomes too low, the polarization time can be extended to an arbitrarily long period, as previously described².

Warmup (Standby)

Once all the liquid helium has evaporated (figure 2.5-A), the cryostat starts warming up: both the Sample Space and the Separator temperatures increase, meaning that the flow on the Separator is not sufficient to keep it cold (figure 2.5-4).

The Sample Space quickly warms up in an exponential fashion with an estimated characteristic time constant of about one hour, within the temperature region where the measuring resistor calibration is reliable $T_{SS} < 40\text{ K}$.

The characteristic time of the temperature evolution of the Separator more than doubles up to (8-9 hours) with respect to the period during which liquid helium was present in the Sample Space and the limit Separator temperature rises to about 150 *K*.

Warmup (Idle)

After the cryostat was disconnected from the dewar (figure 2.5-B), the characteristic time of the Separator temperature evolution was about 16 hours. Thus, even after one day, the

system was still at a rather low temperature, and during this period it can be cooled down faster than it was at room temperature (less than 1.5 hours).

Radiation Screens

The radiation screens behavior shows that although the inner part of the cryostat can be cooled fast and liquid helium can be maintained inside the Sample Space, the screens have a much longer cooldown time constant due to the efficient insulation (figure 2.5-1).

We observed a quite long delay between the beginning of the cooldown and a notable temperature drop of the screens (about 2 hours). Then it takes more than one full day until the screens temperature reach a steady state (figure 2.5-6). Afterwards, their behavior follows quite rightly the one of the Separator: this can be easily explained since the screens are thermally anchored to the top part of the cryostat.

This behavior indicates that the best cryogenic performances in terms of the minimum radiation leakage through the cold screens and thus the longest hold-time, can be achieved after one day of operation. This observation suggests that the performances could be improved by a continuous use of the cryostat, although a good hold-time was achieved even after the first cooldown.

2.3 Conclusions

In this chapter the details of the development and installation of the cryogenic and dissolution hardware of the new prepolarizer setup were thoroughly discussed, together with a presentation of the main operations performed during a typical dissolution DNP polarization. The cryogenic tests, following the optimizations, show that the procedures optimized for this prepolarizer need significantly less time than the procedures actually performed on the prepolarizer already installed² to reach 4.2 K inside the Sample Space and for the initial filling. A reason for the increased cooling speed of the Sample Space is most likely linked to the lower thermal inertia of the Separator. It however has to be highlighted that the radiation screens are still quite warm during the initial filling and the initial helium consumption is larger than in the PSI design. One of the drawback of this new design is that it tends to warm up faster if the Sample Space is empty, again most likely because of the lower thermal inertia of the Separator which also affects the screen temperatures. This drawback might nevertheless turn into an advantage when the cryostat needs to be serviced or cleaned. Nevertheless, after optimization the overall helium consumption and the helium hold-time are comparable to the previous design.

In the framework of scientific collaborations, several copies of this system were installed or will be soon installed in several European and United States Universities.

References

- [1] J. H. Ardenkjaer-Larsen, B. Fridlund, A. Gram, G. Hansson, L. Hansson, M. H. Lerche, R. Servin, M. Thaning, and K. Golman. Increase in signal-to-noise ratio of > 10,000 times in liquid-state NMR. *Proceedings of the National Academy of Sciences of the United States of America*, 100(18):10158–10163, 2003.
- [2] A. Comment, B. van den Brandt, K. Uffmann, F. Kurdzesau, S. Jannin, J. A. Konter, P. Hautle, W. T. H. Wenckebach, R. Gruetter, and J. J. van der Klink. Design and performance of a DNP prepolarizer coupled to a rodent MRI scanner. *Concepts in Magnetic Resonance Part B-Magnetic Resonance Engineering*, 31B(4):255–269, 2007.
- [3] S. Jannin, A. Comment, F. Kurdzesau, J. A. Konter, P. Hautle, B. van den Brandt, and J. J. van der Klink. A 140 GHz prepolarizer for dissolution dynamic nuclear polarization. *Journal of Chemical Physics*, 128(24):241102, 2008.
- [4] A. Comment, B. van den Brandt, K. Uffmann, F. Kurdzesau, S. Jannin, J. A. Konter, P. Hautle, W. T. Wenckebach, R. Gruetter, and J. J. van der Klink. Principles of operation of a DNP prepolarizer coupled to a rodent MRI scanner. *Applied Magnetic Resonance*, 34(3-4):313–319, 2008.

3 Solid-state enhancement measurement

Abstract

The enhancement factor ϵ , *i.e.* the ratio between DNP-enhanced and thermal polarization at liquid helium temperatures is an essential parameter to characterize samples used for dissolution DNP. The standard way to determine ϵ is by calculating the ratio between the NMR signal of the DNP-enhanced spins and the thermal equilibrium NMR signal.

It typically takes 5 build-up time constants to reach the maximum polarization plateau and 5 T_1 's to reach thermal equilibrium leading to extremely time consuming measurements in case of long T_1 nuclei as for instance ^{15}N in certain molecules. Furthermore these are single shot measurement.

The method we developed allows for a complete and very accurate (to a precision of about one percent) characterization of the sample NMR/DNP properties, namely build-up time constant, T_1 and ϵ , in as little as 2 build-up time constants plus 3 T_1 's without any a priori knowledge of the coil B_1 . If the T_1 of the sample is known, the method allows to precisely determine the thermally polarized signal in a time shorter than $T_1/2$ instead of the standard 5 T_1 . In this time frame a series of measurements are performed and averaged leading to more robust signal determination with respect to the single shot method.

The technique can be applied to both the thermally polarized and hyperpolarized NMR signal determination.

3.1 Introduction

Determining the polarization enhancement factor ϵ , defined as the ratio between the DNP enhanced polarization and the thermally relaxed polarization, is important to characterize samples for dissolution DNP. Furthermore comparing polarization measured in solid-state and in liquid state after dissolution helps to adopt strategies that minimize losses and improve dissolution procedure.

The standard way to determine the enhancement factor is to measure separately the DNP-enhanced and the thermally relaxed NMR signal, and then calculate their ratio. Although the simple definition, the measurement can be extremely time consuming due to the long time needed to reach the thermally relaxed and DNP-enhanced states for nuclei with long buildup times and T_1 's. Furthermore, since both are single shot measurement, they can suffer from problems related to this method, namely radio-frequency noise instability in the electronics or lack of circuit stability between measurements. Since the same reasoning can be applied both to DNP-enhancement and to the thermal relaxation, in the following we will focus on the thermal relaxation. To apply the technique to the DNP-enhancement it is enough to substitute T_1 with the buildup time, and the thermally relaxed magnetization M_{th} with the DNP-enhanced magnetization M_{DNP} .

The standard way to measure the NMR signal intensity corresponding to thermal polarization of a nuclear spin system, is to wait until the system is fully relaxed to its thermal equilibrium state and perform a single-pulse measurement, typically a $\pi/2$ pulse. To do so it is necessary to have an estimate of the longitudinal relaxation time T_1 . The measured signal S in a single-pulse measurement with flip angle θ is related to the longitudinal magnetization M through:

$$S(t) \propto M(t) \sin(\theta) \quad (3.1)$$

where t is the time at which the pulse is applied. Due to this proportionality, in the following we will study only the longitudinal magnetization evolution. It is important to note that the proportionality is exact only if the circuit remains perfectly stable; variations of the circuit properties over measurements can affect the proportionality, decreasing the measurement accuracy.

Assuming a mono-exponential relaxation behavior we can use the Bloch equation 1.18 to determine the time evolution of the magnetization:

$$M(t) = M_{th} - [M_{th} - M_0] e^{-\frac{t}{T_1}} \quad (3.2)$$

where M_{th} is the thermally relaxed magnetization and M_0 is the initial magnetization at time

$t = 0$.

Starting from a null initial polarization $M_0 = 0$ it takes at least $5 T_1$ to reach a magnetization that is within 1% of the equilibrium polarization signal M_{th} . For most nuclei and in particular 1H and ^{13}C , $T_1 \leq 1 \text{ min}$ in liquid state at common MRI fields. In these conditions it is not an issue to determine the signal from M_{th} through NMR measurements in a reasonably short amount of time, even if a certain amount of averages is required.

However, if we consider solid-state samples at very low temperatures, in the order of $1 K$, as it is the case for DNP and we want to measure the enhancement for nuclei such as ^{15}N , the relaxation times can be in the order of hours, up to tens of hours; this means even more than a full day to achieve a thermally polarized system on which to perform a single-shot NMR experiment.

This is problematic because during the long time before the measurement is performed, the circuit could have been affected by changes related to temperature instability that modify its characteristics. Furthermore, to reliably obtain the relaxed magnetization the system must remain at constant temperature for all the long time waited to achieve the relaxed state.

In the following we will present a method we developed that can dramatically decrease the measurement time, down to a fraction of T_1 or buildup time in case of DNP-enhanced signal determination. This method is based on averaging of measurement thus making the determination more robust with respect to the single-shot acquisition.

The NMR probe was tuned using fixed capacitors placed next to the coil and variable capacitors placed outside of the cryostat, as described in a previous publication¹. Without any *a priori* knowledge of the quality factor of the loaded probe, we determined the exact flip angle θ for a given square pulse at fixed length and power and the relaxation time T_1 from the measurement of the signal decays at different repetition times δ .

From the knowledge of θ and T_1 , we were able to rapidly achieve and measure the steady-state magnetization for different values of δ , taking advantage of the high sensitivity of the NMR probe even for low steady-state polarization values. Finally, the signal corresponding to the thermally relaxed and DNP-enhanced magnetization were calculated and used to determine c very precisely.

3.2 Evenly spaced pulses

Magnetization dynamics

The measurement presented in this chapter were all performed with a sequence, shown in Figure 3.1, composed by single square pulses of flip angle θ followed by the signal acquisition, repeated n times with a repetition time δ . Both θ and δ remain constant within the same experiment.

The dynamics of the nuclear spin magnetization is not a continuous function of time, due

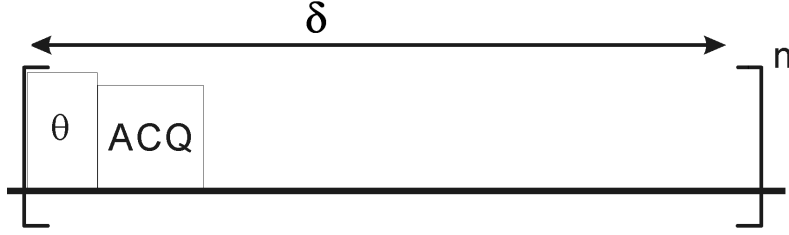


Figure 3.1: Evenly spaced pulses scheme. The signal is acquired after each pulse. δ is the total amount of time between two pulses.

to the effect of the pulses. Nonetheless, as long as θ and δ are kept constant, it is possible to predict the time evolution of the magnetization without any approximation (See Appendix B).

We define $M_0 = M(t=0)$ the magnetization of the system at the time just before the first pulse is applied and M_{th} the thermally polarized magnetization in absence of perturbations.

The signal intensity measured on the j^{th} experiment is proportional to the actual longitudinal magnetization $M_j^{\delta,\theta}$ that can be written as:

$$M_j^{\delta,\theta} = M_\infty^{\delta,\theta} - (M_\infty^{\delta,\theta} - M_0) e^{-\left(\frac{1}{T_1} - \frac{\ln(\cos\theta)}{\delta}\right)j\delta} \quad (3.3)$$

where:

$$M_\infty^{\delta,\theta} = M_{th} \frac{1 - e^{-\frac{\delta}{T_1}}}{1 - e^{-\frac{\delta}{T_1}} \cos\theta} \quad (3.4)$$

is the limit magnetization of the steady state obtained with θ and δ .

The signal obtained by this expression of the magnetization is commonly maximized for a given δ in function of θ on MRI/MRS measurements with a low recycle time^{2,3}. The angle that maximize $S = M_\infty^{\delta,\theta} \sin(\theta)$ for a single measurement, $\theta_E = \cos^{-1} \left[e^{-\frac{\delta}{T_1}} \right]$ is called Ernst angle.

In our approach θ is unknown at the beginning and kept constant. We perform measurements at different δ to determine M_{th} and the goal is to minimize the total measurement time disregarding the magnetization of the optimized steady state.

Although the dynamic defined in equation 3.3 is inherently discontinuous, we find convenient to use continuous time functions in the following discussion. Identifying $j\delta = t$ we obtain:

$$M^{\delta,\theta}(t) = M_{\infty}^{\delta,\theta} - \left(M_{\infty}^{\delta,\theta} - M_0\right) e^{-\left(\frac{1}{T_1} - \frac{\ln(\cos\theta)}{\delta}\right)t} \quad (3.5)$$

We underline that the dynamics obtained in equation 3.5 holds only in the case of measurement performed at constant flip angle θ and constant repetition time δ .

Relaxation time and flip angle

Equation 3.5 allows us to determine the values of θ and T_1 .

We assume to be in conditions where we need to measure the relaxation time T_1 of a sample using an unknown flip angle θ ; equation 3.5 allows for arbitrary θ , but for clarity in the following we will assume the flip angle $0 < \theta < \pi/2$ so that $\ln \cos\theta \in \mathbb{R}$. A separate discussion is needed for the case $\cos\theta \leq 0$ out of the scope of this chapter. In the following we will define $\alpha = \cos\theta$ and $\beta = e^{-\frac{\delta}{T_1}}$.

After a decay measurement, as presented in Section 1.6, we can determine the apparent relaxation time $T'_\theta(\delta)$ by fitting data with a mono-exponential function. From equation 3.5 we obtain that T'_θ is linked to δ as:

$$T'_\theta(\delta) = \frac{1}{\frac{1}{T_1} - \frac{\ln\alpha}{\delta}} \quad (3.6)$$

Equation 3.6 is also known as *RF correction* and is used to obtain the real T_1 , correcting the fitted value T'_θ , from a single measurement at a certain δ with θ already known from previous calibration.

In our case we skip the coil calibration and we directly measure the apparent relaxation time T'_θ for different values of δ . Then, using equation 3.6, we can extract the relaxation time T_1 of the sample and the flip angle θ used.

Figure 3.2-left shows the theoretical behavior of the apparent relaxation time T'_θ in function of δ for different flip angles θ . Notice that $T'_\theta < T_1$ always and it decreases linearly for $\delta \ll T_1 \ln \alpha$. Only two measurement performed on the $\delta > T_1 \ln \alpha$ and on the $\delta < T_1 \ln \alpha$ regions respectively are enough to obtain a good determination of T_1 and θ up to a 1 – 2 % precision. Repeating the measurement over a larger δ interval further improves the determination.

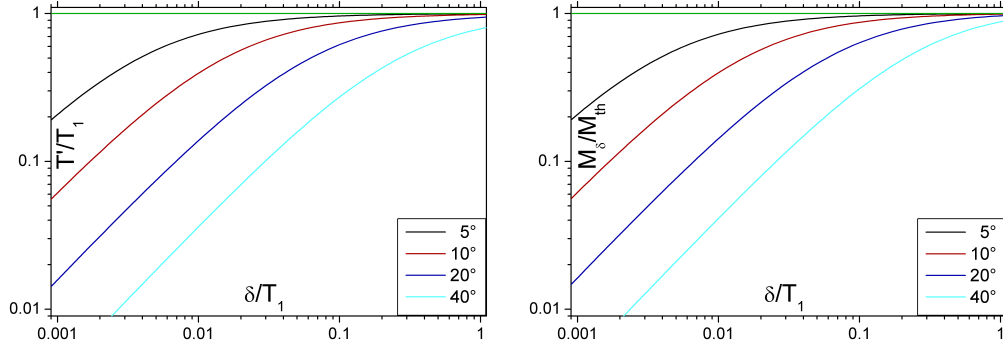


Figure 3.2: T' (left) and $M_\infty^{\delta, \theta}$ (right) in function of δ and in units of T_1 and M_{th} for different flip angles θ .

Thermal signal determination

From here on we assume T_1 and θ known from previous experiments.

We can determine the thermal equilibrium magnetization M_{th} precisely, measuring the steady state magnetization $M_\infty^{\delta, \theta}$.

Inverting equation 3.4 we obtain:

$$M_{th} = M_\infty^{\delta, \theta} \frac{1 - \beta\alpha}{1 - \beta} \quad (3.7)$$

From Figure 3.2-right we can see the behavior of the steady state magnetization $M_\infty^{\delta, \theta}$ in function of δ . $M_\infty^{\delta, \theta} < M_{th}$ always. Using equation 3.7, a single measurement of the steady state magnetization signal for an arbitrary δ is enough to determine the signal of the thermal magnetization.

At this stage it is not evident how to speed up the determination, with respect to the standard scheme. Using a large δ will lead us back to the long waiting times to reach the steady state, comparable to the one of the standard scheme while using a δ too low requires a very small time for the system to reach the steady state but with the drawback of a very long time needed in averaging due to the low signal intensity.

Exploiting again the knowledge of the magnetization dynamics from equation 3.3 we can decrease the time needed to reach the steady state. Instead of starting the sequence at $t = 0$ and then discard all the measurements performed in the first $5 T'$ needed to approach the steady state, we can start at $t = 0$ with a saturated longitudinal magnetization $M_0 = 0$ and

wait before the first pulse a certain time T^* satisfying the following condition:

$$\begin{aligned} M_{\infty}^{\delta, \theta} &= M_{th} \cdot (1 - e^{-\frac{T^*}{T_1}}) \\ T^* &= -\ln\left(\beta \frac{1-\alpha}{1-\alpha\beta}\right) T_1 \end{aligned} \quad (3.8)$$

The time T^* needed to reach the steady state magnetization, for common values of the measurement parameters, is close to T' , and after the acquisition begins no measurement is discarded.

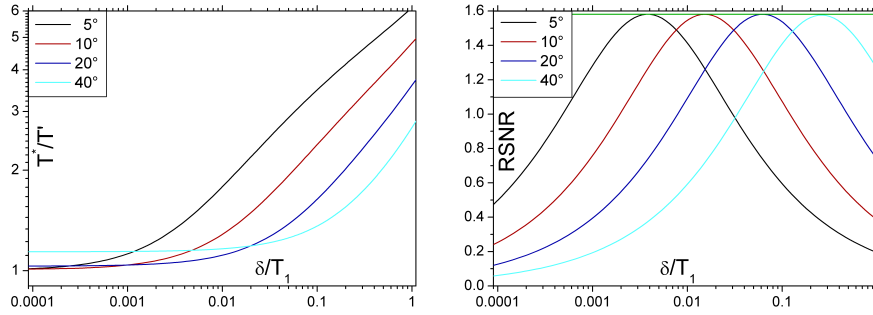


Figure 3.3: T^* in units of T' (left) and $RSNR$ achievable in $\tau = 5 T_1$ (right) vs δ in units of T_1 for different flip angles.

From Figure 3.3-left we can see that $T^* < 5 T'$ in a wide range of experimental conditions, decreasing the amount of time needed for every measurement. Note that this time is wasted, since no measurement is performed.

At this point we still have a free parameter, δ , to be chosen. We can give a criterion to choose the best δ to achieve the maximum measurement efficiency, in terms of Signal to Noise Ratio (SNR) at the end of the measurement.

We assume arbitrarily $SNR = 1$ for a hypothetical reference NMR signal measured with a $\pi/2$ pulse on a thermally relaxed system with M_{th} magnetization. We define the Relative SNR (RSNR) as the ratio between the SNR of an averaged measurement taking time τ performed with our method, and the SNR of the reference signal. In other words the RSNR is the amount of information we can extract with our measurement scheme with defined δ and θ in a time τ compared to the thermal signal determined with the standard scheme on a single measurement.

Although the following equations are valid for arbitrary τ , to perform a meaningful comparison in the examples we will consider the $RSNR$ achievable in $\tau = 5 T_1$.

If we perform a measurement every δ time interval during a period of time τ we can do:

$$n = \left\lfloor \frac{\tau}{\delta} \right\rfloor \sim \frac{\tau}{\delta} \quad (3.9)$$

acquisitions, where the approximation on the right hand term holds if we consider $\delta \ll \tau$. The signal measured on each acquisition is only a fraction of the maximum signal achievable with a $\pi/2$ pulse on M_{th} :

$$S_{\delta,\theta} = S_{th} \frac{1-\beta}{1-\alpha\beta} \sin\theta \quad (3.10)$$

Combining equations 3.9 and 3.10, and assuming Gaussian noise propagation, we can calculate the RSNR obtained from a measurement during an acquisition period τ :

$$RSNR_{\delta,\theta} = \frac{S_{\delta,\theta}}{S_{th}} \sqrt{n} = \frac{1-\beta}{1-\alpha\beta} \sin\theta \sqrt{\frac{\tau}{\delta}} \quad (3.11)$$

Figure 3.3-right shows the behavior of $RSNR_{\delta,\theta}$ for $\tau = 5 T_1$ in function of δ for different θ . It can be noted that this measurement scheme, at the optimal value of δ for a certain θ allows to obtain higher SNR than the classical scheme, in the same amount of time.

Summarizing, the advantages of this method are on one side the fact that in the same amount of time as the classical scheme it can increase the measurement SNR by about 60%; on the other hand if, as it often happens in solid-state NMR, the SNR of the reference signal is known to be very high, the measurement can be stopped at $n^* \ll n$, dramatically decreasing the measurement time.

3.3 Results

Optimized strategy examples

As an example, let's assume that we already know $\theta = 10^\circ$ and T_1 , and we want to determine the thermally polarized signal with different RSNR. We have to take into account in the total measurement time t_{TOT} , both the T^* time at the beginning of the acquisition and the effective measurement time $\tau = \delta n^*$.

From Table 3.1 we can see that even to achieve the same SNR as the standard technique, the time needed with our method is about half of a single standard measurement. This time then decreases in a parabolic fashion, as the desired RSNR decreases.

$RSNR$	0.1	0.25	0.5	1
$\delta [T_1]$	0.0011	0.0029	0.006	0.01
$T^* [T_1]$	0.07	0.17	0.33	0.5
$M_{\infty}^{\delta, \theta} [M_{th}]$	0.067	0.16	0.28	0.40
n	73	81	103	209
$T_{meas} [T_1]$	0.08	0.24	0.62	2.1
$t_{TOT} [T_1]$	0.15	0.41	0.95	2.6

Table 3.1: Operational parameters for different values of target RSNR.

Since our goal consists in minimizing the measurement time, it is worth to say some words about the flip angle. The explicit dependency of the minimum t_{TOT} on θ for a given $RSNR$ is non trivial but for low enough flip angle $\theta < 30^\circ$, it remains $t_{TOT} < 2.7 T_1$ for $RSNR = 1$ while it increases very fast when $\theta \sim 90^\circ$ (see Appendix B).

Example of measurements

In this section we show an example measurement performed on a sample of ^{129}Xe , polarized at 5 T and 1.07 K.

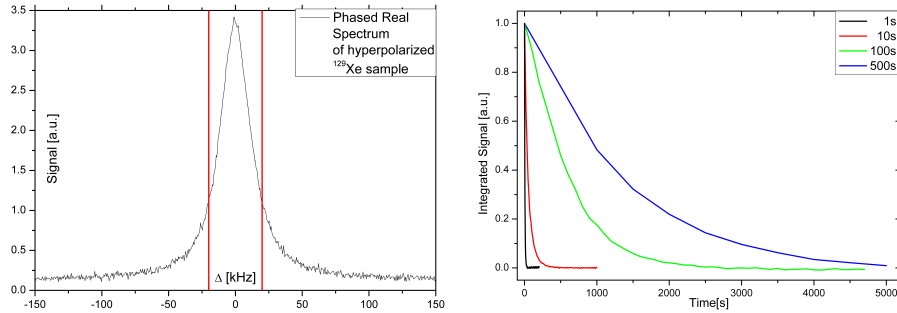


Figure 3.4: Example of a spectrum obtained from a measurement on a DNP-enhanced ^{129}Xe sample (left) centered at 58.797 MHz with integration window for signal intensity determination marked in red and several decays at different δ (right).

In figure 3.4-left an example of a spectrum obtained from a measurement on a DNP-enhanced ^{129}Xe sample is shown. The signal intensity is determined integrating the peak in the region where it is above $\approx \frac{1}{3}$ of the maximum, in this case $\Delta \in [-20\text{ kHz}; 20\text{ kHz}]$ (red lines) about the resonance frequency of 58.797 MHz .

The signal decays for different δ , shown in Figure 3.4-right, were fitted with a single exponential function to extract $T'(\delta)$.

In Figure 3.5-left the fitting of T' with equation 3.6 is shown. This allowed us to determine $\theta = 34^\circ \pm 0.5^\circ$ and $T_1 = 3450 \pm 50\text{ s}$ with high precision.

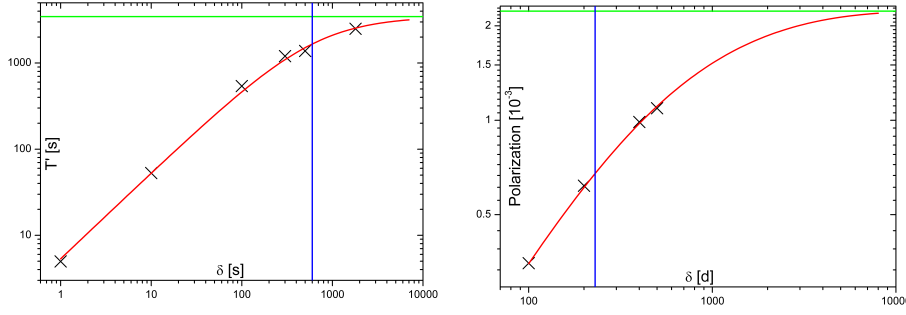


Figure 3.5: Right: $T'(\delta)$ fitted to determine T_1 and θ in a wide range of δ . blue line represents $\delta = T_1 \ln \cos \theta$. Left: $M_{\infty}^{\delta, \theta}$ fitted to determine M_{th} showed in green; blue line represent the optimal δ for a $RSNR = 0.5$.

We measured $M_{\infty}^{\delta, \theta}$ with the strategy described above and showed the results in Figure 3.5-left. We chose different δ about the optimal value of 230 s for a $RSNR = 0.5$, and then fitted to determine M_{th} . The chart is already rescaled accounting for the thermal polarization of ^{129}Xe at 5 T and 1.07 K to be $P = 2.495 \cdot 10^{-3}$.

Finally we only need to know the signal intensity from a DNP-enhanced experiment, eventually determined with the same technique, to directly determine the enhancement.

Application

We measured several different nuclei in different conditions to asses the feasibility of the technique.

Nucleus	Sample	Radical	T [K]	θ [°]	T_1 [s]	T_b [s]	ϵ_-
^{129}Xe	1:2 Xe:Isobutanol	33mM	1.07	34	3450	614	43 ± 2
^{13}C	3M 1-Acetate in 2:1 D_2O :d6-etOD	50mM	1.07	2	3620	1030	140 ± 5
			4.20	8	130	48	87 ± 3

Table 3.2: Results of measurements on different nuclei in different conditions. Thermal and negatively DNP-enhanced signals were measured with the same method extracting the longitudinal relaxation time T_1 and the buildup time constant T_b . DNP-enhanced $M_{\infty}^{\delta, \theta}$ were obtained directly from the T' measurements. The radical used was TEMPOL.

The results are summarized in table 3.2. In all the cases it was possible to apply the technique both to thermal and DNP-enhanced signals, obtaining reproducible measurements with an error as low as 1 – 2 %.

3.4 Conclusions and Outlook

In this chapter we showed how to quickly obtain and then exploit the steady state magnetization, produced by trains of evenly spaced constant flip angle pulses, to determine the thermal polarization signal intensity. We showed as well, in the case the resonant circuit is not calibrated or the T_1 of the sample is unknown, a quick method to perform the flip angle and relaxation time determination at once.

The model was applied to various nuclei in various conditions and samples, always observing a mono exponential decaying of the signal measured. This suggest that the interaction between magnetization baths of different nuclei is negligible in the timescale of our measurement for the samples in exam.

Due to his potentially very low time needed to determine the thermal signal, this method can be routinely used to determine the solid-state enhancement obtained in the prepolarizer. This can be done before a dissolution for experiments where the signal intensity is important, to probe for example the sample quality or, coupled to an *a posteriori* measurement in the MRI scanner, the amount of polarization lost during the sample transfer.

References

- [1] A. Comment, B. van den Brandt, K. Uffmann, F. Kurdzesau, S. Jannin, J. A. Konter, P. Hautle, W. T. Wenckebach, R. Gruetter, and J. J. van der Klink. Principles of operation of a DNP prepolarizer coupled to a rodent MRI scanner. *Applied Magnetic Resonance*, 34(3-4):313–319, 2008.
- [2] R.R. Ernst and W.A. Anderson. Application of fourier transform spectroscopy to magnetic resonance. *The Review of Scientific Instruments*, 37(1):93–102, 1966.
- [3] J. Cavanagh, W.J. Fairbrother, A.G. Palmer III, M. Rance, and N.J. Skelton. *Protein NMR Spectroscopy. Principles and Practice*. Elsevier Academic Press, 2010.

4 Hyperpolarized ${}^6\text{Li}$ as blood oxygenation probe

Abstract

Hyperpolarization by dissolution DNP allows enhancing the polarization of selected nuclear spins, in particular ${}^{13}\text{C}$ in biomolecules, and to perform MR experiments with an unprecedented sensitivity. The main drawback of the technique is that the large polarization will ineluctably relax towards its thermal equilibrium and typical ${}^{13}\text{C}$ T_1 's are shorter than a minute. It was recently shown that ${}^6\text{Li}$ can be hyperpolarized in aqueous solution of ${}^6\text{LiCl}$ and that, thanks to its long T_1 , hyperpolarized ${}^6\text{Li}$ can be a sensitive probe to detect nanomolar concentration of the *Gd* contrast agent. The aim of the present chapter was to determine the effect of oxygenation in human and rat, blood and plasma, on ${}^6\text{Li}$ relaxation. The results show the relaxivity enhancement effect of hemoglobin on its de-oxygenated form with respect to its oxygenated form. This behavior produces a difference in ${}^6\text{Li}$ T_1 's between oxygenated and de-oxygenated blood that will be useful to detect hemoglobin oxygenation level in cells and possibly *in vivo* and could potentially be used to detect diseased tissue with abnormal oxygenation, such as cancerous regions.

4.1 ^6Li properties and medical applications

Although ^6Li has a spin $I = 1$, the amplitude of its electric quadrupolar moment is so small ($Q < 8.5 \text{ kHz}$)¹ that the relaxation associated with the quadrupolar interactions is usually negligible compared to other relaxation mechanisms such as intermolecular dipolar relaxation induced by paramagnetic species in aqueous solutions. The ^6Li longitudinal relaxation time of Li^+ ions in aqueous solutions is in fact unusually long and values up to $T_1 = 1040 \text{ s}$ in de-oxygenated D_2O have been reported². It was proposed that this property could be taken advantage of to detect minute amount ($< \text{mM}$) of Gd -based MR contrast agents since small variations in relative relaxation can be readily detected³. This can be done *in vivo* thanks to the dissolution DNP technique developed to hyperpolarized long- T_1 nuclear spins⁴. Hyperpolarized ^6Li has a great potential for molecular imaging since Li^+ ions diffuse freely across cell membranes. A recent study in rodents showed that a large fraction of lithium in the brain is located in the intracellular compartment⁵. Hyperpolarized ^6Li could thus be an interesting contrast media for perfusion imaging with similar methods than the ones proposed with hyperpolarized xenon⁶, and hyperpolarized ^{13}C tert-butanol⁷.

The primary use of lithium salts in a medical context is to treat maniac-depressive (bipolar) and depressive disorders^{8,9}. It has been administrated at doses up to 1200 mg/day , which led to serum concentration between $0.3 - 1 \text{ mM}$ ¹⁰, a concentration which is on the same order as the ones obtained after infusion of hyperpolarized $[1 - ^{13}\text{C}]$ -pyruvate in the first clinical study¹¹. The only other lithium isotope, ^7Li , has a natural abundance of 93% and a short T_1 , on the order of 6 s in human blood¹². It is thus been used as a NMR probe to determine the distribution of lithium in patients brain after administration of lithium treatment¹⁰. ^7Li NMR was also used to probe Na^+ ion channel activity in isolated rat hearts¹³.

One common method used in MRI to probe blood oxygenation levels, relies on the relaxivity effects of hemoglobin and oxyhemoglobin¹⁴ on the transversal relaxation time T_2 of water protons. This method is called Blood-Oxygen-Level Dependent contrast imaging (BOLD contrast imaging)¹⁵ and is extensively used in functional MRI (fMRI) to determine the difference of activity on brain regions in response to an external stimulus¹⁶.

We herein tested the potential of hyperpolarized ^6Li to detect blood oxygenation level, and specifically the relaxivity effects on ^6Li of hemoglobin in its oxygenated and de-oxygenated form, in human and rat blood. Rather than detecting the influence of blood oxygenation on the chemical shift of ^{129}Xe as was previously proposed¹⁷, we propose to measure the effect on the long longitudinal relaxation time of hyperpolarized ^6Li .

4.2 Methods

$450 \mu\text{l}$ of glassy frozen $15 \text{ M } ^6\text{LiCl}$ (2:1 $\text{D}_2\text{O}/\text{d}_6$ -ethanol with 40 mM TEMPO) solution was polarized at 7 T and $1 \pm 0.05 \text{ K}$ using already presented hardware and methods^{4,18}. Following a procedure described in a previous publication¹⁹ six frozen beads of 1 M Sodium Ascorbate in D_2O were inserted into the sample cup to quench the radical in order to obtain

the longest possible T_1 . The samples were subsequently rapidly dissolved in 5 ml of super-heated D_2O . The hyperpolarized solution was extracted from the polarizer using high-pressure helium gas at 6 bar in about 3.5 s and collected in a vial.

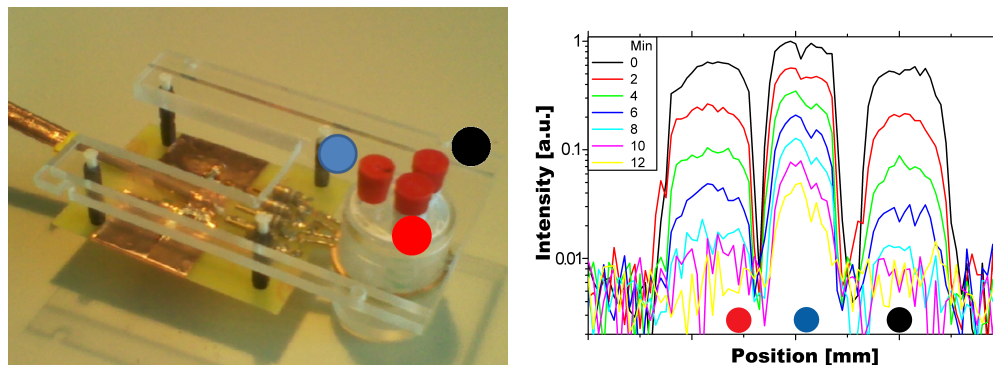


Figure 4.1: Left: arrangement of coils and tubes for the measurement. Red and black circles represent tubes filled with oxygenated and de-oxygenated blood/plasma; the blue tube contains the D_2O reference. Right: example of a series of projections acquired during a single experiment on a blood sample. Each peak correspond to the signal coming from a tube in the sample holder (left) according to the colored circles.

To perform simultaneous NMR acquisition on both oxygenated and de-oxygenated samples we developed a Plexiglas phantom, shown in of figure 4.1-left, composed of a circular 38 mm \varnothing container capable of allocate three standard NMR tubes. This container is surrounded by two circular coils with resonance frequency set at 1H and 6Li frequency at 9.4 T. The 1H coil is essentially used for shimming purposes, while the 6Li coil is used for acquisition during the DNP experiment.

Prior to each hyperpolarized MR experiment, three 10 mm NMR tubes were prepared and placed in the phantom of figure 4.1-left: one tube was filled with D_2O (blue), the second and third ones with 2 mL of oxygenated (red) and de-oxygenated (black) human blood added with 3 UI/mL of heparin, respectively. The de-oxygenation procedure consisted in blowing Argon gas at the top surface of blood into the NMR tube for 10 min. Then the phantom was placed into a 9.4 T horizontal wide bore Varian rodent scanner and 300 μL of hyperpolarized 6Li solution was injected manually into each tube.

The geometrical arrangement of the tubes was designed so that they do not overlap if linearly projected along a certain direction. Thanks to this arrangement, using a 6Li 1D gradient echo image sequence, we obtained signals coming from each tube in different positions of the image respectively, being able to associate to each tube the signal coming from each region of the spectrum as shown in figure 4.1-right. The images were recorded once every 20 s using a 10° flip angle, 55 μs hard pulse. We used the minimum linear gradient intensity to separate signal coming from different tubes. In this condition we obtained the maximum possible SNR. The samples were kept at room temperature.

The sample holder used for the measurement together with the gradient echo imaging,

allowed the synchronous measurement of T_1 in oxygenated and de-oxygenated samples together with the presence of a reference measurement in D_2O . This fact is very important in order to perform comparisons due to the non negligible variability of T_1 between different measurements. This procedure overcomes the variability and allows us to perform robust determinations and comparisons of the relaxation time differences between oxygenated and de-oxygenated samples. The measured projections were integrated along the three images and the time evolution of the signals integral determined. We fitted the data with simple mono-exponential decay functions to determine T' and then we corrected the results for the RF perturbation according to equation 3.6 to determine the exact T_1 . An identical procedure was used to measure T_1 in oxygenated and de-oxygenated human plasma. We repeated the whole procedure also in rat blood and plasma to highlight eventual differences between human and rat blood.

Quenching and reproducibility

^6Li T_1 being extremely long, it is very sensitive to impurities and variations due to different efficiencies of the quenching procedure. The radical used for hyperpolarization as well as the presence of protons coming from the ascorbate itself used to quench the radical, contribute to the relaxation process. We performed some bench relaxivity measurement experiments on $^6\text{LiCl}$ solutions to determine the entity of the variations in some controlled conditions.

Solution	^6Li T_1 [s]
Pure D_2O	506.0 ± 10
20 mM Deuterated Sodium Ascorbate	400.7 ± 5
20 mM Sodium Ascorbate	394.2 ± 5

Table 4.1: Longitudinal relaxation time T_1 of ^6Li in pure D_2O with and without adding normal and deuterated Sodium Ascorbate.

We measured the ^6Li T_1 in a 500 mM solution of $^6\text{LiCl}$ in pure D_2O (99.96% D) on a 400 MHz 9.4 T vertical high resolution Bruker NMR scanner. Then we compared the effect of adding Sodium Ascorbate and Deuterated Sodium Ascorbate to the pure D_2O solution. The results are summarized on table 4.1. The ^6Li T_1 in pure non de-oxygenated D_2O was about one half of that reported in literature for de-oxygenated D_2O ². Furthermore, adding 20 mM of Sodium Ascorbate, either in its protonated or deuterated form, further decreases the T_1 of about 20 %. The measurements show the high sensitivity of T_1 even to the presence of a small amount of protons coming from the ascorbate.

As can be seen from figure 4.2 even the T_1 values on the reference sample in different experiments can show variability. We used these values as a first quality check for the dissolution quality: if T_1 is too low the experiment is discarded and repeated. This high sensitivity led to a non negligible variability of T_1 between experiments, especially in blood. This elucidate

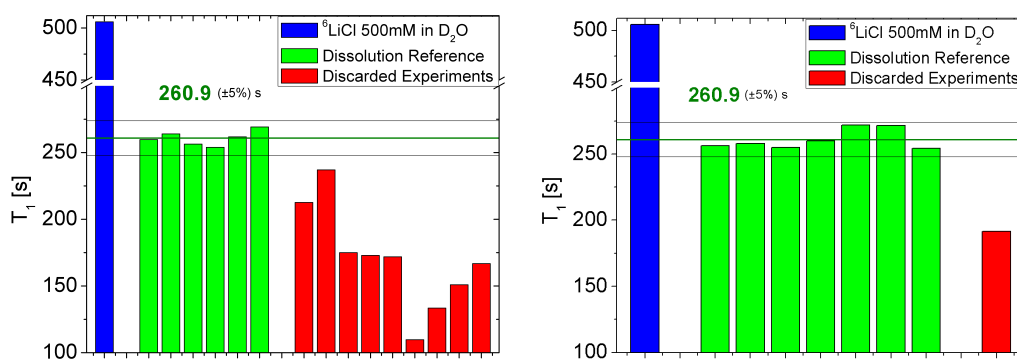


Figure 4.2: Results of T_1 measurements on the reference samples. The results obtained during human (left) and (rat) experiments are shown together with the reference measurement on pure ${}^6\text{LiCl}$ in D_2O (see table 4.1). The red experiments were discarded.

the importance of a synchronous measurement of oxygenated/de-oxygenated samples in the same conditions in order to be able to perform a meaningful comparison. In our experiment each measurement is performed on two tubes of the same blood sample at the same time and temperature, where the only difference between samples comes from the de-oxygenation procedure performed with Argon gas.

4.3 Results

In figure 4.2, the results of hyperpolarized ${}^6\text{Li}$ T_1 measurements on the D_2O reference for the two sessions of experiments performed in human and rat blood and plasma, are presented. The measurement showed that, although many experiments had a very good reproducibility (green), in about half of the total experiments performed T_1 's were sensibly lower (red). This fact can be ascribed to the not perfect quenching of the radical during the fast dissolution procedure. We used the following criterion to accept an experiment: its reference T_1 had to lie within a $\pm 5\%$ band drawn in the chart around the average 261 s of the experiments with longest T_1 . Obtaining a value outside this range let the measurement be discarded.

Absolute measurements

We observed a quite high variability in the absolute value of ${}^6\text{Li}$ T_1 measured in figure 4.3, for both human and rat blood, especially in full blood samples. As we showed in the precedent paragraph, the relaxation of ${}^6\text{Li}$ is very sensitive to impurities. This led to the observation that into a biological environment it is not possible to assign a definite value to T_1 . The variability is lower in plasma probably because of its higher homogeneity with respect to full blood.

On average, the measured T_1 's on full blood lie in the same range for both human and rat samples. About plasma, we observed a lower average T_1 on rat samples with respect to human ones, of about 10%. This difference can be mainly ascribed to the precision of the T_1

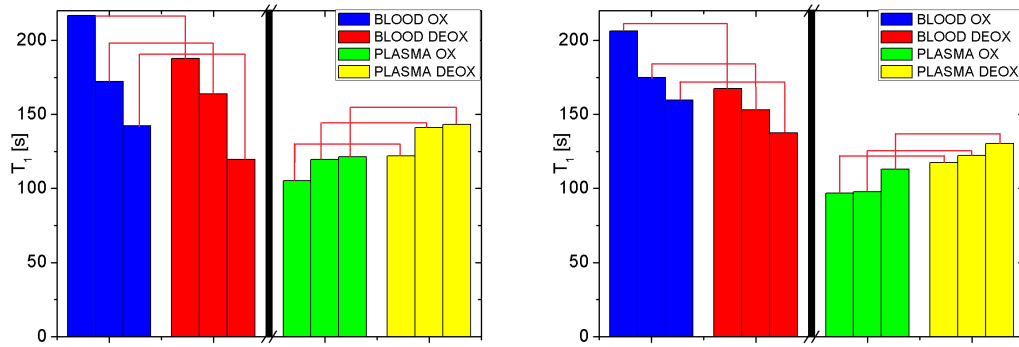


Figure 4.3: Results of T_1 measurements on blood and plasma, human (left) and rat (right) plasma samples. Magenta lines link couples of oxygenated/de-oxygenated measurements on the same experiment. Both charts have the same vertical scale.

determination that in our case is $\pm 5\%$. With this error level the difference between average T_1 's between human and rat plasma is below the significance threshold.

Relative difference

Although this quite high variability in the measurements, our protocol of simultaneous acquisitions allowed us to consistently and repeatably determine a difference between oxygenated and de-oxygenated samples.

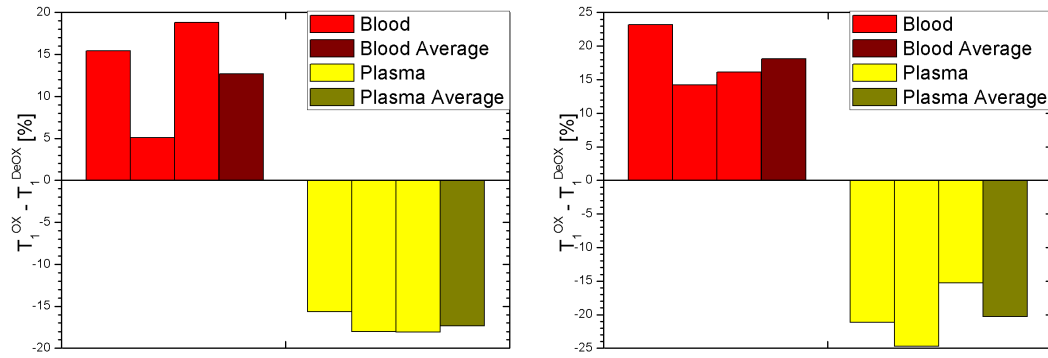


Figure 4.4: Relative difference, in percent, between T_1 's of oxygenated and de-oxygenated samples measured in the same experiment for human (left) and rat (right).

The T_1 's differences between oxygenated and de-oxygenated samples, shown in figure 4.4, have opposite sign for blood with respect to plasma. Blood samples show a longer T_1 for oxygenated samples of about 15 – 20%. If we discard the extreme measurements (second for human blood and first for rat blood) we obtain compatible results. Plasma samples show an opposite behavior with longer T_1 's on de-oxygenated samples. The average observed ratios between rat and plasma samples are very close and the slight difference in average T_1 's can be explained with the experimental errors as previously discussed.

Discussion

The opposite T_1 difference between blood and plasma samples can be explained taking into account the presence and the effects of hemoglobin. In case of plasma, hemoglobin is not present and the main source of relaxation is linked to the presence of dissolved molecular oxygen, that act as a paramagnetic source of relaxation. In the oxygenated samples the presence of dissolved O_2 enhances the relaxation thus decreasing the T_1 of about 18 – 20% as we determined.

In full blood the molecular oxygen is bound to hemoglobin forming oxyhemoglobin. It has been shown¹⁴ that hemoglobin in oxygenated form has no unpaired electrons thus being diamagnetic. Furthermore, also bound oxygen loses his paramagnetic nature. Finally, the oxygen-hemoglobin complex is diamagnetic, with much limited relaxation effects with respect to paramagnetic hemoglobin. In de-oxygenated blood, the presence of paramagnetic hemoglobin with four unpaired electrons enhances the relaxation of 6Li thus decreasing its T_1 of about 15 – 20% as we saw in figure 4.4.

The slight mismatch between absolute T_1 values and relative differences, between human and rat samples have shown to be non significant thus allowing to conclude that human and rat blood has, with respect to relaxivity properties linked to oxygenation, the same effects on 6Li .

4.4 Conclusions and Outlook

Oxyhemoglobin being diamagnetic and hemoglobin paramagnetic, the observed differences in T_1 of blood samples were attributed to the oxygenation level of hemoglobin. In plasma samples, dissolved oxygen acts as a paramagnetic relaxing agent leading to a decreased T_1 . We showed that hyperpolarized 6Li can be used as an oxygenation probe in human and rat blood, 6Li relaxation being significantly faster in presence of hemoglobin.

The observed difference in T_1 between oxygenated and de-oxygenated blood could be used to detect hemoglobin oxygenation level in cells and possibly *in vivo*. It should be possible to take advantage of the high sensitivity of hyperpolarized 6Li to obtain images with a relaxation-based contrast modulated by tissue oxygenation. This could be useful for localizing *in vivo* areas that are poorly oxygenated, in particular injured brain or cancerous tissue containing hypoxic regions. The response to treatment of these regions could then be probed to assess therapy efficacy.

- [16] S. Ogawa, D.W. Tank, R. Menon, J.M. Ellermann, S.G. Kim, H. Merkle, and K. Ugurbil. Intrinsic signal changes accompanying sensory stimulation: functional brain mapping with magnetic resonance imaging. *Proceedings of the National A*, 89(13):5951½5955, 1992.
- [17] Jan Wolber, Andrea Cherubini, Martin O. Leach, and Angelo Bifone. Hyperpolarized ^{129}Xe NMR as a probe for blood oxygenation. *Magnetic Resonance in Medicine*, 43(4):491–496, 2000.
- [18] F. Kurdzesau, B. van den Brandt, A. Comment, P. Hautle, S. Jannin, J. J. van der Klink, and J. A. Konter. Dynamic nuclear polarization of small labelled molecules in frozen water-alcohol solutions. *Journal of Physics D - Applied Physics*, 41(15):155506, 2008.
- [19] P. Mii½eville, P. Ahuja, R. Sarkar, S. Jannin, P. R. Vasos, S. Gerber-Lemaire, M. Mishkovsky, A. Comment, R. Gruetter, O. Ouari, P. Tordo, and G. Bodenhausen. Scavenging free radicals to preserve enhancement and extend relaxation times in NMR using dynamic nuclear polarization. *Angewandte Chemie-International Edition*, 49(43):7834–7834, 2010.

5 ^{15}N labeled choline cross polarization

Abstract

Choline is a precursor for phospholipid metabolism. It has been studied in NMR for a long time as a biomarker for tumor metabolism. ^{15}N labeled choline shows a very long T_1 and can be used to probe rate of transport or metabolism in brain or study the metabolic changes in tumors. Despite its long T_1 , the ^{15}N spectral dispersion of choline metabolites is very poor. On the other hand the spectral dispersion is much higher for ^1H . Being able to partially and repeatedly transfer the ^{15}N hyperpolarization to ^1H before detection on ^1H would exploit both the long ^{15}N T_1 and ^1H spectral resolution.

We show a method to use Hartmann-Hahn polarization transfer, to partially transfer the hyperpolarization of ^{15}N to surrounding ^1H before detection on ^1H . This method can then be applied to *in vitro* DNP experiments.

5.1 ^{15}N Choline

Recent MR studies^{1;2} have demonstrated that choline is a sensitive biomarker to probe cellular phospholipid metabolism. This metabolism has been proven to be modified in tumors with respect to healthy tissues³. Choline metabolism plays an important role in different pathologies (*e.g.* in liver⁴ or brain⁵).

In Figure 5.1, the structure of choline is shown. Choline does not have long T_1 non protonated carbons (black) that can be effectively used in the dissolution DNP technique. It has been proposed to use deuterated ^{13}C -choline to increase the carbon T_1 's up to 5 times and it was shown that choline metabolites can be observed on ^{13}C spectra after hyperpolarization^{6;7}. On the other hand choline has a quaternary nitrogen (blue) surrounded by non-magnetic nuclei (natural abundance carbon is almost completely ^{12}C with spin $I = 0$). The nitrogen site labeled with ^{15}N shows a very long liquid-state T_1 on the order of minutes⁸. It was shown that fully deuterated choline hyperpolarized ^{15}N signal can be observed for up to an hour⁹.

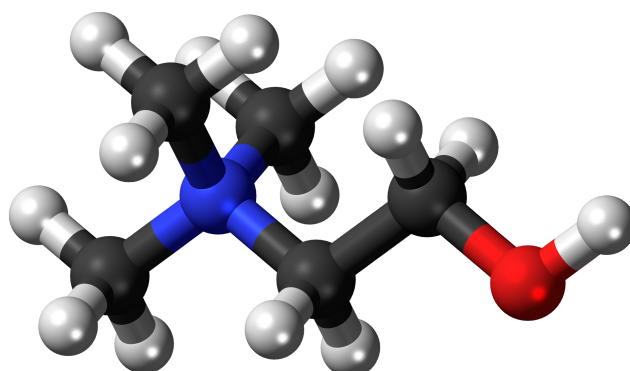


Figure 5.1: Choline structure. Figure adapted from www.wikipedia.com.

The NMR sensitivity of ^{15}N is very low since its gyromagnetic ratio is about ten times lower than protons. In addition, the separation between choline and its metabolites on the ^{15}N spectra is small, making it difficult to study metabolic processes using hyperpolarized ^{15}N -choline as substrate, especially *in vivo* or in cells. It has been shown that transferring the nitrogen polarization to protons prior to proton spectra acquisition greatly enhances the sensitivity and the separation of metabolites¹⁰. However the INEPT sequence used in earlier studies is only applicable for full polarization transfer and it is not possible to have multiple measurements to follow the evolution of the metabolic process. An indirect strategy to overcome this problem while still using INEPT has been proposed. It consists in a synchronous measurement with spatially selective INEPT sequence on a sample¹¹. The sequential readings are performed only on a small part of a homogeneous sample each time. Another cross-polarization scheme was recently proposed to enhance proton polarization from insensitive nuclei with a partial INEPT transfer, called HINDER. HINDER is able to enhance the proton signal while partially retaining the nuclear polarization of the long T_1 hyperpolarized nuclei¹².

In the context of hyperpolarization, there are two main limitations in the use HINDER transfer scheme. First would be that the time for the transfer are related to the scalar couplings which will be different for the substrate and its metabolites. The second issue comes if the J-coupling is weak and the proton T_2 is short since most of the signal will have decayed before acquisition starts. This will most likely be the case with polarization transfer from ^{15}N to ^1H in hyperpolarized choline.

We herein introduce a method to obtain time evolution of ^{15}N -choline metabolism via indirect proton detection, based on a repeated partial transfer of polarization from hyperpolarized ^{15}N to surrounding protons using a partial Hartmann–Hahn polarization transfer¹³. This partial transfer is done from ^{15}N to ^1H and then ^{15}N polarization is flipped back to z axis to be stored for the next measurement. The detection is then performed on protons due to their high spectral dispersion that eases the metabolite observation.

5.2 Efficiency of cross polarization

Although the final aim of the study is the polarization transfer from ^{15}N to ^1H , we studied *in vitro* the reverse transfer to test the cross polarization efficiency. That is because the thermal polarization of ^{15}N is already $\frac{\gamma_{^{15}\text{N}}}{\gamma_{^1\text{H}}} \sim \frac{1}{10}$ of the ^1H thermal polarization and in the Hartmann–Hahn scheme it is shared between at least the 11 protons bound to the 4 carbons surrounding the ^{15}N site. Starting from null proton polarization the maximum theoretical final polarization on each proton after Hartmann–Hahn transfer is less than 1% of ^1H thermal polarization. The difficulties in destroying the ^1H polarization at better than 1%, summed to the short proton relaxation time, led to unreliable measurements on the direct transfer. ^{15}N to ^1H polarization transfer will be tested in *in vitro* dissolution DNP experiments.

In our case, to test the cross polarization efficiency we performed experiments on a 0.5 M ^{15}N -choline in D_2O . The objective of the tests were to assess the efficiency of Hartmann–Hahn cross polarization versus normal refocused INEPT¹⁰ from ^1H (especially the ones at $J3$) to ^{15}N .

The scheme used to test the efficiency of the transfer, shown in figure 5.2-A and B, is the following: a saturation continuous wave (CW) was sent in the nitrogen channel to saturate the ^{15}N polarization. Then the Hartmann–Hahn sequence was performed. It consisted in a $\pi/2$ pulse, used to flip the ^1H magnetization into the xy plane, followed by the spin lock irradiation at optimal Hartmann–Hahn condition for a variable contact time τ . At the end of the contact time, nitrogen (figure 5.2-A) or proton (figure 5.2-B) signals were measured respectively in different experiments. These measurements allowed to determine the ^{15}N enhancement and the residual ^1H polarization in function of the contact time τ .

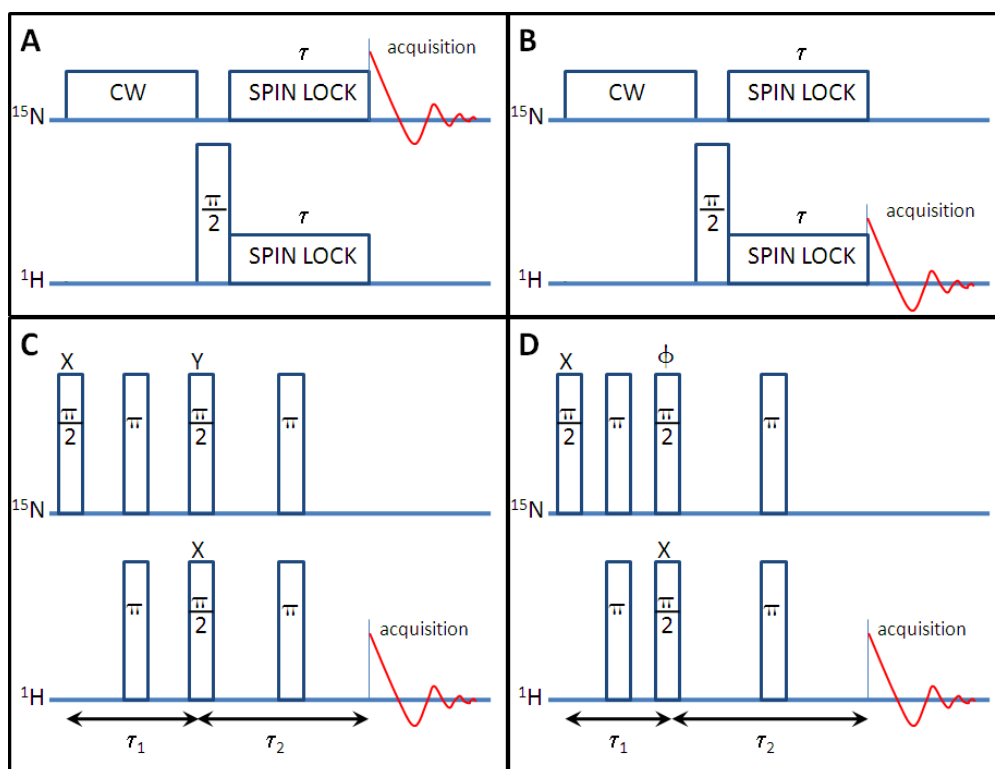


Figure 5.2: Polarization transfer sequences. A) ^1H to ^{15}N partial Hartmann-Hahn transfer sequence used to measure the ^{15}N enhancement for variable contact time τ . B) ^1H to ^{15}N partial Hartmann-Hahn transfer sequence used to measure the residual ^1H polarization after the transfer. C) standard ^{15}N to ^1H refocused INEPT sequence. D) ^{15}N to ^1H HINDER sequence.

5.3 Methods and Results

We prepared a $0.5\text{ M }^{15}\text{N}$ -choline in pure D_2O (99.8% atoms D). $500\text{ }\mu\text{l}$ of solution was inserted in a 5 mm outer diameter NMR tube. The measurements were performed on a 300 MHz Bruker INOVA spectrometer using a BBI probe (one ^1H channel and one broadband channel) at constant temperature of 25°C . Power levels used for hard pulses were -5 dB on the ^{15}N channel and -7 dB on the ^1H channel. At these power levels the pulse lengths for π pulses were determined to be $\pi_{^{15}\text{N}} 59\text{ }\mu\text{s}$ and $\pi_{^1\text{H}} 27\text{ }\mu\text{s}$. The optimized power settings for the Hartmann-Hahn polarization transfer were -15 dB on the ^{15}N channel and -19.8 dB on the ^1H channel.

We measured the longitudinal relaxation times of ^{15}N and ^1H and we obtained $T_1^{^{15}\text{N}} = 180 \pm 5\text{ s}$ and $T_1^{^1\text{H}} = 3 \pm 0.1\text{ s}$. To determine the polarization enhancement we preliminarily measured the thermal polarization signal for both ^{15}N and ^1H . The determination was performed averaging a series of spectra obtained with a simple sequence composed by a $\pi/2$ hard pulses followed by acquisition, with a repetition time of $5 T_1$. The initial continuous wave irradiation used to saturate the ^{15}N polarization was performed for 5 s with a power level of

–15 dB. The residual polarization after the irradiation was determined to be less than 5 % of the ^{15}N thermal polarization.

In the following we define $\epsilon_{^{15}\text{N}}$ and $\epsilon_{^1\text{H}}$ as the relative polarization of ^{15}N and ^1H with respect to their thermal polarization respectively. For nitrogen $\epsilon_{^{15}\text{N}}$ represents the enhancement obtained by the Hartmann-Hahn polarization transfer. For protons $\epsilon_{^1\text{H}}$ represents the residual polarization after the Hartmann-Hahn transfer.

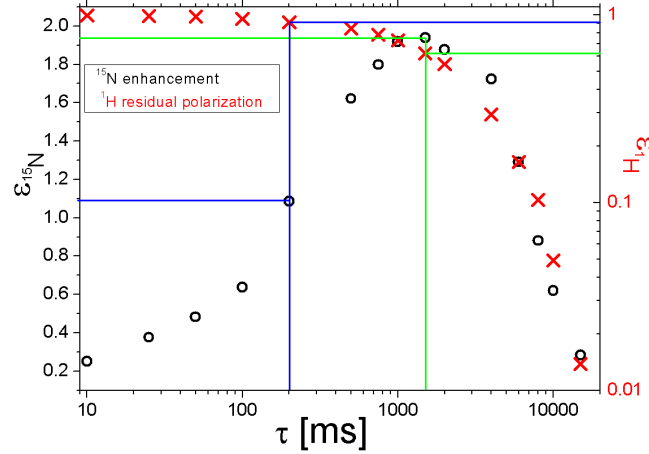


Figure 5.3: ^1H to ^{15}N relative polarization after partial Hartmann-Hahn polarization transfer in function of the contact time τ .

Figure 5.3 shows the results of measurements of ^{15}N polarization enhancement $\epsilon_{^{15}\text{N}}$ and of ^1H residual polarization $\epsilon_{^1\text{H}}$ in function of the contact time τ . We obtained a maximum Hartmann-Hahn ^{15}N enhancement of $\epsilon_{^{15}\text{N}}^{HH} = 1.93$ for a contact time of $\tau = 1.5\text{ s}$ which corresponds to a proton polarization loss of about 38% (green horizontal and vertical lines in figure 5.3).

Although the lower maximum performances of the sequence, compared to the $\epsilon_{^{15}\text{N}}^{INEPT} = 9.9^{10}$, the Hartmann-Hahn has the possibility of being used for partial polarization transfers. As an example a $\epsilon_{^{15}\text{N}} = 1.1$ can be obtained with a contact time of $\tau \sim 200\text{ ms}$ destroying only about 10% of ^1H polarization (blue horizontal and vertical lines in figure 5.3).

As can be seen in figure 5.3, the main limiting factor in terms of polarization transfer efficiency is the ^1H longitudinal relaxation time. In the inverse ^{15}N to ^1H transfer the T_1 limitation is less critical due to the much longer ^{15}N T_1 .

5.4 Conclusions and Outlook

In this chapter we demonstrated the feasibility of the Hartmann-Hahn polarization transfer for ^{15}N -choline. The reversed ^1H to ^{15}N transfer shows that the maximum enhancement achievable is about $\epsilon_{^{15}\text{N}}^{HH} \sim 2$. Although this enhancement is about one fifth of the theoretical maximum, it is limited by the proton T_1 . This limitation is much less strict in the case of the

^{15}N to ^1H transfer due to the much longer ^{15}N T_1 .

Despite the lower maximum enhancement achievable, the Hartmann-Hahn ^{15}N to ^1H polarization transfer scheme has two main advantages with respect to HINDER. The first advantage is linked to relaxation: in the Hartmann-Hahn scheme the contact time can be shortened to a small fraction of $1/J$ if $\epsilon_{1H}/P_{i-}^{15\text{N}} \ll \epsilon_{1H}^{HH}$ (high ^{15}N polarization with respect to the required ϵ_{1H} as it is the case in dissolution DNP) and the relaxation time constant during the transfer $T_{1,\rho}$ is comparable to T_1 ; in the HINDER sequence (see figure 5.2-D) $\tau_2 = 1/J$ is the refocusing delay, independent of the enhancement achieved, during which the polarization decays with T_2 . T_2 being usually much shorter than T_1 for protons in biological systems, this leads to higher losses with respect to the Hartmann-Hahn scheme if τ_2 is not negligible with respect to T_2 . The second advantage of the Hartmann-Hahn sequence lies in the higher robustness of the sequence in case of mismatch in the intensity of the interaction used for the polarization transfer (dipolar coupling for Hartmann-Hahn and J -coupling for HINDER). Metabolites can have dipolar couplings and J -couplings different from the substrate molecule. In the case of the Hartmann-Hahn sequence, the phase of the polarization is always known independently on the coupling constant thus allowing to recover to the z axis all the magnetization that was not transferred. The consequence of different $^{15}\text{N} - ^1\text{H}$ dipolar couplings between substrate and metabolites will be a variation in the polarization transfer efficiency. In the case of HINDER, if a substrate has a J -coupling different from the substrate, on top of the different polarization transfer efficiency, its magnetization cannot be refocused perfectly at the end of the τ_2 refocusing period thus leading to polarization losses that increase with increasing J -coupling difference.

The work initiated in this chapter will continue with the aim of measuring choline metabolism in diseased rat brain homogenates *in vitro* by mean of dissolution DNP. Before performing the homogenates measurements a further calibration of the efficiency of the direct ^{15}N to ^1H transfer is needed.

In order to obtain precise data, dissolution DNP will be used to start from a high nitrogen signal and to assess the polarization transfer efficiency to the three non equivalent proton sites in the choline (9 protons on the three $-\text{CH}_3$ groups, 2 protons in the $-\text{CH}_2-$ group and other two protons in the $-\text{CH}_2\text{OH}$ group). Once the characteristic curves, similarly to the ones in figure 5.3, will be obtained, the optimized strategy for the measurement, as presented in Appendix C, can be calculated and used for the homogenates measurements. Finally an *a posteriori* precise measurement of T_1 for nitrogen and protons of the various metabolites in the homogenates can be used to correct the results and to increase the precision of the determination.

References

- [1] K. Glunde and N. J. Serkova. Therapeutic targets and biomarkers identified in cancer choline phospholipid metabolism. *Pharmacogenomics*, 7(7):1109–23, 2006.
- [2] K. Glunde, M.A. Jacobs, and Z.M. Bhujwalla. Choline metabolism in cancer: implications for diagnosis and therapy. *Expert Review of Molecular Diagnostics*, 6:821–829, 2006.
- [3] F. Podo. Tumour phospholipid metabolism. *NMR in biomedicine*, 12:413–439, 1999.
- [4] C-W Li, Y.C. Kuo, C-Y Chen, Y-T Kuo, Chiu Y-Y, F-O She, and G-C Liu. Quantification of choline compounds in human hepatic tumors by proton MR spectroscopy at 3 T. *Magnetic Resonance in Medicine*, 53:770–776, 2005.
- [5] M.C. Gustafsson, O. Dahlqvist, J. Jaworski, P. Lundberg, and A.-M.E. Landtblom. Low choline concentrations in normal-appearing white matter of patients with multiple sclerosis and normal MR imaging brain scans. *American Journal of Neuroradiology*, 28:1306–1312, 2007.
- [6] H. Allouche-Arnon, A. Gamliel, C. M. Barzilay, R. Nalbandian, J. M. Gomori, M. Karlsson, M. H. Lerche, and R. Katz-Brull. A hyperpolarized choline molecular probe for monitoring acetylcholine synthesis. *Contrast Media Mol Imaging*, 6(3):139–47, 2011.
- [7] H. Allouche-Arnon, M. H. Lerche, M. Karlsson, R. E. Lenkinski, and R. Katz-Brull. Deuteration of a molecular probe for DNP hyperpolarization - a new approach and validation for choline chloride. *Contrast Media Mol Imaging*, 6(6):499–506, 2011.
- [8] C. Gabellieri, S. Reynolds, A. Lavie, G. S. Payne, M. O. Leach, and T. R. Eykyn. Therapeutic target metabolism observed using hyperpolarized ^{15}n choline. *J Am Chem Soc*, 130(14):4598–9, 2008.
- [9] K. Kumagai, K. Kawashima, M. Akakabe, M. Tsuda, T. Abe, and M. Tsuda. Synthesis and hyperpolarized ^{15}n NMR studies of ^{15}n -choline-d13. *Tetrahedron*, 69(19):3896–3900, 2013.
- [10] R. Sarkar, A. Comment, P. R. Vasos, S. Jannin, R. Gruetter, G. Bodenhausen, H. Hall, D. Kirik, and V. P. Denisov. Proton NMR of N-15-Choline metabolites enhanced by dynamic nuclear polarization. *Journal of the American Chemical Society*, 131(44):16014–+, 2009.
- [11] T. Harris, P. Giraudeau, and L. Frydman. Kinetics from indirectly hyperpolarized NMR spectroscopy by using spatially selective coherence transfers. *Chemistry - A European Journal*, 17:697–703, 2011.
- [12] V.A. Norton and D.P. Weitekamp. Partial polarization transfer for single-scan spectroscopy and imaging. *J. Chem. Phys.*, 135:141107, 2011.
- [13] S.R. Hartmann and E.L. Hahn. Nuclear double resonance in the rotating frame. *Physical Review*, 128:2042–2053, 1962.

6 Hyperpolarized ^{13}C NMR at 14.1 T

Abstract

Even with a high signal intensity it is difficult to quantify metabolites that are close in the spectrum, compared to the actual *in vivo* linewidth. In particular, the ^{13}C spectrum of labeled $R-^{13}\text{COOH}$ molecules, metabolites of $[1-^{13}\text{C}]$ -acetate, is crowded in proximity of the $[1-^{13}\text{C}]$ -acetate peak at 182.6 ppm. The closeness of the metabolites peaks to the acetate peak leads to difficult or impossible resolution of the metabolites peaks from the hyperpolarized acetate peak, or among them, in conditions where the shimming is hard to perform, *in vivo* in muscles for instance.

Increasing the field intensity for *in vivo* hyperpolarized MR experiments improves spectral resolution. The increased spectral resolution directly reflects in higher peak separation of the different metabolites leading to the possibility of resolving peaks very close in the spectrum. One of the major technical challenges to perform *in vivo* dissolution DNP at ultra high field is due to the large distance between the polarizer and the MRI magnet. Since there is no actively shielded MRI magnet above 11.7 T the distance traveled by the dissolved hyperpolarized solution, and thus the time needed to transfer the solution from the prepolarizer to the MR magnet, is increased with respect to MR imagers at lower field. This increased transfer time leads to increased signal losses that have to be minimized through optimization of the dissolution and transfer procedure.

In this chapter we show the hardware implementation of the new cryostat presented in chapter 2 with a horizontal 14.1 T Varian rodent MRI scanner. The first *in vitro* DNP experiments performed at 14.1 T are presented.

6.1 Hardware

The polarizer presented in chapter 2^{1;2} was coupled to a 14.1 T Varian rodent MRI scanner to perform dissolution DNP measurements *in vitro* and *in vivo*.

The main issue arising from the implementation of this system came from the long distance between the polarizer and the non shielded MRI scanner. Increasing the distance between polarizer and scanner leads to an increase in transfer time the hyperpolarized solution has to travel and therefore increases losses in polarization through relaxation. In addition, the hyperpolarized solution may spend a non-negligible time in regions of low magnetic field where the relaxation times are often shorter, at least for ^{13}C in carboxylic groups. Significant losses of polarization during the transfer may occur if care is not taken.

Sources of polarization loss

On a given sample, the polarization losses during the transfer from the polarizer to the MRI scanner, are mainly due two causes:

- the first cause is linked to the absolute value of the magnetic field intensity. The relaxation rate can dramatically vary with magnetic field and in many molecules of interest, the nuclear relaxation T_1 becomes very short at low magnetic field. In the extreme case, the sample could cross a region where $B_0 \sim 0$ which would lead to a degeneration of the levels of the spin system, completely destroying the polarization;
- the second cause originates from the rapid time variation of the coupling between nuclear spins and external magnetic field during sample transfer, *i.e.* if the quantum mechanical adiabatic condition is not fulfilled^{3;4}. If the external magnetic field experienced by the nuclear spins, and thus the Zeeman Hamiltonian varies too rapidly, the nuclear magnetization will not be colinear with the external field. A loss of polarization is produced because the spin state cannot continuously stay in an eigenstate of the local Hamiltonian and consequently a high rate of transition is induced.

In the case of the present system, *i.e.* a polarizer placed in the fringe field of an unshielded 14.1 T magnet, the absolute value of the magnetic field intensity never decreases below 50 – 100 G.

The fringe field generated by the MRI scanner in figure 6.1-left across the room where the polarizer is located is relatively intense. The 50 G line of the 14.1 T MRI scanner is located more than 6 m away from the magnet. In addition, the fringe field generated by the 5 T polarizer magnet shown in figure 6.1-right, adds up. The sum of the two fringe fields added keeps the overall field above 50 G all along the path of the transferred hyperpolarized solution. This field is large enough to limit losses caused by T_1 relaxation to less than ten percent in molecules like $[1-^{13}\text{C}]\text{-acetate}$ ⁵.

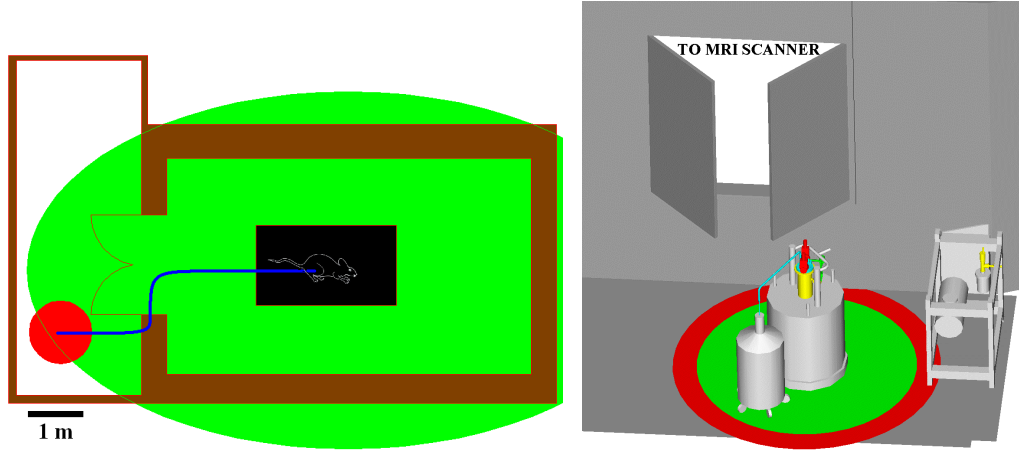


Figure 6.1: Left: diagram of the fringe field (green: region above 50 G for the isolated 14.1 T magnet) generated by the 14.1 T MRI scanner (black rectangle) across the room where the polarizer (red circle) is located. The blue line represents the hyperpolarized solution transfer path. Right: image of 5 T magnet with the DNP polarizer inserted and storage dewar on the side. The red circle represents the 50 G limit for the isolated 5 T magnet.

However, care must be taken to avoid polarization losses due to the rapid field variations linked to the adiabatic condition. The field variation can be decomposed in two parts: the component parallel to $\vec{B}(t)$, $\vec{B}_{\parallel}(t)$, which modifies the energy of the spin states but do not cause transitions and the component perpendicular to $\vec{B}(t)$, $\vec{B}_{\perp}(t)$, which induces transitions. For our purposes, the adiabatic condition can be written as:

$$\int \frac{E(|\vec{B}_{\perp}(t)|^2)}{|\vec{B}(t)|} dt \ll 1 \quad (6.1)$$

where: $E(|\vec{B}_{\perp}(t)|^2)$ is the expectation value of the square of the magnetic field variation perpendicular to the actual $\vec{B}(t)$ direction. This is proportional to the instantaneous transition probability per unit of time according to the Fermi's golden rule. The integral has to be taken along the transfer path of the hyperpolarized solution. If the condition is not met, the spins states have not enough time to follow the varying Hamiltonian eigenstates. This causes transitions that do not conserve energy, and can lead to severe loss of polarization.

To minimize relaxation caused by the two effects described above the best strategy consists in:

- maximizing the speed and minimizing the transfer path length, and thus time, of the transfer. This can be obtained by shortening the transfer line;
- define a transfer path where the field intensity $|\vec{B}(t)|$ is as large as possible at all loca-

tions;

- avoid the regions that are too close to sources of large magnetic field gradient, in particular the magnetic parts of the frame surrounding the MRI scanner.

Optimized setup

The main challenge associated with the installation of the setup was to determine a path across the Faraday cage surrounding the MR scanner room that complies with the two limitations described above, *i.e.* minimum length of the transfer path and minimum external magnetic field variation along the path. The locations where a high field gradient is present are the surrounding of the metallic pillars of the frame structure and the space close to the waveguides crossing the frame itself.

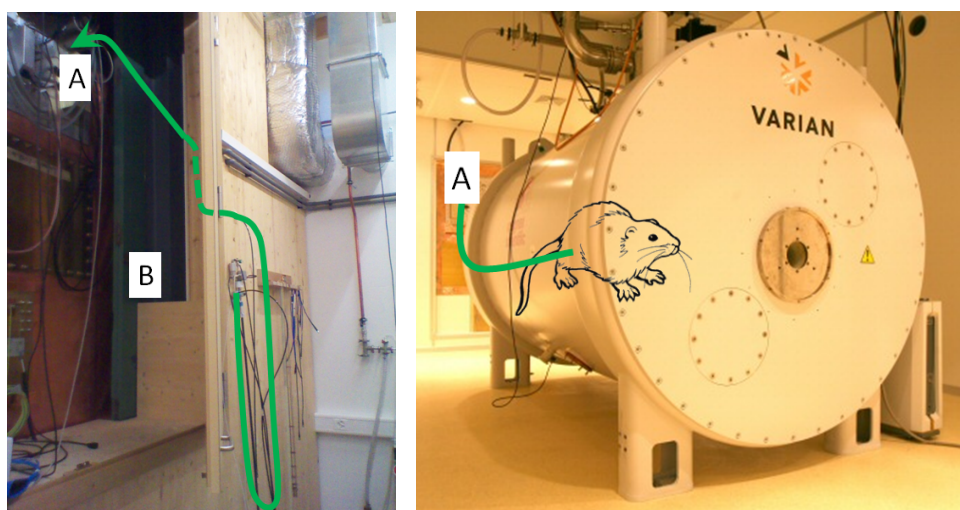


Figure 6.2: Transfer path (green line) in the polarizer room (left) and in the MRI scanner room (right). A) waveguide used for the transfer line to cross the Faraday cage; B) metallic pillars.

The transfer line shown in green in figure 6.2, was as short as possible. It passes through the outer wooden wall and turns around the metallic pillars (B) at a distance of about 20 cm. Because the pillars are magnetized from the interactions with the field of the scanner, the stray field experienced by the spins in the hyperpolarized solutions is highly distorted in the vicinity of the pillars. It is thus necessary to avoid placing the transfer line at proximity of the pillars. The line was placed away from the metallic waveguide (A) surface and passed exactly in its central axis for the same reasons, although the magnetization is relatively low in aluminum alloys. Finally, the line comes out of the frame into the 14.1 T MR scanner room from the waveguide in figure 6.2-A at a position close to the axis of the 14.1 T magnet and goes straight to the infusion pump located inside the magnet bore near the isocenter.

The syringe pump was placed outside of the 14.1 T MR scanner room to avoid accidents and interferences with the pump. The line used to push the piston of the infusion pump

passed through the same waveguide as the one used for the transfer line.

With respect to the already installed setup¹ the optimal transfer time was increased to 5 s due to the increased length of the transfer line that is about 7 m long. To obtain this timing, the helium gas pressure maintained during transfer had to be increased to 6.5 bar. These settings allows to collect 2 mL of the hyperepolarized solution into the infusion pump in the 14.1 T MR scanner.

6.2 Results

In vitro

A sample of 4.5 M $[1-^{13}\text{C}]$ -acetate in 2 : 1 D_2O :d6-ethanol with 33 mM TEMPOL has been DNP polarized in the 5 T prepolarizer at 1.1 ± 0.05 K. The solid-state polarization build-up curve, obtained with single low flip angle ($\theta < 5^\circ$) pulses, for the acetate sample is presented in figure 6.3-A in black. The data were fitted with a mono-exponential function to determine the build-up time constant $T_B = 1750 \pm 40$ s. Figure 6.3-B shows the DNP enhanced spectrum obtained by a single measurement on the polarized sample.

To assess the polarization losses during the dissolution procedure a polarization measurement was performed directly into the infusion pump in the 14.1 T MR scanner. The hardware and procedure used for this measurement is essentially identical to the ones described in an early publication⁶. Once the hyperpolarized solution was transferred into the infusion pump, a train of calibrated $\theta = 10^\circ$ pulses was applied every 3 s to measure the signal intensity decay. Once the ^{13}C polarization relaxed to thermal equilibrium, a series of $\pi/2$ pulses was applied every 5 T_1 and the signals were averaged to determine the thermally polarized signal.

Finally the enhancement ϵ was calculated, accounting for the different pulses used in the two measurements, through:

$$\begin{aligned}\epsilon &= \frac{S_{DNP}}{S_{th} \cdot \sin \theta} \\ \epsilon_R &= \frac{14.1\text{ T}}{9.4\text{ T}} \cdot \epsilon\end{aligned}\tag{6.2}$$

where: S_{DNP} is the maximum signal obtained after the first pulse, S_{th} is the averaged thermal signal and ϵ_R is the equivalent enhancement that would have been obtained in a field of 9.4 T, to perform comparison with previous measurements made with the same sample on the PSI polarizer coupled to the 9.4 T MR scanner. For a direct comparison it is also necessary to consider the additional losses of polarization due to the longer transfer path.

The results of the test dissolution and transfer in the infusion pump are shown in figure 6.3. The signal decay (C) was fitted with a mono-exponential function to obtain a $T_1 = 11.7$ s after correction for the effect of RF pulses. The calculated enhancement from the signal shown

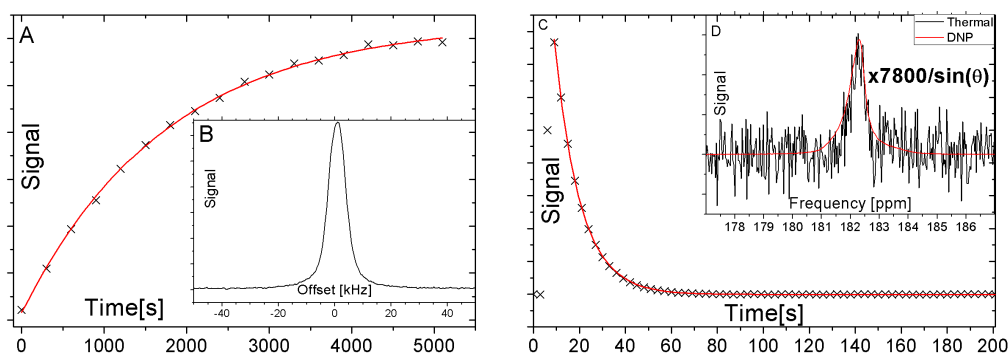


Figure 6.3: A) buildup time course for acetate solid-state polarization; B) solid-state 1 K acetate spectrum; C) time course of hyperpolarization decay in the infusion pump; D) hyperpolarized and rescaled thermal signal in the infusion pump overlapped.

in (D) was $\epsilon = 7'800$. Rescaling this value, the enhancement would correspond, in the 9.4 T MR scanner, to a value of $\epsilon_R = 11'700$. Furthermore if we consider the additional loss in the transfer line due to the longer transfer time, ϵ_R is coherent with the results obtained in the system coupled to the 9.4 T scanner.

These results show that the path chosen for the transfer does not produce significant effects on the polarization and the system is suitable for *in vivo* experiments.

In vivo

An *in vivo* experiment on rat leg muscle with femoral vein cannulation was performed. 1.6 mL of the solution obtained from dissolving the same sample as described in the previous section was injected in the femoral vein of a rat and the acquisition performed with a single loop ^{13}C coil.

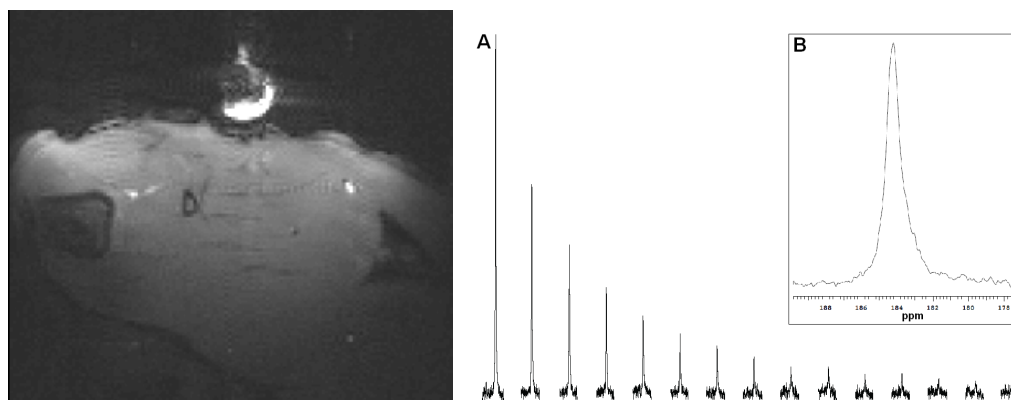


Figure 6.4: Left: anatomic proton image of the rat leg muscle; Right: A) signal decay of the hyperpolarized $[1-^{13}\text{C}]$ -acetate peak with an *in vivo* $T_1 = 7 \pm 0.3\text{ s}$; B) sum of the signal of all the spectra.

Figure 6.4-A shows the anatomic proton image of the rat leg where the surface coil sensitivity is maximum. On Figure 6.4-B a time course of the signal obtained from calibrated 10° flip angle pulses is presented. The protocol used was essentially identical to the one used in previous rat muscle experiments⁷. In this experiment the shimming quality was not sufficient to obtain a low enough metabolites peaks linewidth to detect acetate metabolites signals. Although optimization is still required we demonstrated the feasibility of dissolution DNP at 14.1 T MRI scanner field.

6.3 *In vivo* outlook

The aim of this section is to demonstrate the possibility to resolve peaks of $[1-^{13}\text{C}]$ -acetate metabolites *in vivo* in muscles.

The ^{13}C at a $R-\text{COO}^-$ site (carboxyl functional group) is surrounded only by atoms without spin (^{16}O and ^{12}C). For this reason it has a relatively long T_1 in liquid state thus making acetate and its metabolites ideal candidates for observation in dissolution DNP techniques. In addition, because it is spatially isolated from other nuclear magnetic moments, the ^{13}C resonances of acetate and its metabolites are spectrally very close to one another, with a chemical shift of about 182 ppm (see table 6.1).

Molecule	Chemical shift
Acetate	182.6
Citrate	179.7
2-oxo Glutarate	182.5
Glutamate	182.4
Butyrate	185.0

Table 6.1: List of chemical shifts of ^{13}C in some $R-^{13}\text{COOH}$ molecules.

Glutamate is a metabolite that is present in sufficiently large concentration that it can usually be detected following the injection of $[1-^{13}\text{C}]$ -acetate⁸ without hyperpolarization. Since its chemical shift is only 0.2 ppm away from acetate, it is challenging to resolve this metabolite signal *in vivo* when a large signal from the hyperpolarized substrate is hindering the small peaks. In a 9.4 T MRI scanner, previous experiments in the rat heart⁹ have shown that the glutamate peak is clearly visible when $[1-^{13}\text{C}]$ -butyrate is injected instead of $[1-^{13}\text{C}]$ -acetate. In muscles it was indeed not possible to see the glutamate peak after the injection of $[1-^{13}\text{C}]$ -acetate⁷.

Increasing the field to 14.1 T enhances the spectral dispersion due to chemical shift of about 50% allowing to resolve acetate metabolites. The protocol for the *in vivo* experiments performed in further optimizations will be essentially identical to the one used in previous rat muscle experiments⁷.

References

- [1] A. Comment, B. van den Brandt, K. Uffmann, F. Kurdzesau, S. Jannin, J. A. Konter, P. Hautle, W. T. H. Wenckebach, R. Gruetter, and J. J. van der Klink. Design and performance of a DNP prepolarizer coupled to a rodent MRI scanner. *Concepts in Magnetic Resonance Part B-Magnetic Resonance Engineering*, 31B(4):255–269, 2007.
- [2] S. Jannin, A. Comment, F. Kurdzesau, J. A. Konter, P. Hautle, B. van den Brandt, and J. J. van der Klink. A 140 GHz prepolarizer for dissolution dynamic nuclear polarization. *Journal of Chemical Physics*, 128(24):241102, 2008.
- [3] T. Kato. On the adiabatic theorem of quantum mechanics. *Journal of the Physical Society of Japan*, 5:435–439, 1950.
- [4] B. Simon. Holonomy, the quantum adiabatic theorem, and berry's phase. *Physical Review Letters*, 51:2167–2170, 1983.
- [5] P. Mii $\frac{1}{2}$ ville, S. Jannin, and G. Bodenhausen. Relaxometry of insensitive nuclei: Optimizing dissolution dynamic nuclear polarization. *Journal of Magnetic Resonance*, 210:137–140, 2011.
- [6] Tian Cheng, Mor Mishkovsky, Jessica A. M. Bastiaansen, Olivier Ouari, Patrick Hautle, Paul Tordo, Ben van den Brandt, and Arnaud Comment. Automated transfer and injection of hyperpolarized molecules with polarization measurement prior to in vivo NMR. *NMR in Biomedicine*, pages n/a–n/a, 2013.
- [7] J.A.M. Bastiaansen, T. Cheng, M. Mishkovsky, J.M.N. Duarte, A. Comment, and R. Gruetter. In vivo enzymatic activity of acetyl-CoA synthetase in skeletal muscle revealed by ^{13}C turnover from hyperpolarized $[1 - ^{13}\text{C}] \text{acetate}$ to $[1 - ^{13}\text{C}] \text{acetylcarnitine}$. *Biochimica et Biophysica Acta*, 1830:4171–4178, 2013.
- [8] Lidia Szczepaniak, Evelyn E. Babcock, Craig R. Malloy, and A. Dean Sherry. Oxidation of acetate in rabbit skeletal muscle: Detection by ^{13}C NMR spectroscopy in vivo. *Magnetic Resonance in Medicine*, 36(3):451–457, 1996.
- [9] J.A.M. Bastiaansen, M. Merritt, and A. Comment. In vivo myocardial substrate competition using hyperpolarized ^{13}C magnetic resonance. *Circulation*, 2013.

7 MRI segmentation method for granular material reconstruction

Abstract

Granular materials are complex systems composed by a large number of particles that interact mainly via contact forces¹⁻³. Furthermore, the large number of particles suggests that statistical effects could provide an explanation of the observed thermodynamical features. Unfortunately, the nature of granular samples makes direct observation of their inner structure a very complex task. By using magnetic resonance imaging (MRI), we observed a granular system in a non-destructive, non-invasive way. In the past, mainly due to resolution constraints, the MRI approach was only used to study average dynamics of flows in granular media^{4;5}. In this work, we show a method, based on real space thresholded Hough transform, to extract and completely reconstruct sphere by sphere the complete 3D structure of millimeter sized granular media. The measured data allow us to access both global and local properties of static granular media.

7.1 Methodology

Our sample is composed of 3 mm nominal diameter d plastic spheres (polyoxymethylene). The average beads volume was measured directly through the Archimede's method, to obtain a value of $V_b = 14.348 \text{ mm}^3$ thus a diameter of $d = 3.015 \pm 0.005 \text{ mm}$. This correction is about 1.5% with respect to the nominal volume and must be taken into account in all the determinations involving the density or scaling through the beads diameter.

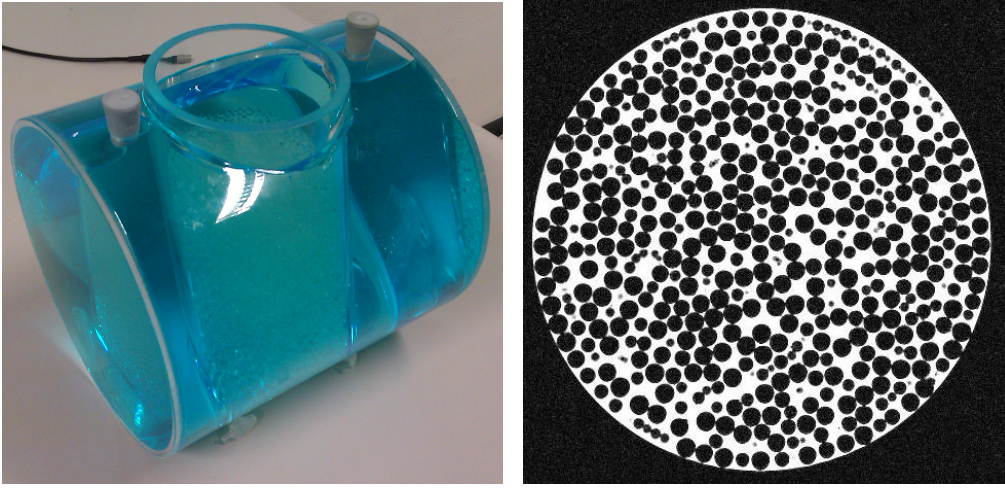


Figure 7.1: Left: cylindrical sample holder for MRI measurements. Right: example of an acquired horizontal slice.

The phantom is a horizontal cylindrical container, shown in Figure 7.1-left. It contains another vertical cylinder to actually contain the plastic spheres. The outer horizontal cylinder is filled with D_2O . On one hand, due to the absence of protons, this avoids the presence of high amount of unwanted signal originating outside the region actually containing the beads. On the other hand the horizontal cylinder is the ideal shape to obtain a good shimming because of the shimming coil geometry, based on cylindrical harmonics, and because it is pretty homogeneous, being the electric and magnetic properties of D_2O very close to ones of the solution in the central cylinder.

The central, vertical, cylinder is filled with beads poured in a water solution of 40 mM of $CuSO_4$ used as relaxing agent in order to speed up the acquisition. The proton relaxation times at this concentration are roughly $T_1 \sim T_2 \sim 20 \text{ ms}$.

Since our purpose consists on demonstrating the technique, the beads are placed in the container with the $CuSO_4$ solution and then compacted through a mild shaking overnight without aiming at a particularly high compaction.

MRI acquisition

The packings were scanned in a Siemens 7 T clinical scanner using a birdcage MRI volume coil⁶ (designed to accommodate a human head). The 3D images were then acquired using a standard Gradient Echo Imaging (GRE)⁷ technique ($TR = 50\text{ ms}$, $TE = 3.79\text{ ms}$, total acquisition time 6 h).

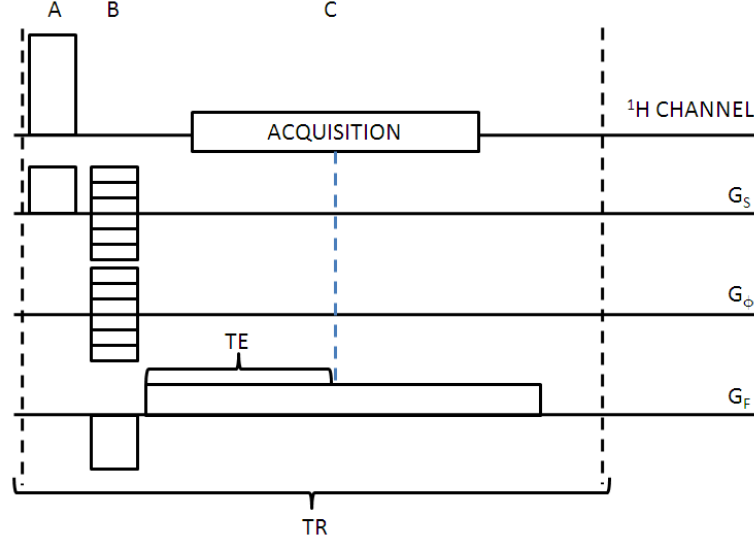


Figure 7.2: Gradient echo sequence: A) volume selection RF pulse and gradient G_S which rotates only those spins in the imaged volume of the object; B) phase encoding gradient in dimension 1 G_S and in dimension 2 G_ϕ , the gradient on G_F is used to create the echo exactly in the center of the acquisition time; C) acquisition period, the spatial information is frequency encoded by G_F and an echo is acquired. TR and TE are the repetition time and the echo time respectively.

The output 3D matrix (Figure 7.1-right) consisted of a water density map with an isotropic resolution of $0.2\text{ mm} \sim d/15$. The dark zones give, by contrast, the volume occupied by the beads. The presence of only D_2O in the outer cylinder produces the complete absence of spurious signal outside the beads region. Furthermore, the cylindrical shape of the phantom allows for a very good shimming decreasing distortions. Both resolution and contrast are high enough to reconstruct the structure with very high precision.

7.2 Reconstruction algorithm

The raw data matrix $\mathbb{I}_r(x, y, z)$ (Figure 7.1-right) is treated as a full 3D image in the following way.

3D acquired matrix threshold

A binary local threshold, based on two parameters, was applied to the raw data. We start determining a local threshold value associated to each voxel. Each voxel is compared to the maximum and minimum values of other voxels at a distance lower than a certain radius:

$$T(x, y, z) = (\max(\mathbb{I}_r(x', y', z')) - \min(\mathbb{I}_r(x', y', z'))) \cdot t + \min(\mathbb{I}_r(x', y', z')) \quad (7.1)$$

where: $T(x, y, z)$ is the threshold value for the examined voxel (x, y, z) ; $0 < t < 1$ is a free parameter; maxima and minima are taken with the condition $|(x - x', y - y', z - z')| < R_T$; R_T , the second free parameter, is the threshold radius used.

Based on the local thresholds $T(x, y, z)$ of equation 7.1, the voxel of the thresholded image \mathbb{I}_t is then set to 1 only if its value is below the threshold (the voxel of the acquired image $\mathbb{I}_r(x', y', z')$ is recognized as black meaning is inside a sphere) 0 otherwise:

$$\mathbb{I}_t(x, y, z) = \theta(T(x, y, z) - \mathbb{I}_r(x, y, z)) \quad (7.2)$$

where: $\theta(\cdot)$ is the Heaviside function. All the voxels of the thresholded image \mathbb{I}_t to which a value of 1 is associated, were positively recognized as inside a bead.

With this definition the parameter t can be interpreted as the thresholding strength. $t = 0$ and $t = 1$ are extreme cases producing a complete black or white $\mathbb{I}_t(x, y, z)$ respectively.

A global threshold cannot be applied efficiently, due to the presence of non negligible variation in brightness along the acquired image. The local threshold is then necessary to compensate these changes.

In our case the choice of the free parameters is not extremely critical for the thresholding quality:

- the thresholding radius in equation 7.1 has to be chosen $R_T > d/2$ to comprehend voxels filled with water even when the voxels in exam is exactly in the center of a plastic sphere. The criterion we chose is to keep R_T as low as possible keeping a large enough number of water filled voxels to obtain a reliable estimate of $\max(\mathbb{I}_r(x', y', z'))$ for the region, also in the worst case of a (x, y, z) voxel in a bead center. We used $R_T = 1.5d$ for all the determinations;
- the results are not strongly dependent on the thresholding strength t while in the range $0.25 < t < 0.75$. Increasing t produces an increase in the apparent bead size and blurs

the contact points making them bigger. On the other hand decreasing t helps in separate the spheres but with the drawback of losing positive matches in voxels into the beads. Thanks to the high Contrast to Noise Ratio (CNR) of the acquired images, and to limit the arbitrariness of the parameters choice, we kept the value at $t = 0.5$.

Real space spherical thresholded Hough transform

At this stage the image \mathbb{I}_t obtained from equation 7.2 still shows the beads regions touching, making difficult to define and separate the different beads.

To obtain a good separation we chose to perform a thresholded spherical Hough transform⁸ in real space to \mathbb{I}_t . Also this is a two free parameters transformation. This treatment has the objective to identify voxels close to the spheres centers. In this way isolated agglomerates of voxels are produced. These agglomerated are then easily recognized and associated to a bead center.

First the sum of the values of \mathbb{I}_t within a certain distance R_H from the voxel (x, y, z) in exam is calculated.

Then the corresponding voxel of the transformed image \mathbb{I}_H is set to 1 only if the number of active voxels is over a certain fraction of the total volume h , 0 otherwise:

$$\begin{aligned} H(x, y, z) &= \sum \mathbb{I}_t(x', y', z') \theta(R_H - |(x - x', y - y', z - z')|) \\ n_H = n_H(x, y, z) &= \sum \theta(R_H - |(x - x', y - y', z - z')|) \end{aligned} \quad (7.3)$$

where: H is the value of the spherical Hough transform with a radius of R_H and n_H is the number of summed voxels. $\theta(R_H - |(x - x', y - y', z - z')|)$ is the kernel of the spherical Hough transform.

Then after the transformation, the threshold is applied similarly to equation 7.2 to obtain again a binary image:

$$\mathbb{I}_H(x, y, z) = \theta\left(\frac{H(x, y, z)}{n_H} - h\right) \quad (7.4)$$

where: \mathbb{I}_H is the image after the thresholded Hough transform and h is the threshold value.

\mathbb{I}_H in equation 7.4 shows almost spherical shaped agglomerates of voxels separated by more than $d/4$.

In this case, although the parameters resembles the ones used for the first threshold, they have a different meaning and their choice is much more critical to obtain agglomerates

that are on one hand well separated, and on the other hand as big as possible to increase the reconstruction precision:

- the spherical Hough transform radius R_H in equation 7.3 has to be chosen carefully: if it is too big the average is done on a wide region, blurring the results; if it is too small the voxel agglomerates obtained are not well separated because the contact region between beads is bigger than the Hough transform radius.

To optimize this parameter we repeated the reconstruction with a wide set of diameters and chose a value in between the range in which the previous conditions of good separation and biggest volumes were satisfied. We used $R_T = \frac{1}{3}d$ for all the determinations;

- with a careful choice of R_H , the results are not strongly dependent on the thresholding strength h while it is close enough to 1. The hough transform $H(x, y, z)$ in equation 7.3 consists basically of sharp, roughly circular regions of diameter smaller than the beads diameter, surrounded by values sensibly lower. Setting $0.9 < h < 0.99$ does not change much the transformation quality, while lower values start to produce connected voxel agglomerates. We kept this value at $h = 0.975$ for all the determinations.

The image is then post processed to get rid of every signal coming from outside the sample volume and to eliminate isolated voxel. The number of isolated voxels, located in the space between beads, were only a small fraction of the number of beads. On average a cluster was composed by more than a hundred voxels.

Beads center determination

The agglomerates produced in the binary image \mathbb{I}_H are then associated to a bead with center in the agglomerate center of mass.

To ensure the perfect reconstruction of the sample we used a very conservative strategy. In the first step we identified every agglomerate of voxels with a simple connectivity criterion. Then we determined the properties of the agglomerate (*e.g.* minimum bounding sphere radius, sphericity, minimum distance between other agglomerates, number of voxels) and only if all the parameters were in a meaningful range (*e.g.* minimum bounding sphere radius lower than beads radius) then the agglomerate was positively recognized as a sphere.

All the remaining non-recognized agglomerates were then 3D plotted and a manual check done. Normally the unrecognized agglomerates are composed by some 5 beads at most and they reside close to the cylinder walls or the bottom surface. The presence of these unrecognized connected agglomerates of beads is mainly due to not perfect signal cleaning outside the sample region.

The absence of unrecognized agglomerates inside the sample region guarantees that no sphere was missed in the reconstruction.

All the data processing was performed using a C program written *ad-hoc* that manages all

the calculation from the initial 3D matrix $\mathbb{I}_r(x, y, z)$ to the list of coordinates of beads centers. On average a complete reconstruction of a 15'000 beads sample with a MRI resolution $d/15$ takes about one hour on a desktop dual core PC with the algorithm scaling roughly linearly with the image volume or number of beads.

7.3 Data analysis and results

The mathematical and geometrical analyses of the spheres position were based on the sphere-sphere correlation function and on Voronoi polyhedra space decomposition respectively.

Modified correlation function

The two body correlation function $f(r)$ is defined as:

$$f(r) = \left\langle \frac{N_\delta(r) \cdot V_b}{V_\delta(r)} \right\rangle \quad (7.5)$$

where: $V_\delta(r)$ is the volume of the spherical shell of average radius r and thickness δ centered in the bead center; $N_\delta(r)$ is the number of sphere centers located within the distance interval $\left(r - \frac{\delta}{2}, r + \frac{\delta}{2}\right)$; the average value (indicated with $\langle \cdot \rangle$) is taken over all the spheres located within the actual region of interest (ROI). The shell thickness δ was adjusted to obtain a good compromise between noise and resolution (in our case $\delta \sim 10^{-3}d$).

The function $f(r)$ contains information about local structure, medium range order and long range average sample density. It can only be calculated for particles that are at least at a distance r from the ROI borders thus significantly decreasing the quantity of useful spheres available for long range determinations, especially in small-sized ROI.

To overcome this limitation of equation 7.5, following the idea of Scott⁹, we introduced a corrected correlation function $f_c(r)$ that overrides the limitation through the substitution of $V_\delta(r)$ by $V_\delta^{int}(r)$, its fraction intersecting the ROI, such as to have:

$$f_c(x) = \left\langle \frac{N_\delta(x) \cdot V_b}{V_\delta^{int}(x)} \right\rangle \quad (7.6)$$

where we define $x = \frac{r}{d}$ to normalize the distances by the sphere diameter and thus have a general expression that is independent of the sphere size.

With the corrected correlation function in equation 7.6 the number of beads available for determination for high values of x is considerably increased, especially in small sized-ROIs the increase of precision can be close to an order of magnitude.

This allows to use the correlation function to precisely determine a boundary effects free sample density even for dataset of only 1'000 ~ 1'500 spheres.

Finally, defining P_1 as the exact position of the center of the sharp peak close to $x \sim 1$ (obtained by a Gaussian fitting on the top part to avoid tail distortions) we can rescale $f_c(x)$ in the following way:

$$\begin{aligned} x' &= \frac{x}{P_1} \\ f'_c(x') &= \frac{f_c(x)}{\rho} \end{aligned} \tag{7.7}$$

to obtain a correlation function $f'_c(x')$ corrected for the overall sample density and for the average *quasi*-mechanical nearest neighbors distance represented by P_1 .

Voronoi space decomposition

A geometrical analysis based on Voronoi polyhedra¹⁰ was performed to extract structural information from our data.

Given a set of sphere centers, the Voronoi polyhedron associated to each sphere can be defined as the polyhedron which points are closer to the sphere center in exam, than all the other centers.

An operational way to determine a Voronoi polyhedron is to consider all the vectors connecting the sphere centers to the sphere in exam; then for each connecting vector a plane is constructed perpendicular to the vector and intersecting its middle point. The Voronoi polyhedron for that sphere is given by the volume, comprising the bead center in exam, enclosed by all the planes.

Then from the Voronoi polyhedron volume V_i of the i^{th} bead, a local density can be defined as:

$$\rho_i = \frac{\pi d^3}{6V_i} \tag{7.8}$$

then dividing by the average density:

$$\tilde{\rho}_i = \frac{\rho_i}{\langle \rho_i \rangle} \tag{7.9}$$

we obtain a set of single bead rescaled average density $\tilde{\rho}_i$ which distribution can be compared across samples with different average densities.

The spheres generating Voronoi polyhedron faces are defined as geometrical neighbors of the bead in exam¹⁰.

From these we can calculate the values of Steinhardt order parameters Q_l defined as follows:

$$\begin{aligned} Y_{lm} &= e^{im\phi} P_l^m(\cos\theta) \\ q_{lm} &= \frac{1}{N_b} \sum_{j=1}^{N_b} Y_{lm}(r_j) \\ Q_l &= \sqrt{\frac{4\pi}{2l+1} \sum_{m=-l}^l |q_{lm}|^2} \end{aligned} \quad (7.10)$$

where: P_l^m are the Legendre polynomial of order l , θ and ϕ are the polar angles of the vectors r_j connecting the center of bead i with the centers of its N_b geometrical neighbors j . The definition of Q_l is independent of the reference frame used.

These parameter are often used to determine local ordering in disordered structures. q_{lm} can discriminate between solid-like and liquid-like ordering. Q_l are indicators very sensitive to crystalline structures. Depending on the order l used they can be more sensitive to different crystalline geometries.

In our work we choose $l = 4$ and $l = 6$ since the first is very sensitive to cubic-like lattices and the latter to icosahedral structures with 6-fold or 12-fold symmetries common in granular packings.

Results

We prepared three packings with different densities. The densities were chosen in order to be representative of the upper half of the range of disordered sphere packings, between the limits defined by the Random Loose Packing (RLP)^{11;12}, and the Random Close Packing (RCP)¹²⁻¹⁴. To avoid boundary effects, the reconstructed packings were cropped. For each sample we defined a cylindrical region of interest (ROI), the surface of which was chosen to be 4 diameters away from the packing boundaries (container walls and packing top surface) and we discarded all spheres outside the ROI.

In Figure 7.3-A a typical reconstruct sphere packing of about 15'000 spheres is shown. The entire region of interest (ROI), at 4 bead diameters from the borders is shown in color. The different color tones correspond to spheres at increasing distance from the ROI center. The gray spheres, outside the ROI were discarded for the analyses.

In Figure 7.3-BC a typical corrected correlation function $f_c(x)$ (see equation 7.6) is shown. The main information extracted from these data are highlighted in colors:

- red: average density;
- green: amplitude decay envelope;

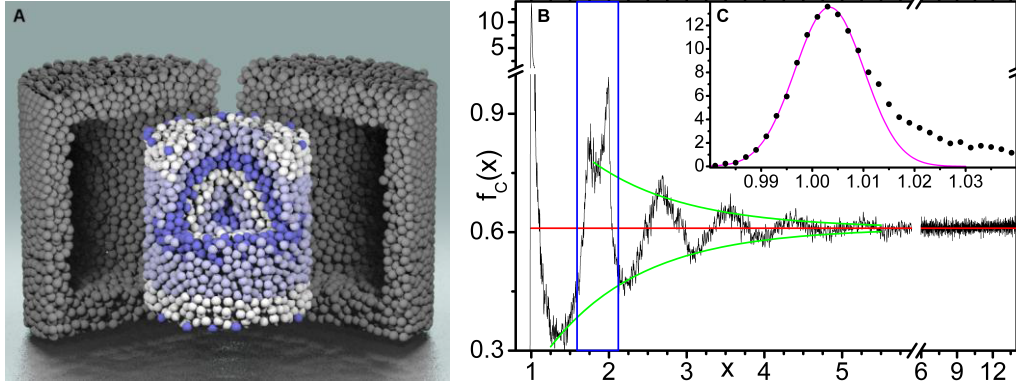


Figure 7.3: A: Computer-generated image of a reconstructed packing. B: Corrected correlation function $f_c(x)$ calculated for a typical sample. C: detail of $f_c(x)$.

- magenta: Gaussian fit of the peak at $x \sim 1$;
- blue region: observations on additional peaks on top of decay envelope. These peaks, located about $x = \{\sqrt{2}; \sqrt{3}; 2; \sqrt{5}; \dots\}$, are fingerprints of local crystalline order.

All spheres lying inside each ROI defined our entire samples respectively (in color in Figure 7.3-A). The samples were treated as a whole and we also analyzed subROIs determined by evenly dividing the entire ROI with two horizontal planes to obtain three subsamples composed of the upper, middle and lower part of the entire sample.

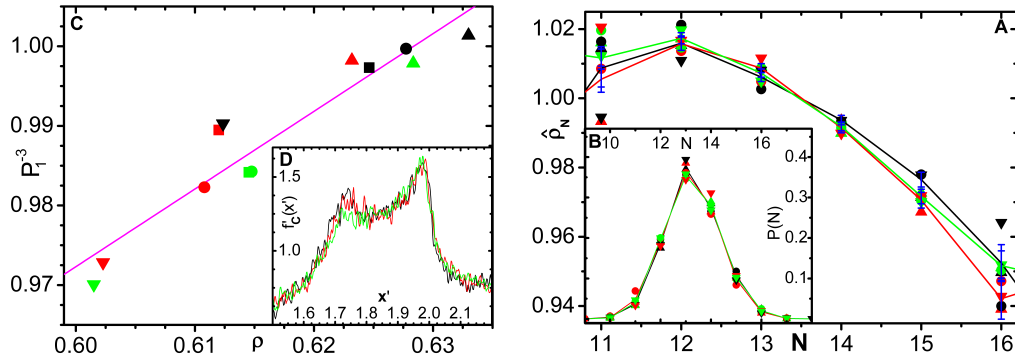


Figure 7.4: C: Inverse estimated first shell volume P_1^{-3} as a function of the average density ρ . D: Detail of the shape of $f'_c(x)$ around $x \sim 2$. A: Renormalized average single-particle density $\bar{\rho}_N$ as a function of the number of faces N of Voronoi polyhedra. B: Distribution $P(N)$ of the number of faces of the Voronoi polyhedra; vertical bars represent standard deviation for entire samples, the data corresponding to the 3 entire samples are linked by straight segments as guide for the eyes.

In Figure 7.4 some results of the relevant parameters are shown. Each color represents a sample and each symbols corresponds to a specific part of the samples (■ entire samples, ▲ upper part, ● middle part, ▼ lower part).

The value of P_1^3 can be used to estimate the average volume of the first shell of neighbors of a bead. The inverse of this volume, linked to the short-range correlations, is plotted in Figure 7.4-C for each sample and their fractional parts as a function of the average density ρ , which is an indicator of how beads arrange in the long-range. The results revealed a strong and approximately linear correlation between P_1^{-3} and ρ in the range $0.6 < \rho < 0.64$.

The rescaled correlation functions $f'_c(x)$ match both the period and amplitude of the oscillations in the region close to $x \sim 2$ as can be seen in Figure 7.4-D. Furthermore with the change $x \rightarrow \frac{x}{P_1}$, correlation functions from different samples are better superimposed also for higher values of x .

Voronoi polyhedra represent the geometrical structure not only at a local scale ($x \sim 1$) but also up to a distance of $x \sim 1.8 - 2.0$, mixing information related to the first shell and the mesoscopic region.

For all entire samples and their partial volumes we observed that $\bar{\rho}_N$ in Figure 7.4-A only varies by less than 10% over the whole range of N in which we have a significant number of measured polyhedra ($11 \leq N \leq 16$). The maximum of the average density is found at $N = 12$. As for the rescaled correlation function $f'_c(x)$, the renormalized single-particle density $\bar{\rho}_N$ is essentially identical for all samples and their subsamples. In addition, $P(N)$ appears to be independent on the sample density.

7.4 Conclusions and outlook

The present study reveals a strong correlation between the volume of the shell defined by the nearest neighbors (first shell) and the average density of the sample. To the best of our knowledge, this scaling relation is reported for the first time. Even if it is a well known fact for molecular liquids, it had been conjectured for granulars in the sixties, and subsequently abandoned. This is the first time it is directly observed in a real granular material. In general, the common belief is that the variations in densities for granular system is due to a geometrical evolution in the structure. This is in strong contrast to our observations.

The high degree of monodispersion of the beads we used, together with the high precision of the reconstruction method we proposed are crucial in obtaining the present result.

The acquisition time associated with our technique is quite long (about 6h) to obtain high spatial resolution. Although the relaxation time of protons could be further decreased adding more CuSO_4 , there are specific limitations due to the duty cycle of the gradient coils of the MRI scanner, preventing from potential drastic decrease of the repetition time. DNP could help to overcome these difficulties: a possible application could be the use of long relaxation time nuclei (such as ^6Li) to perform X-nuclei imaging in the solution surrounding the granular material. This would permit very fast acquisitions thanks to the higher SNR,

allowing to increase the sample size and the resolution of the initial image.

References

- [1] R. L. Brown and J. C. Richards. *Principles of powder mechanics*, volume 10 of *International series of monographs in chemical engineering*. Pergamon Press, 1970.
- [2] R. M. Nedderman. *Statics and Kinematics of Granular Materials*. Cambridge University Press, Cambridge, November 1992.
- [3] H. M. Jaeger, S. R. Nagel, and R. P. Behringer. Granular solids, liquids, and gases. *Rev. Mod. Phys.*, 68(4):1259–1273, Oct 1996.
- [4] T. Kawaguchi. MRI measurement of granular flows and fluid-particle flows. *Advanced Powder Technology*, 21(3):235 – 241, 2010.
- [5] E.E. Ehrichs, H.M. Jaeger, G.S. Karczmar, J.B. Knight, V.Y. Kuperman, and S.R. Nagel. Granular convection observed by magnetic resonance imaging. *Science*, 267:1632–1634, 1995.
- [6] F.D. Doty, G. Entzminger, C.D. Hauck, and J.P. Staab. Practical aspects of birdcage coils. *Journal of Magnetic Resonance*, 138:144–154, 1999.
- [7] K. Oshio and D.A. Feinberg. GRASE (Gradient-and-Spin-Echo) imaging: A novel fast MRI technique. *Magnetic Resonance in Medicine*, 20(2):344–349, 1991.
- [8] A. Rosenfeld. Picture processing by computer. *ACM Computing Surveys (CSUR)*, 1(3):147–176, 1969.
- [9] G.D. Scott. Radial distribution functions from small packings of spheres. *Nature*, 217:733–735, February, 24 1968.
- [10] G. Voronoi. Nouvelles applications des paramètres continus à la théorie des formes quadratiques. deuxième mémoire. recherches sur les paralléloèdres primitifs. *Journal für die reine und angewandte Mathematik*, 134:198–278, 1908.
- [11] G.Y. Onoda and E.G. Liniger. Random loose packings of uniform spheres and the dilatancy onset. *Phys. Rev. Lett.*, 64(22):2727–2730, May 1990.
- [12] J.G. Berryman. Random close packing of hard spheres and disks. *Physical Review A*, 27:1053–1061, 1983.
- [13] J.D. Bernal and J. Mason. Packing of spheres: Co-ordination of randomly packed spheres. *Nature*, 188(4754):910–911, Dec 1960.
- [14] G.D. Scott and D.M. Kilgour. The density of random close packing of spheres. *Journal of Physics D: Applied Physics*, 2(6):863, 1969.

8 Conclusions and Outlooks

In this thesis we covered many aspects of dissolution DNP ranging from hardware development to *in vivo* application and imaging, including solid-state NMR measurements and *in vitro* applications.

We implemented a highly automated system with a minimal user interaction for the cryogenic management. The procedures involved in the cryogenic and dissolution have been simplified with respect to the previous design, allowing for easier system handling and high customizability. The successful coupling of the new prepolarizer setup to a 14.1 T scanner allowed us to obtain the first *in vivo* hyperpolarized ^{13}C measurements in such a high-field system. Following the injection of hyperpolarized $[1-^{13}\text{C}]\text{-acetate}$ it was possible to observe the metabolite signal in rat skeletal muscle with an enhancement factor of about 8'000. Although before using this setup for routine *in vivo* experiments some optimizations of the probe will be required to achieve narrower metabolites linewidth, it should be possible to exploit the higher spectral resolution associated to the higher external magnetic field. It should be particularly well adapted to the study of substrates for which the metabolic products have chemical shifts very close to one another or to the substrate. To further improve the present prepolarizer hardware, we could consider the completion of the automation process, replacing the manually operated valves with electro-valves and servo motors. These improvements would lead to a completely automated system with the possibility to schedule operations via the software interface.

As for the solid-state NMR measurements, the method developed in this thesis could allow to perform enhancement measurements before each dissolution experiment; for an exact quantification of the amount of polarization achieved inside the polarizer. Implementing

such a measurement before each dissolution will increase the precision and reproducibility of *in vitro* and *in vivo* experiments.

We demonstrated the feasibility of using ^6Li to probe blood oxygenation levels in rat and human blood *in vitro*. The T_1 difference between oxygenated and de-oxygenated blood, in the order of 20 %, could be exploited in future applications to probe and image tissue oxygenation *in vitro* and possibly *in vivo*, with applications to the detection of tumors or ischemic regions.

We also proposed the use of partial Hartmann-Hahn polarization transfer from ^{15}N to ^1H in hyperpolarized ^{15}N -choline. This, in connection with the very long T_1 of ^{15}N in choline and the high ^1H spectral dispersion of its metabolites, allows to probe choline metabolism for very long times. A potential application of this work could be an *in vitro* study of choline metabolism of brain cells homogenates.

Finally we demonstrated that MRI can be used to study the internal structure of granular materials. We developed an acquisition and reconstruction method to determine the exact 3D position of up to 10^4 spheres contained in granular samples with a very high precision. This precision allowed us to study the structural characteristics of granular samples and observe correlations previously hidden within the measurement uncertainty. Based on this method, experiments could be designed to observe the structural properties and effects of compaction dynamics on granular samples close to the random close packing state or in partially crystalline form. Furthermore, dissolution DNP could be used to design experiments on fluidized beds coupled to very high speed acquisition schemes, exploiting the high signal obtained from hyperpolarization and the long relaxation time of nuclei such as ^6Li .

A Polarizer development

The development of the control and management hardware and procedures, for the system described in Chapter 2, will be covered in detail starting from the electronic system capabilities and instruments connected. Then the software GUI and the procedures already implemented will be presented. Finally possible hardware improvements to enhance automation will be briefly discussed.

A.1 Electronic box

All the system hardware is interfaced to a PC by mean of an electronic box. The box manages directly all the different instruments, sensors and actuators of both cryostat and dissolution insert. This setup avoids the use of multiple commercial readers decreasing the overall costs and increasing the possibilities of control of the system.



Figure A.1: Electronic box interfacing hardware instruments: left, front panel with LED indicators; right, rear panel with connectors and USB interface.

In Figure A.1 the front and rear panel of the electronic box are shown. This box directly controls different commercial instruments, as well as custom made probes:

1. Cryostat

Temperature:

- the temperature of the Separator is monitored by measuring the resistance of a calibrated Temperature Resistor;

Appendix A. Polarizer development

- at the bottom of the cryostat, close to the sample, the temperature is monitored by mean of another calibrated Temperature Resistor;
- the main insert top plate temperature is monitored trough a *Pt 100* resistor;
- in the Outer Vacuum Chamber the temperatures of the two Radiation Screens are monitored by mean of two *Pt 1000* resistors;

Helium Level: using a Superconductive wire stick it is possible to relate the measured resistance with the lenght of wire outside liquid helium. To perform the measurement a constant current is sent for several seconds to heat the superconductive wire outside liwuid helium above the superconductive transition. After stabilization the resistance of the wire outside the helium bath is measured with the same current used to warm up and the helium level deduced:

Pressure: the Sample Space pressure is measured by two manometers,

- a *Thermovac* for the low vacuum range;
- a *Ceravac* for the medium vacuum range;

2. Flow Box

Flow Regulation:

- a high capacity flowmeter is controlled to set the flow pumped from the Sample Space;
- a low capacity flowmeter is controlled to set the flow pumped from the Separator;

Pumping Path:

- an electro-mechanic valve sitting close to the Sample Space outlet is operated to isolate the cryostat from the flowbox during the polarization procedure;
- a three way valve is operated to switch the Sample Space line connection to the pumping line or to the pressurization/recovery path;
- a three way valve is operated to switch the Separator line connection to the pumping line or to the pressurization/recovery path;
- a three way valve is operated to switch the recovery path to be pressurize or connected to the helium recovery line;

Rotary/Root Pumps: can be switched on and off by a dedicated electronics, if the pumping system supports this feature;

3. Dissolution Management

Dissolution insert:

- a *Pt100* resistor is used to monitor the boiler temperature;
- a manometer is used to monitor the pressure in the boiler;
- a resistive heating wire is powered to heat up the water in the boiler;

- a push button is monitored to allow the user to trigger the dissolution procedure;

Pneumatic valves: are operated by an electro-mechanic hub with 4 compressed air lines;

Syringe pump: is interfaced to send the start/stop triggers and reading the pump status;

Bubble detector: is monitored to stop the infusion pump in case a bubble is formed in the infusion line;

Console trigger: can be sent both through a BNC and/or an optical fiber connectors;

A.2 Software

A custom made software standalone Graphical User Interface (GUI) was developed, in the Labview™ programming environment, to manage all the cryogenic and dissolution operations on the cryostat.

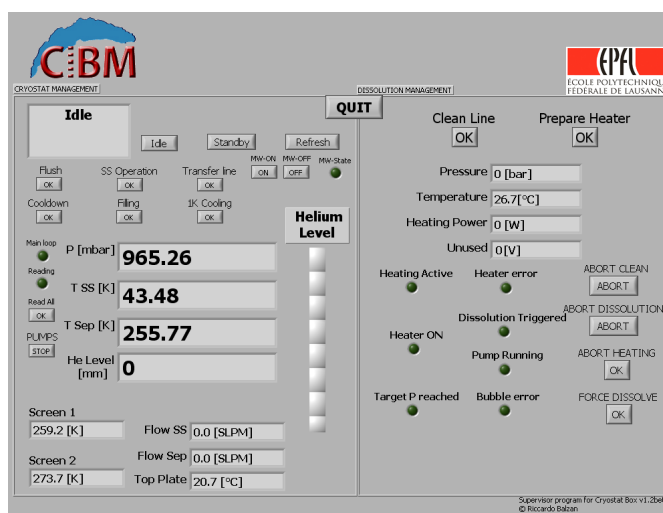


Figure A.2: Front panel of the Cryostat Management Software.

In Fig. A.2 the front panel of the software is presented.

The software is designed to be a "one click - one operation" interface. It is highly customizable through a configuration file that can be changed during runtime. The system parameters and the operations executed are logged in a text file.

It is arranged in two separate parts following the logical scheme of the setup.

Cryogenic Management

The left part is used to monitor the cryostat and control the cryogenic operations. The controls are located in the top part and follow the main operations and states in which the

Appendix A. Polarizer development

cryostat can be operated; every button changes the state automatically, with a reminder of the few manual operation needed to be done before the status changes. The monitoring part shows at a glance all the relevant parameters measured on the cryostat allowing the operator to easily notice eventual problems of the system.

Idle : the Sample Space as well as the Separator are connected to the recovery line. This is the state the system should be in when the cryostat is not used or for room temperature operations:

Standby : the Sample Space is connected to the recovery line and the Separator is pumped by the membrane pump. This is the state the system should be in when no operations are in progress and the cryostat should be kept at low temperature (around 40 ~ 60 K).

Flush : this procedure pumps out the air from the system and re-pressurizes the cryostat with helium gas. It must be run after each operation that involved opening the system to air.

- Slow Flushing: is the slowest protocol but it does not need the presence of an operator;
- Fast Flushing: is the fastest protocol. It requires less pump-pressurize cycles, but the user has to perform more manual operations;

SS Operations: this procedure always has to be run before the Sample Space is opened to air while it is cold, *e.g.* when the operator wants to insert a sample in the Sample Space, or during the dissolution procedure. The Sample Space is pressurized, preventing air to enter it while open;

Transfer line: this procedure is used when the transfer line needs to be connected to or disconnected from the cryostat. The Separator is pressurized, preventing air to enter it while open;

Cooldown: this procedure is used to cool the system from room temperature to a given low target temperature defined in the configuration file. Once the target temperature is reached the system automatically goes in the Mantain Cold state, in which the software monitors the temperature and cool down the system again if the temperature rises above a threshold.

Filling: this procedure, which should only be started when the cryostat is close to liquid helium temperatures, fills the cryostat with liquid helium up to a level preset in the configuration file. Once the liquid helium level is above the preset level, the system automatically goes in the Mantain full state, in which the software monitors the level and restart the filling procedure if the level decreases below a threshold;

1K cooling: this procedure allows to reach the lowest Sample Space temperature below the lambda point allowed by the system (the exact temperature depends on the vacuum pumps used to pump on the superfluid helium in the Sample Space).

The operator has to open the direct connection between the Sample Space and the big pumping line (Figure 2.2-1) allowing the main pumping system to work at full pumping efficiency on the liquid helium bath. Then the system will reach its base temperature and is ready to start the polarization. The software continuously monitor the helium level and displays it on the Helium Level bar.

MW-ON / MW-OFF: if the microwave source is supported, it can be controlled directly from the software front panel.

Automatic pressure and temperature monitoring: the software automatically and continuously monitors cryostat parameters to make sure the system is running in a safe mode. If undesired behaviors are detected the program automatically performs emergency procedures to prevent system failures. The emergency conditions can be controlled via the configuration file.

Dissolution Management

The right part of the software interface, is used to control the dissolution process. In the top part the two buttons allow to perform the two basic operations linked to the dissolution management, while the state of the dissolution insert, syringe pump and bubble detector are continuously monitored. To increase the flexibility of the system during this delicate procedure, other special operations were added in the lower right part.

Clean line: this procedure is used to clean the transfer line with water to remove leftovers of previously dissolved samples, and then to dry it with the pressurized helium gas. After the software button is pressed, the flushing procedure takes place only after the operator pushes the dissolution button (Fig. 2.4-E). The procedure can be aborted via the *ABORT CLEAN* button. This procedure can be used either when the dissolution insert heater is full of water (rinsing procedure) or when the heater is empty (flushing procedure).

Prepare heater: this procedure activates the heating process of the solvent used for the dissolution step. It pressurize the boiler with the compressed helium line and then it starts the heating to reach and keep the pressure stable within a range defined in the configuration file. When ready the software informs the user and waits for the dissolution button to be pressed to start the sequence.

The heating and dissolution sequence can be aborted via the *ABORT HEATING* and *ABORT DISSOLUTION* buttons respectively.

The dissolution can be started from the software interface via the *FORCE DISSOLVE* button.

Since this is one of the most delicate operations, a number of safety checks were implemented to prevent the operator to run the sequence in case an abnormal behavior is detected.

Dissolution sequence: in the configuration file a basic operational language was implemented to define the number of stages of the dissolution sequence, as well as the timing and the operations the software has to perform during the dissolution. With this solution it is possible to independently control the pneumatic valves on the dissolution insert, the syringe pump and the console triggering.

A.3 Details on cryogenic operations

All the following operations directly correspond to buttons on the Software front panel. Where not explicitly stated, we assume the membrane pump pumping on the Separator, the main pumping system off and the needle valves closed before and during each procedure or state.

Idle

When the system is not used for a long time and the liquid helium dewar is not connected, the cryostat is kept on Idle state: both the Sample Space and the Separator are directly connected to the recovery line and slightly pressurized 30 – 100 *mbar* above ambient pressure. In this state the software can be stopped and the box, as well as all the pumping system can be turned off safely.

This is the state which the Software sets after initialization. Depending on the initial temperature it can be necessary to wait even up to 4 ~ 5 days before all the cryostat parts reaches close to room temperature. This is mandatory in case the main insert has to be removed for maintenance.

Standby

Between experimental sessions or overnight, it is practical to leave the cryostat cold enough to be able to rapidly restart the filling and polarization procedures. The cryostat is kept in a "standby" state by continuously pumping a small helium flow through the Separator. Standby is the state in which the system should be set between experiments or when not used for short periods of time (*e.g.* overnight). The storage dewar must be connected and the Separator is pumped with a low flow to keep low temperature in the top cryostat part thus decreasing the amount of time necessary for the following cooldown. The Sample Space remains connected to the recovery line to evacuate the boiloff of eventual liquid helium present.

Flushing

During cryogenic operations no other gas than helium can be present in the cryostat. This because every other gas freezes at liquid helium temperature and can possibly clamp mobile parts or clog the tiny capillary tubes used for operations.

Flushing procedure is used to remove the air from the cryostat and pumping lines, and replace it with pure helium gas coming from the recovery line or an helium bottle. The rotary pump must be turned on and both needle valves must be opened before the sequence starts

Once the button is pressed the operator can choose between the slow procedure (automatic, time and helium consuming) or the fast procedure (requires operator interaction but is faster and requires less cycles thus decreasing the helium consumption).

The procedure can be aborted with the dedicated button appearing in the front panel during the sequence. At the end the system goes back to Idle state.

Sample Space Operations

This procedure is mandatory when the cryostat has to be opened even for short amount of time for sample placement or dissolution procedure. The software arranges the connections to pressurize the cryostat avoiding air contamination. At the end the system goes back to Standby state.

Transfer Line

Similar to the Sample Space Operation, in this state the Separator is connected to the overpressure line and it can be opened to place or remove the Transfer Line. It can be started from every state and goes back to Standby state except if the 1K Cooling (see below) procedure is running.

Cooldown

Before condensing helium, the cryostat has to be cooled down to close to liquid helium temperature. To do so the cold helium gas coming from the storage dewar is pumped through the Separator and then, through capillaries wrapped around and thermally anchored to the main metallic parts of the cryostat to enhance the heat transfer, into the Sample Space. The rotary pump must be turned on before the sequence starts. Both needle valves need to be opened.

During this procedure the Separator is connected to the Sample Space and both are pumped at a calibrated flow to obtain a good compromise between time spent for the cooldown and helium used.

The cooldown is performed through two pumping lines:

- the first from the Separator to the membrane pump, produces a flow of cold helium through the capillary wrapped around the top part of the cryostat. This flow cools down the top baffles and the radiation screens in the OVC;
- the second from the Sample space to the main pumping system to lower the pressure in the Sample Space and force the helium gas from the Separator into the Sample Space.

Appendix A. Polarizer development

The cooldown is efficient in both the top part and the tail of the cryostat thanks to the long capillaries wrapped around and thermally anchored to the central tube; their functions is to increase the contact surface between gas and metallic cryostat parts allowing an efficient heat exchange in both ways: when the cold gas or liquid flows from the Separator to the Sample Space and when the gas is pumped out of the cryostat directly from the Separator. Once the cryostat temperature reaches the target value set in the configuration file, the software goes to Maintain Cold state. This is the same as Standby with the difference that both needle valves are still open and the software continuously monitor the temperature. If it increases above a certain threshold the Cooldown procedure is restarted.

From Cooldown or Maintain Cold states, the operator can go back to Standby after closing the needle valves or proceed with the Filling procedure.

Filling

Before starting the hyperpolarization we need to fill the Sample Space with liquid helium. As soon as liquid helium is condensed in the Separator it can be transferred to the Sample Space by strongly pumping on it.

This state is similar to Cooldown, with the difference that it monitors the helium level and goes in Mantain Full state once the level is above the desired value set in the configuration file. As well as the Mantain Cold, the Mantain Full state is basically a Standby with the needle valves open. It turns back to Filling state if the liquid helium level drops below a certain threshold defined in the configuration file.

The Mantain Full is very helium consuming; since the Separator is still pumped and connected to the Sample Space, the liquid helium is slowly sucked back and wasted. To avoid that situation it is advised to stop the Mantain Full procedure as soon as possible by going to Standby state and to close the needle valves.

1 K cooling and solid-state DNP

After the filling procedure, and with the sample and polarization hardware placed in the cryostat, the procedure to reach the lowest allowed temperature in the helium bath can be started with the 1K Cooling button.

On the first stage the rotary pump have to be turned on. After the sequence starts the operator has to open the KF-50 VAT manual valve on the top cross of the cryostat. Notice that this valve should be opened only while the software is in the 1 K Cooling state to prevent helium gas being pumped from the recovery line.

After the pressure is low enough the software isolates the Sample Space from the flow box closing the electro-mechanic valve sitting at the exit of the Sample Space pumping line. Furthermore, the software asks the user to turn on the root pumps to reach the lower allowed pressure, dependent on the maximum pumping flow.

It takes several minutes to lower the pressure from 1 *bar* to 1 *mbar*. Once the helium bath becomes superfluid, after the temperature has decreased below 2.17 K the microwaves can

be irradiated on the sample to start the DNP process. At the end, before exiting this state to perform every other operation, the KF-50 VAT manual valve on the top cross must be closed and the root pumps turned off.

Dissolution

The dissolution procedure needs to be as fast as possible to limit the polarization losses due to T_1 relaxation. The dissolution consists in blowing D_2O steam at about $160 - 190^\circ C$ on the frozen sample while still in the cryostat at high field, to convert it into a liquid solution that can be quickly pushed out of the cryostat to the MRI/MRS scanner for the experiment. The dissolution insert boiler is filled with D_2O and heated to reach the target temperature. Then the cryostat is pressurized to be opened for the dissolution insert to be inserted and immediately the automated dissolution procedure is started. After the dissolution was performed the cryostat can be refilled and the procedures repeated.

A.4 Outlook on automation improvements

Although the high degree of optimization obtained on the cryogenic management side, the operator is still required to perform some actions on the cryostat. In the following we propose some improvements that could be added to the system to let it become a completely automated system without any need of operator interaction in normal conditions.

The interactions still required by the operator are linked to the following component:

Needle valves: these are the most common operated components of the cryostat. They have to be opened and closed when the cryostat goes from Standby to Cooldown and back, preventing the cryostat to be cooled remotely. The micro-metric screws driving the needle valves could be replaced by automated servo-motors and the electronic box modified to handle them according to the software requirements. This would give the operator the possibility to start remotely or schedule the beginning of the different operations, to obtain the cryostat ready for polarization at a certain time. This could routinely save about one hour for the initial system cooldown and filling.

Manual Valve on the top cross: although this valve is opened or closed only during at the beginning and at the end of the 1 K procedure, it requires user interaction. Furthermore if the operator misses to close it before the software exits the 1 K procedure, the main pumping system starts to pump straight from the recovery line, with the possible risk of contaminating the cryostat with impurities from the recovery line and of damaging the pumping system. An electro-mechanic valve could replace the manual one, allowing for full software control of the system and preventing mistakes and mishandling.

Appendix A. Polarizer development

Despite these two proposed improvements, the degree of automation already obtained is very high. It was shown during the various installations mentioned in section 2.3 that, despite the system complexity, the required installation time can be as short as a couple of days. Furthermore only a training period of several days is enough for new operators to fully understand the system and to be able to autonomously manage the cryostat and perform dissolutions.

B Steady State for evenly spaced pulses

We want to exactly determine the evolution of magnetization intensity on the z axis for a sequence composed of a train of constant RF pulses of θ flip angle (considered instantaneous) evenly spaced with a repetition time of δ . The goal of this section is to obtain without approximations the system magnetization in function of time for every choice of θ and δ .

Evolution

In the j^{th} experiment we measure a signal proportional to the magnetization M_j of the system before the pulse is applied, multiplied by a $\sin\theta$ term that accounts for the projection on the xy plane of the magnetization flipped by an angle θ from the z axis. Since this is a constant factor it will be omitted where not necessary, and only the behavior of M_j studied.

After applying a θ flip angle pulse, the magnetization on the z axis is multiplied by a factor $\cos\theta$. Between two pulses the magnetization on the z axis $M'_{j+1}(\tau)$ where $0 < \tau < \delta$ relaxes according to Bloch equations.

We can summarize the discrete evolution of the magnetization caused by the pulse and the free evolution:

$$\begin{aligned} M'_{j+1}(0) &= M'_j(\delta) \cos\theta \\ M'_{j+1}(t) &= M_{th} - \left(M_{th} - M'_{j+1}(0) \right) e^{-\frac{t}{T_1}} \quad t \in [0, \delta] \end{aligned} \tag{B.1}$$

where T_1 is the nuclear longitudinal relaxation time, M_{th} is the thermal equilibrium magnetization and $M'_j(t)$ describes the evolution of the magnetization between the j^{th} and the $(j+1)^{th}$ pulses.

Appendix B. Steady State for evenly spaced pulses

In the following we define:

$$\begin{aligned}
 M'_j &= M'_j(t=0) \\
 M_j &= M'_j(t=\delta) \\
 \alpha &= \cos\theta \\
 \beta &= e^{-\frac{\delta}{T_1}}
 \end{aligned} \tag{B.2}$$

With these definitions we obtain, for the first pulse:

$$\begin{aligned}
 M_0 &= M(t=0) \\
 M'_1 &= M_0\alpha \\
 M_1 &= M_{th}(1-\beta) + M_0\alpha\beta
 \end{aligned} \tag{B.3}$$

Then for the second pulse:

$$\begin{aligned}
 M'_2 &= M_{th}(1-\beta)\alpha + M_0\alpha^2\beta \\
 M_2 &= M_{th}(1-\beta) + M_{th}(1-\beta)\alpha\beta + M_0\alpha^2\beta^2
 \end{aligned} \tag{B.4}$$

Finally we can give a general explicit expression for the magnetization evolution:

$$\begin{aligned}
 M_j &= M_{th}(1-\beta) \sum_{k=0}^{j-1} (\alpha\beta)^k + M_0(\alpha\beta)^j \\
 &= M_{th} \frac{1-\beta}{1-\alpha\beta} (1-(\alpha\beta)^j) + M_0(\alpha\beta)^j
 \end{aligned} \tag{B.5}$$

Then, defining:

$$\begin{aligned}
 M_{\infty}^{\delta,\theta} &= M_{th} \frac{1-\beta}{1-\alpha\beta} \\
 T'_{\delta,\theta} &= \frac{1}{\frac{1}{T_1} - \frac{\ln\alpha}{\delta}}
 \end{aligned} \tag{B.6}$$

we obtain exactly:

$$M_j = M_\infty^{\delta,\theta} - \left(M_\infty^{\delta,\theta} - M_0\right) e^{-\frac{j\delta}{T'_{\delta,\theta}}} \quad (\text{B.7})$$

that is the same as equation 3.5 if we extend the discrete $j\delta$ to continuous time t .

Now, in a typical experiment $T'_{\delta,\theta}$ can be easily extracted by fitting the hyperpolarized magnetization decays and then values of T_1 and θ determined from equation B.6.

Achieving the steady state

To achieve the steady state polarization we can use two strategies:

- start the pulsing sequence from an arbitrary magnetization; in this case we have to wait about $5 T'$ until M_j reaches close enough to $M_\infty^{\delta,\theta}$. The measurement performed during the initial $5 T'$ should be discarded;
- saturate the nuclei to achieve a known initial state with magnetization $M_0 = 0$. Then wait a time T^* without pulsing, for the magnetization to freely relax to $M_\infty^{\delta,\theta}$. Once the magnetization reaches this value the acquisition sequence can be started.

From equation B.7 we can calculate T^* imposing the condition:

$$\left(1 - e^{-\frac{T^*}{T_1}}\right) M_{th} = M_\infty^{\delta,\theta} \quad (\text{B.8})$$

we obtain:

$$T^* = -\ln\left(\beta \frac{1-\alpha}{1-\alpha\beta}\right) T_1 \quad (\text{B.9})$$

for low enough δ , T^* is much shorter than $5 T'$. T^* reaches a minimum for $\delta \ll \theta \ll 1$ of $T^* \sim T'$.

Measurement optimization

To determine the thermal signal, already knowing the values of T_1 and θ , a single measurement of a steady state signal is enough. Thus we can choose the value of δ to minimize the overall time spent for the measurement.

To choose δ we only have to decide which measurement precision we want to achieve with

Appendix B. Steady State for evenly spaced pulses

respect to a relative scale. We can assume the unity of this scale the Signal to Noise Ratio (SNR) achievable with a single $\pi/2$ pulse measurement on the thermally relaxed sample.

To calculate the number of averages needed to obtain a defined Relative SNR ($RSNR$) we assume a constant noise level along all the measurements and a gaussian error propagation; we have to consider:

- the signal measured using a θ flip angle pulse has an intensity $\sin \theta$ times the $\pi/2$ pulse measurement;
- the signal measured while the system is in the steady state originates from a magnetization $M_{\infty}^{\delta, \theta}$, lower than M_{th} .

So, the $RSNR$ obtained from n measurements is given by:

$$RSNR_{\delta, \theta}(n) = \sin \theta \frac{1 - \beta}{1 - \alpha \beta} \sqrt{n} \quad (B.10)$$

In Section 3.2, we showed how to determine the $RSNR$ achievable in a fixed amount of time. Here we invert equation B.10 and solve it for a given $RSNR$ and flip angle θ , for the optimal δ and n to achieve the minimum overall measurement time t_{tot} . In t_{tot} we have to considering both the T^* and the effective measurement time δn . For ease the explanation we consider a target $RSNR = 1$; in Table 3.1 we give the values of all the relevant optimized parameters for different choices of $RSNR$.

The effective time spent during the measurement period is:

$$T_{Meas} = \left[\frac{RSNR_{\delta, \theta}}{\sin \theta} \cdot \frac{1 - \alpha \beta}{1 - \beta} \right]^2 \cdot \delta = n \delta \quad (B.11)$$

Nevertheless what we have to minimize, in function of δ , is the total time of the experiment, meaning the sum of the initial waiting time T^* and the time effectively spent for the measurement T_{Meas} :

$$t_{tot} = T^* + T_{Meas} \quad (B.12)$$

No explicit form of $\delta_{\theta}(RSNR)$, in function of θ and $RSNR$, to minimize equation B.12 was found so the minimization was performed numerically.

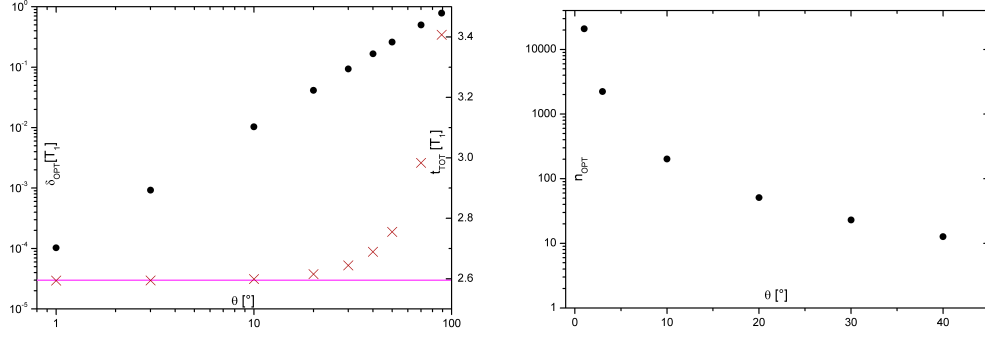


Figure B.1: Left: behavior of the optimal δ_{OPT} (black circles) that minimizes the total measurement time t_{TOT} (red crosses) in function of θ choosing $RSNR = 1$. The magenta horizontal line is the limit value of the minimal t_{TOT} for low θ . Right: number of averages needed in the minimum measurement time conditions.

In Figure B.1-left we can see that δ_{OPT} is roughly proportional to θ^2 in all the considered range, while the total measurement time t_{TOT} reaches a minimum of about $2.6 T_1$, for a $RSNR = 1$, that is about half the $5 T_1$ needed in the classical scheme.

From Figures B.1 we can make some observations:

- if the flip angle is $\theta \gtrsim 30^\circ$ the measurement time increases;
- if the flip angle is too small there is no gain in measurement time but the requested number of averages increases very fast (for $\theta = 1^\circ$ $n > 20000$) possibly creating problems arising from averaging spectra.

Although the model is valid for every θ and δ , we can establish an additional constraint to ease the measurements. In this example with a given $RSNR = 1$, in order to keep the measurement time close to the minimum, and the number of acquired spectra as small as possible, the flip angle should be roughly chosen in the range $10^\circ < \theta < 20^\circ$. If the required SNR is lower, the number of averages rapidly decreases and the lower constraint on θ can be relaxed.

C Optimized Hartmann-Hahn polarization transfer for choline

In this appendix we will show a strategy to optimize the polarization transfer of ^{15}N to ^1H in order to obtain, for example, a constant signal originated from the choline substrate.

C.1 Optimized polarization transfer

A constant low flip angle is normally used for all the sequential excitations and detections in hyperpolarized MR experiments aimed at determining the time evolution of the substrate and metabolites MR signals. This scheme is very simple but has the disadvantage that the SNR varies dramatically between the first and the last experiments since the signal decays with time.

If all the relevant parameters of the experiment are known (*e.g.* T_1 of the hyperpolarized nucleus in the substrate and metabolites, polarization transfer efficiency, etc.), the Hartmann-Hahn scheme presented can be optimized in function of the desired conditions. As an example, we can determine the set of contact times to be used in the sequence of figure C.1 to obtain a constant substrate signal intensity for all sequential measurement.

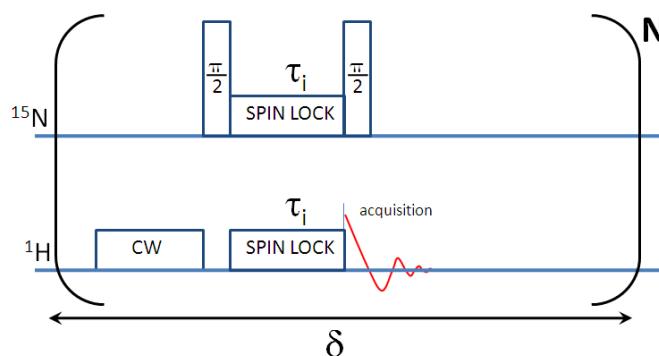


Figure C.1: Pulse sequence used for the optimized partial Hartmann-Hahn polarization transfer. δ is the repetition time, N is the total number of acquisitions and τ_i is the optimized contact time used in the i^{th} acquisition.

Appendix C. Optimized Hartmann-Hahn polarization transfer for choline

To explain the method in the following we consider the ^1H to ^{15}N transfer (of which we know the characteristic curves in figure 5.3). The same reasoning can be straightforwardly applied to the ^{15}N to ^1H transfer shown in figure C.1 if the reverse transfer from ^{15}N to ^1H characteristic curves are known.

Interpolating data in figure 5.3, we can numerically define for $\tau < 1.5\text{ s}$ and $\epsilon_{15\text{N}} \leq \epsilon_{15\text{N}}^{HH}$ a function $\rho(\epsilon_{15\text{N}})$ that represents the residual ^1H polarization, from a unitary ^1H polarization, after we performed a partial Hartmann-Hahn transfer, to obtain a ^{15}N enhancement of $\epsilon_{15\text{N}}$ with a contact time of $\tau(\epsilon_{15\text{N}})$.

We want to obtain for each single step i a constant signal, and thus polarization, on ^{15}N of $\epsilon_{15\text{N}} \ll \epsilon_{15\text{N}}^{HH}$, starting from thermal ^1H polarization. We define $P_{i-}^{1\text{H}}$ the proton polarization before the i^{th} polarization transfer and $P_{i+}^{1\text{H}}$ the proton polarization after the i^{th} polarization transfer. $\delta > \tau(\epsilon_{15\text{N}}^{HH})$ is the constant repetition time.

We assume to have in our system, at time $t = 0$, a known proton polarization $P_{1-}^{1\text{H}} = P_0$. We can explicitly write expression for the evolution of proton polarization during the first acquisitions:

$$\begin{aligned} P_{1-}^{1\text{H}} &= P_0 \\ P_{1+}^{1\text{H}} &= P_{1-}^{1\text{H}} \rho(\epsilon_{15\text{N}}/P_{1-}^{1\text{H}}) \\ P_{2-}^{1\text{H}} &= P_{1+}^{1\text{H}} \cdot \left(1 - e^{-\frac{\delta - \tau(\epsilon_{15\text{N}}/P_{1+}^{1\text{H}})}{T_1}} \right) \end{aligned} \quad (\text{C.1})$$

where $P_{1-}^{1\text{H}}$ represents the proton polarization before the first Hartmann-Hahn polarization transfer, $P_{1+}^{1\text{H}}$ the residual proton polarization after the transfer and $P_{2-}^{1\text{H}}$ the proton polarization after the longitudinal relaxation during the period between the first and the second polarization transfer.

The proton polarization before the second transfer step is lower than before the first transfer step $P_{2-}^{1\text{H}} < P_{1-}^{1\text{H}}$. To obtain the same polarization on ^{15}N in the second transfer step we need to increase the contact time from $\tau(\epsilon_{15\text{N}}/P_{1-}^{1\text{H}})$ to $\tau(\epsilon_{15\text{N}}/P_{2-}^{1\text{H}})$. This way, in the second step the proton polarization is further decreased of a factor $\rho(\epsilon_{15\text{N}}/P_{2-}^{1\text{H}})$.

Summarizing these observations we can define the iterative rule for an arbitrary polarization transfer i :

$$\begin{aligned} P_{i+}^{1\text{H}} &= P_{i-}^{1\text{H}} \cdot \rho\left(\frac{\epsilon_{15\text{N}}}{P_{i-}^{1\text{H}}}\right) \\ P_{i+1-}^{1\text{H}} &= P_{i+}^{1\text{H}} \cdot \left(1 - e^{-\frac{\delta - \tau(\epsilon_{15\text{N}}/P_{i+}^{1\text{H}})}{T_1}} \right) \end{aligned} \quad (\text{C.2})$$

The equations C.2 can be numerically solved once δ and ϵ_{15N} are chosen, to obtain a set of $\tau_i(\epsilon_{15N}, \delta)$ that will be used as contact times for each of the measurements respectively. The maximum number of steps is limited by the domain of the ρ function. This because after a certain step i_{max} we have $\epsilon_{15N}/P_{i_{max}}^{1H} > \epsilon_{15N}^{HH}$. After this moment the residual 1H polarization is too low to obtain the desired polarization on ^{15}N .

The same reasoning can be applied on the other direction to transfer magnetization from ^{15}N to 1H after measuring the efficiency of the reverse transfer. It can be applied as well to any pair of nuclear spins for which the characteristic curves showed in figure 5.3 have been determined.

D Table of abbreviations

Abbreviation	Explanation
DNP	Dynamic Nuclear Polarization
NMR	Nuclear Magnetic Resonance
MRI	Magnetic Resonance Imaging
MRS	Magnetic Resonance Spectroscopy
ESR	Electron Spin Resonance
RF	Radio Frequency
FID	Free Induction Decay
GRE	Gradient Echo Imaging
TMS	Tetramethylsilane
BPP	Bloemberg-Purcell-Pound theory
EZR	Electronic Zeeman Reservoir
EDR	Electronic Dipolar Reservoir
NZR	Nuclear Zeeman Reservoir
MW	Microwaves
SEOP	Spin-Exchange Optical Pumping
PHIP	Para-Hydrogen Induced Polarization
PASADENA	Parahydrogen And Synthesis Allow Dramatically Enhanced Nuclear Alignment
OVC	Cryostat Outer Vacuum Chamber
SNR	Signal to Noise Ratio
RSNR	Relative Signal to Noise Ratio
NA	Natural Abundance
GM	Granular Materials
T_1	Longitudinal relaxation time
T_2	Transverse relaxation time
SLPM	Standard Liters Per Minute
UI	Heparine standard unit
GUI	Graphical user interface
PSI	Paul Scherrer Institute
SEPT	Sample Environment and Polarised Targets group

CURRICULUM VITAE

PERSONAL INFORMATION

Name	Riccardo
Surname	Balzan
Address	Via Roma n.30 – 37043 Castagnaro (VR)
Phone	+393391257863
Mail	riccardo.balzan@hotmail.it
Nationality	Italian
Place and date of birth	Legnago (VR) Italy – 10-12-1984

INSTRUCTION

- 2008 - Master degree in Physics with vote 110/110 cum laude
Thesis “Experimental study of granular media: brownian motor”
(Supervisor: Prof. V. Loreto)
“La Sapienza” Rome University – Rome (Italy)
- 2006 - Bachelor degree in Physics with vote 110/110 cum laude
Thesis “Study of a simplified model of granular gas”
(Supervisor: Prof. V. Loreto)
“La Sapienza” Rome University – Rome (Italy)
- 2003 - High School Diploma, Chemistry specialization with vote 100/100
I.T.I.S. G.Silva – Legnago (VR) (Italy)
- 2002 - Monthly Stage as chemical laboratory analyst
for C.A.S. – Castagnaro (VR) (Italy)

PRIZES

- 2004-2007 - Collaboration Grant - Physics Department Library -
"La Sapienza" Rome University (Italy)
- 2003 - Silver Medal - 35th International Chemistry Olimpiad
IChO - Athens (Greece)
- 2003 - 1st place - National Chemistry Games
Italian Chemical Society SCI - Rome (Italy)
- 2002 - 4th place - Certamen of Chemistry
AICA - Frosinone (Italy)

ACTUAL EMPLOYMENT

Since 2009 PhD student in Physics at EPFL – Lausanne (Switzerland) under the supervision of Prof. A. Comment and Prof. R. Gruetter.

Thesis project covers:

- hardware and software development of automated electromechanical control systems for cryogenics and NMR;
- use and optimization of cryogenic apparatus;
- use and development of NMR systems;
- dynamic nuclear polarization (DNP) techniques applied to magnetic resonance in solid state, in vitro and in vivo.

PROFESSIONAL EXPERIENCE

Among an university/company collaboration I gained experience on development and installation of cryogenic and NMR systems applied to solid state physics, hyperpolarization and dissolution DNP.

The project consists in the *ex novo* development of an automated dissolution DNP system. My work has been focused first on cryogenic, electronic, mechanical and software development to create a fully automated solid state NMR and dissolution DNP system. After the development, I optimized the performances and tested all the procedures from the basic cryogenics to the *in vivo* NMR/MRI experiment.

Afterwards, I took care of the installation of the system in various top universities in Europe and United States.

ABILITIES AND SKILLS

English Language	Fluent, professional proficiency
French Language	Good
Italian Language	Mother tongue
Software	MS Office Origin AutoCAD Labview C and C++ Programming languages
Skills and Attitudes	NMR system utilization and optimization Hardware/software system development. 3D Mechanical design. Cryogenic system management. Experience in installation of cryogenic/NMR systems in university environments in collaboration with Vanderklink Sàrl, Echichens, CH. Experience in hardware/software integration and automation of management and measurement systems.

SCIENTIFIC PUBLICATIONS

Journal Articles

2013

A link between short-range and long-range properties of random sphere packings

R. Balzan, A.L.Sellerio, D. Mari, A. Comment, G. Gremaud

Granular Matter - DOI:10.1007/s10035-013-0450-8

Over 35% liquid-state ^{13}C polarization via dissolution dynamic nuclear polarization at 7 T and 1 K with ubiquitous nitroxyl radicals

Cheng Tian, Capozzi Andrea, Yuhei Takado, Balzan Riccardo, Comment Arnaud

Physical Chemistry Chemical Physics - DOI:10.1039/C3CP53022A

Hyperpolarized ^6Li as probe for hemoglobin oxygenation level

R. Balzan, M. Mishkovsky, Y. Solomon, R. B. van Heeswijk, R. Gruetter, U. Eliav, G. Navon, A. Comment

In preparation

Accurate fast low-angle solid-state nuclear polarization measurement

R. Balzan, A. Capozzi, T. Cheng, A. Comment

In preparation

A new MRI reconstruction technique based on real space Hough transform for granular samples

R. Balzan, A.L.Sellerio, D. Mari, A. Comment, G. Gremaud

In preparation

Dissolution-DNP setup for in vivo hyperpolarized MRS and MRI in rat muscle at 14.1T

R. Balzan, J. Bastiaansen, T. Cheng, A. Capozzi, J. Van Der Klink and A. Comment

In preparation

2011

Brownian Motor in a Granular Medium

R. Balzan, F. Dalton, V. Loreto, A. Petri and G. Pontuale

Physical Review E 83, 031310 (2011)

Conference Proceedings

2013

- Accurate fast low-angle solid-state nuclear polarization measurement
R. Balzan, A. Capozzi, T. Cheng, A. Comment
- ^{13}C DNP efficiency in function of the glassing matrix content at different magnetic fields
A. Capozzi, T. Cheng, R. Balzan, V. Breukels, J. van Bentum, T. Scheenen, A. Comment
- Bioreactor to simultaneously measure three parallel in vitro preparations
E. Can, L. D. Daoudi, Y. Pilloud, R. Balzan, R. Gruetter, A. Comment
- Over 35% of liquid-state ^{13}C polarization enhanced by TEMPOL via high field dissolution DNP
T. Cheng, A. Capozzi, Y. Takado, R. Balzan, A. Comment
- Development of a user facility for dissolution DNP development and applications
A.N. Smith, D.P. Downes, R. Balzan, A. Capozzi, A. Comment, J.R. Long

4th International DNP Symposium - 28-31/08/2013 Copenhagen DK

2012

A new MRI reconstruction technique based on real space Hough transform for granular samples
R. Balzan, A.L. Sellerio, D. Mari, A. Comment, G. Gremaud

EUROMAR - 1-5/7/2012 - Dublin IRL

T_1 Relaxation of Hyperpolarized ^6Li in Oxygenated and Deoxygenated Blood

R. Balzan, M. Mishkovsky, Yana Simonenko, Ruud Van-Heeswijk, Rolf Gruetter, Gil Navon and A. Comment

ESMRMB - 4-6/10/2012 - Lisbon P

2011

Effects of Blood and Plasma Oxygenation on the Spin Relaxation Times of Hyperpolarized ^6Li
R. Balzan, Y. Solo, M. Mishkovsky, R. Gruetter, G. Navon and A. Comment

Joint Annual Meeting - Swiss Physical Society - 15-17/06/2011 - Lausanne CH

Development and characterization of an automated dissolution-DNP setup for in vivo hyperpolarized MRS and MRI in rodent at 14.1T

R. Balzan, T. Cheng, J. Van Der Klink and A. Comment

3rd International DNP Symposium - 7-10/09/2011 - Lausanne CH